12-2013

An Implantable Low Pressure Biosensor Transponder

Chad Eric Seaver
University of Tennessee - Knoxville, cseaver1@utk.edu

To the Graduate Council:

I am submitting herewith a thesis written by Chad Eric Seaver entitled "An Implantable Low Pressure Biosensor Transponder." I have examined the final electronic copy of this thesis for form and content and recommend that it be accepted in partial fulfillment of the requirements for the degree of Master of Science, with a major in Electrical Engineering.

Jeremy Holleman, Major Professor

We have read this thesis and recommend its acceptance:

Syed Islam, Mohamed Mahfouz

Accepted for the Council:
Carolyn R. Hodges

Vice Provost and Dean of the Graduate School

(Original signatures are on file with official student records.)

An Implantable Low Pressure Biosensor Transponder

A Thesis Presented for the

Master of Science

Degree

The University of Tennessee, Knoxville

Chad Eric Seaver

December 2013

This thesis is dedicated to my sons,

Alex and Evan,

for encouraging me through their inquisitive nature and love

for science as well as to inspire them in their future studies,

and also to

those that suffer from intracranial hypertension, such as

hydrocephalus, and other related diseases.

Acknowledgements

Throughout my life's experiences and studies the hand of a creator and designer has been evident to me. Many times I've felt the Spirit of the Lord, known as "I AM", with me. I wish to first thank God and my Lord and Savior Jesus Christ, for allowing me the opportunity and ability to advance the study of electronics in medicine.

I also wish to thank the partners and investors of Arkis BioSciences for their support of this work. It is a privilege to have the opportunity to advance the study of diagnostics and treatments for those affected by diseases such as hydrocephalus. I'm especially thankful to Dr. James Killeffer for his neurosurgical mentorship and encouragement of this research. I'm also very grateful for the support of the Electrical Engineering department of the University of Tennessee. I'd like to thank my thesis committee, Dr. Jeremy Holleman, Dr. Syed Islam, and Dr. Mohamed Mahfouz, for their advisement, patience, and flexibility in supporting this work.

Finally, this opportunity stems from the encouragement, mentoring, investment, and love of many friends and family throughout my life. My mother and father have always encouraged and supported me in furthering my education. I appreciate their love and support of my studies and life overall. I also wish to acknowledge my brother, Brian, in motivating me for the study of engineering, who set an assertive example of dedication and hard work in his education. I also wish to recognize and thank the late Dale Christian, my lifelong dear friend, who not only encouraged me during my college education, but mentored and shared so many of life's wonderful qualities during my

childhood. Further, I very much wish to thank my lovely wife, Patricia, who has been supportive of me in every step of my college education. My studies have often come with a sacrifice of time to my family and without her support, this work wouldn't have been possible. I also appreciate my wonderful sons, Alex and Evan, for their interest and respect of my studies, in which I truly hope to inspire a love for learning in their lives as well.

Abstract

The human body's intracranial pressure (ICP) is a critical element in sustaining healthy blood flow to the brain while allowing adequate volume for brain tissue within the relatively rigid structure of the cranium. Disruptions in the body's maintenance of intracranial pressure are often caused by hemorrhage, tumors, edema, or excess cerebral spinal fluid resulting in treatments that are estimated to globally cost up to approximately five billion dollars annually. A critical element in the contemporary management of acute head injury, intracranial hemorrhage, stroke, or other conditions resulting in intracranial hypertension, is the real-time monitoring of ICP. Currently such monitoring can only take place short-term within an acute care hospital, is prone to measurement drift, and is comprised of externally tethered pressure sensors that are temporarily implanted into the brain, thus carrying a significant risk of infection. To date, reliable, low drift, completely internalized, long-term ICP monitoring devices remain elusive. In addition to being safer and more reliable in the short-term, such a device would expand the use of ICP monitoring for the management of chronic diseases involving ICP hypertension and further expand research into these disorders. This research studies the current challenges of existing ICP monitoring systems and investigates opportunities for potentially allowing long-term implantable bio-pressure sensing, facilitating possible improvements in treatment strategies. Based upon the research, this thesis evaluates piezo-resistive strain sensing for low power, sub-millimeter of mercury resolution, in application to implantable intracranial pressure sensing.

Table of Contents

List of Tables

List of Figures

Chapter 1 - Introduction

The human body is comprised of various organs that generate or are subject to a variety of pressures. These pressures are primarily induced externally due to gravity and include atmospheric compression and body weight opposition. However, there are also a wide range of pressures induced within the body itself. These pressures include those generated by the cardiovascular system, urinary system, digestive tract, musculoskeletal system, central nervous system, among others. Most of these pressures are critical for good health and must be precisely regulated. Blood pressure of the cardiovascular system and cerebral spinal fluid of the central nervous system are two such components that must be precisely maintained. The ability to continuously monitor these pressures would allow for early detection and intervention in the event regulation becomes impaired.

The goal of this work is for the feasibility of a long term implantable in-vivo pressure measurement transponder to facilitate frequent non-invasive monitoring. With the advancement of micro-electromechanical system (MEMS) sensor elements, low power inductively charged electronics, standardized wireless methods, as well as wireless hand held computing devices, it has recently become more feasible to approach the concept of long term implantables for such monitoring. In specific, this work will approach the challenge of long term monitoring of intracranial pressures induced by cerebral spinal fluid where high resolution pressures, on the order of a millimeter of mercury, must be measured in-vivo with low drift. Such pressure is among the most critical found within the body whereby intracranial hypotension can lead to ruptured

blood vessels and hematomas while hypertension can lead to decreased blood perfusion within the brain. Either case can quickly become life threatening and affects one to two percent of the population congenitally by hydrocephalus, or acquired due to brain tumor, traumatic obstruction, or damage to the arachnoid villi from meningitis, for example.

Chapter 2 - Background

Intracranial Pressure and Disease Monitoring

Pressure within the cranium is due to the arterial and venous pressure acting against the pressure head of the intracranial contents. Blood flow to the brain, characterized by cerebral perfusion pressure (CPP), is commonly calculated using ICP and mean arterial pressure (MAP) using the relationship CPP = MAP – ICP. Intracranial pressure is normally generated primarily from the formation of cerebral spinal fluid (CSF) and is a result of the pressure volume relationship of incompressible fluids within the semi-rigid intracranial compartment. Therefore, any changes in the volume of the intracranial contents alters ICP. CSF is formed by the choroid plexus within the first and second lateral ventricles of the brain, illustrated in Figure 1, where it thereafter flows into the third and fourth ventricles. Flowing from the ventricles, CSF then surrounds the spinal cord and subarachnoid space, where it is reabsorbed by the arachnoid villi. Pressures vary in human beings, but generally fall within the range of 68 to 136 mm H_2O in normal adults [1, 2].

Abnormalities occur when there is an over generation of CSF by the choroid plexus or a malabsorption of the fluid by the arachnoid villi, such as that of hydrocephalus. Abnormal pressures can also result when restrictions or obstructions in the fluid pathway retard or prevent CSF reabsorption. These obstructions can often be congenital, but also can result from brain tumors or head trauma. Figure 2 shows an MR axial brain scan where enlargement of the lateral ventricles has occurred as a result

of abnormally high ICP. Severe intracranial pressures can extend beyond 500 mm H_2O [3].

Typical methods for assessing intracranial pressures require a surgical procedure to install a ventricular catheter through the skull and thereafter measuring CSF pressure with an external manometer. Another method involves the use of a tethered electrical or optical pressure sensor that can be inserted into the brain for local in-vivo readings. For example, optical pressure sensors are commercially available with a pressure transducer located at the tip of a fiber optic strand. Fiber optic instrumentation is used to provide pressure read outs based upon interferometer techniques to detect translation of the of the pressure transducer diaphragm.

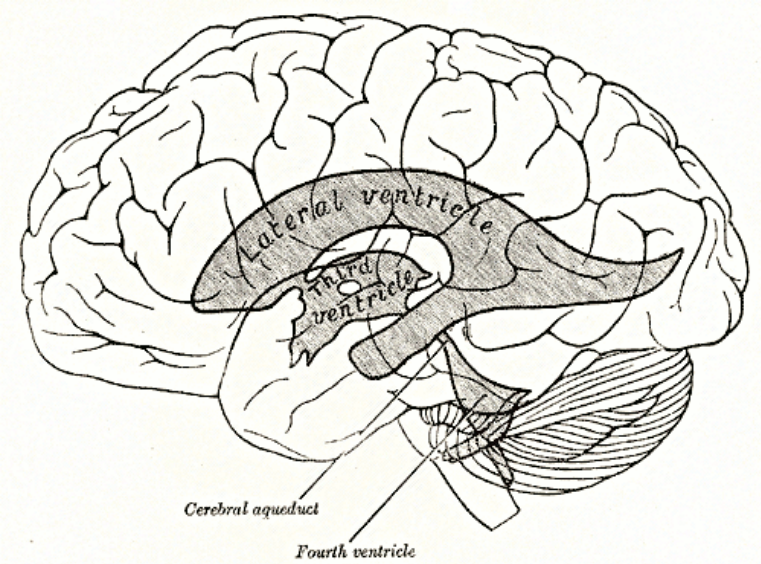

Figure 1 – CSF generation within the brain.
(Source: Gray's Anatomy of the Human Body, 20th edition)

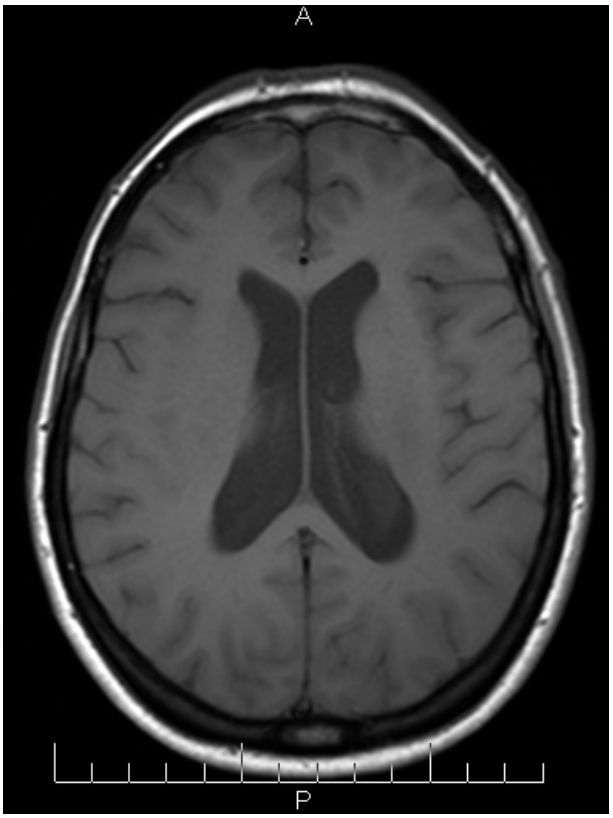

Figure 2 – Axial MRI showing enlargement of the lateral ventricles due to elevated ICP.
(Source: Neurosurgery Center of Colorado)

While these methods provide in-situ assessment of intracranial pressure, they do so most invasively and only upon a temporary basis within a surgical or intensive care setting. Typically, these types of pressure measurements are only carried out after a variety of other expensive diagnostics, such as medical imaging, have been exhausted in an attempt to explain the root cause of a patient's illness. Once it's determined to proceed with invasive pressure measurements, the patient must be sedated while the sensing element is surgically installed. Thereafter, the pressure element remains

temporarily tethered to the patient through a bore hole in the skull. It's then necessary to place the patient under continuing hospital care in order to monitor the pressures over time. Therefore, these assessment techniques are unfortunately the most invasive and expensive approach possible. They furthermore increase patient risk with the potential of surgical complications, such as infection, especially for prolonged periods [4]. Since intracranial pressure can rapidly rise due to an adult's fixed intracranial volume, patients can quickly reach a critical state by the time all preliminary diagnostics have proven negative. Therefore, there exists a need for high risk patients to be able to routinely and non-invasively monitor ICP to prevent life threatening emergencies and also to allow further research into ICP under various activities. The work of this thesis addresses this problem by investigating the sensing and electronic circuitry required for a self-contained implantable pressure transducer plausible for long term monitoring of ICP.

Prevailing In-Vivo Pressure Measurement Techniques

The mainstay "gold standard" method of assessing ICP is by introducing a catheter, connected to a manometer, into the ventricles of the brain by way of a bore hole though the skull, as shown in Figure 3 [5]. A saline solution is used, if needed, as a translating fluid medium to allow external alignment of the measuring solution with that of the ventricular cavity. Fluid elevation beyond that of the internal cavity ceiling level is then measured to arrive at a pressure relative to atmospheric. This technique allows for robust pressure measurement that is immune to drift and also facilitates drainage relief

if necessary. However, the method is also the most invasive and there have been studies showing an infection rate as high as 40% [6].

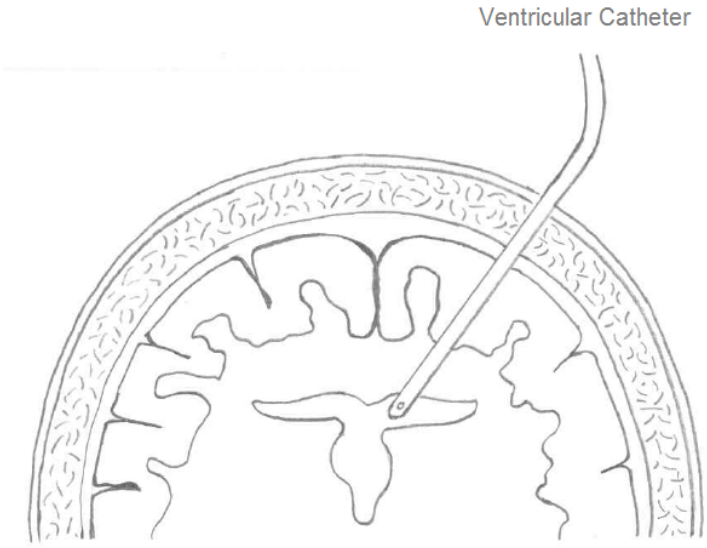

Figure 3 - Intracranial pressure monitoring with a ventricular catheter.

A popular alternative to manometer pressure measurements is that provided by optical pressure transducers, such as those marketed by FISO [7] or Integra LifeSciences [8] (formerly Camino). In this technique, a fiber optic strand with a pressure sensitive tip is inserted into a ventricular catheter or into the parenchyma and is read out by interferometer instrumentation bedside to the patient. Figure 4 shows such a fiber optic sensor whereby the strand is configured with a pressure sensitive membrane that translates relative to incident pressure. A collimated light source present within the fiber

and reflecting off of the sensor membrane varies the amount of reflective constructive or destructive interference. Therefore, the amplitude of the reflected light received at the proximal end is proportional to the pressure present upon the membrane tip. Drift and temperature effects have been widely reported with such sensors, however [5, 2]. Since the fiber optic method is optically based upon interferometry against an absolute pressure reference and given there are no present devices with temperature sensing and correction, the pressure drifts with temperature. Reported drift of fiber optic pressure sensors may for this reason be predominately due to the sensor being "zeroed" ex-vivo at room temperature and then actual pressure assessments taken in-vivo at a temperature of approximately 37°C. Furthermore, since these types of sensors typically deflect more than the thickness of the pressure diaphragm itself in order to reach desired sensitivities, the diaphragm operates within a non-linear range of deflection, which can extend into plasticity and result in hysteresis. Piper reported that their data indicated that more than half of 34 fiber optic pressure transducers explanted had zero drift in excess of 40 mm H_2O [5].

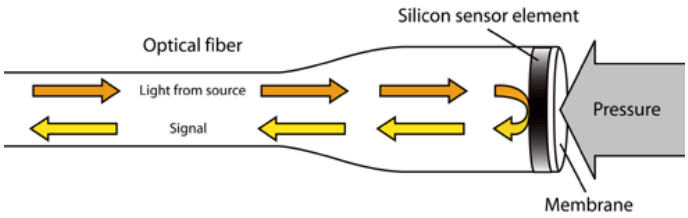

Figure 4 – Fiber optic pressure sensor.
(Source: Sensors by Questex Media Group LLC)

In addition to fiber optic pressure readout systems, additional prevailing techniques include the use of an implantable strain gauge inserted into the brain's ventricles or parenchyma. Commercial offerings, such as those manufactured by Codman (J&J DePuy) [9], offer a titanium probe with a side sensor providing electrical communication of pressure from the transducer to a bedside readout system. The Codman sensor consists of a solid state piezoresistive diaphragm and a Wheatstone bridge readout circuit [2]. As pressure modulates the diaphragm, induced strain changes the resistive properties of the material. The Wheatstone circuit converts this variable resistance into a proportional electrical current representative of the sensor's incident pressure. Advantages of this silicon technique include the option for temperature compensation based upon in-vivo silicon bandgap measurements. Assessments of the Codman strain based sensor have shown minimal drift, an average of 12 mm H_2O, and with pressures that correlate accurately with direct intraventricular ICP measurements [2, 10].

While other methods of ICP exist, including qualitative non-invasive techniques discussed within the Literature Survey, the formerly described intraventricular catheter manometer, fiber optic sensor, or strain gauge sensor all comprise the extent of modern day means of quantitative assessment. As of the time of writing and to the best extent known, there are no commercially available FDA approved self-contained implantable bio-pressure sensors for monitoring ICP. The closest technology for wireless pressure monitoring is that provided by CardioMEMS [11] for the purpose of cardiovascular pressure monitoring, in which the blood pressure range sought is typically much higher than that of ICP. Therefore, prevailing solutions for quantitatively measuring ICP all

require a surgical operation for the insertion of a sensor within the skull and thereafter careful tethered monitoring within a controlled clinical setting.

Literature Survey

Overview

Wiegand [12] provides a comprehensive review, as of 2007, for a sparse set of literature concerning the methods and instrumentation for measuring ICP. Weigand describes intraventricular monitoring as the criterion standard of modern day techniques. However, he also acknowledges its shortcomings with regard to infection rates over time and the difficulty of ventricular cannulation for elevated ICP where a deviated or slit ventricle syndrome is present. Weigand's review covers direct, indirect, and non-invasive techniques for assessing ICP. However, he quickly notes that it wasn't possible, as of the time of writing, to quantitatively measure ICP non-invasively. Rather, he describes non-invasive signs, complimentary to diagnosis, such as clinical history, physical examination, and radiological methods for assessment of elevated ICP.

Non-Invasive ICP Assessment

As a non-invasive, but indirect ICP assessment, sonography techniques allow for the measurement of the optic nerve diameter. Studies [13] have shown that the optic nerve diameter, as assessed by transorbital sonography in the transverse plane, 3 mm posterior to the papilla, is indicative of raised ICP. For patients under normal CSF pressures, the optic nerve sheath was found to have a mean diameter of 3 mm. However, for those patients of increased ICP, the optic nerve sheath diameter was found to average 5 to 6 mm. While this non-invasive technique offers a quick and

inexpensive method of qualitatively indicating elevated ICP, the efficacy of the method requires expert interpretation. Furthermore, Wiegand summarizes that non-invasive methods cannot provide accurate ICP readings as compared with direct techniques, such as ventricular cannulation.

Indirect ICP Measurement

With regard to indirect ICP assessment, Weigand covers techniques involving lumbar puncture, visual evoked potentials, neonatal fontanelle compression, and optic nerve diameter via sonogram as viable methods. Lumbar puncture pressure measurement, which historically is the longest standing method, has substantial accuracy shortcomings, especially for patients under general anesthesia. Czonsnka and Pickard [14] reported misleading ICP for instant fluid column measurements and suggested that such pressures should be averaged over at least 30 minutes and overnight preferably. The delay of visually evoked N2 electrical potentials, as measured upon a patient's scalp, has been correlated to rises in ICP [15]. The issue here, however, is with the setup of the measurement and the interpretation of the delays, which may require neurophysiological expertise. Neonatal fontanelle compression is an ultrasound method whereby an infant's "soft spot" is compressed during Doppler sonography to examine the hemodynamic response. While qualitative in nature, the technique provides a method of assessing progressive or persistent elevations in ICP for neonates with hydrocephalus. However, Weigand again summarizes that indirect methods, similar to non-invasive techniques, still do not provide the accuracy provided by access to the brain's parenchyma or ventricles.

Direct ICP Measurement

Weigand's review also covers a variety of direct measurement techniques for assessing ICP such as the early saline based subdural pressure transducers based upon ventricular cannulation, extradural electrical impedance devices, and also modern day sensors such as the fiber optic [16] or electrical impedance strain transducer [17], which can be used either intraventricular or within the parenchyma. Luerssen describes that these modern day parenchymal sensors are comparable with that of the intraventricular hydrostatic methods and that the complication rate is lower due to the small diameter of the probes and lack of fluid coupling [18]. Luerssen cites Pople [19] and Shapiro [20] as two large studies resulting in less than a one percent infection rate for pressure measurements taken within the parenchyma. For ventricular cannulation, however, Luerssen cites several studies that indicate infection rates can approach ten percent. He explains that the risks of infection increases with the duration of monitoring and for this reason should only be used for as brief a period as possible. He further cited studies showing that prophylactically changing the ventricular catheters used for pressure measurement didn't reduce the risk of infection.

Direct Fiber Optic Measurement

As previously described, fiber optic pressure transduction utilizes a thin diaphragm, often constructed from the silica fiber itself, composing a sealed cavity in order to measure diaphragm deflections from incident pressure against an absolute source. Optical interferometric techniques are used in order to measure the diaphragm translation. Piper questions, however, the efficacy of the fiber optic parenchymal or

intraventricular pressure probes as an accurate direct measurement and reported drifts in excess of 40 mm H_2O for 50% of the pressure probes tested [5] within a period of days. While the manufacturer of the sensors studied specifies an upper bound on drift of ±27 mm H_2O for day one and 13.6 mm H_2O for each day thereafter, Piper claims this is unacceptable for clinical use. Further, researchers have even confirmed zero drift in excess of the specifications in a study of 136 Camino fiber optic sensors with average daily drifts of 43.5 mm H_2O. The study by Piper et. al. showed significant drift bias with a dependence on temperature for the fiber optic sensor. Separate studies indicate a potential reason for such clinical drift is that the absolute pressure sensors are calibrated (i.e. “zeroed”) ex-vivo at room temperature (e.g. ~20°C) and then measured in-vivo at body temperatures, typically at 37°C, where a temperature coefficient of 4 mm H_2O per °C likely results in a pressure error versus the calibration [5]. While this seems likely, there are other possible factors involved in the drift mechanisms of perhaps the optical diaphragm material itself as well as readout electronics and interconnects. For sufficient sensitivity, the optical diaphragm must be very thin. However, in such a case, pressure deflections often are larger than the thickness of the material itself. While small deflections can be predicted linearly as with a normal round circular plate [21], large deflections quickly turn non-linear [22] and can extend into plasticity for the material. Once the deflections become plastic, distortion effects occur where deformity can result in hysteresis and therefore drift. Lastly, atmospheric pressure changes over the course of in-vivo measurements have also been suggested as possible drift factors in the Camino sensor system [23].

Direct Micro-Strain Measurement

In contrast to the direct fiber optic intraventricular or parenchymal probe reviews, micro strain based sensors have received positive appraisals within the literature. Koskinen performed a very large prospective study of 128 patients whereby zero drift was measured explantation [10]. In addition 469 pressure measurements were made within an additional 22 patients with the Codman Microsensor System (i.e. microstrain sensor) that also used an intraventricular manometer [10] at the same time for comparison. Results were shown for the 22 patients for an average ICP of 249±4 mm H_2O measured intraventricularly. The microstrain based device produced an average of 258±3 mm H_2O over the range of patient ICP. The overall mean drift across the span of the study was reported at 12 mm H_2O with bounds less than ±27 mm H_2O in 79% of the devices. Koskinen reported the findings from a clinical point of view as acceptable and that the drift was low. Additional studies were cited, which were in agreement with Koskinen's results.

Other Direct Techniques and Modern Approaches

Capacitive based sensors are not currently prevalent within the industry for ICP measurement, but never the less are a topic of study within the biomems area of research. George, et. al. recently reported their fabrication of a micro-electro-mechanical (MEM) based capacitive catheter sensor for ICP measurement [24]. In this type of sensor, metal upon a silicon die was used to form a variable capacitor whereby one electrode was fixed and a second was moveable in response to fluid pressure. George reported typical sensitivities for such sensors on the order of tens to hundreds

of atto Farads per millimeter of mercury (i.e. 13.6 mm H2O) with a fabrication tolerance of only about ±5%. It's likely that George's results are indicative of why such sensors are not as prevalent within the industry versus those of the strain and optical interferometry methods. George went on to summarize that not only was the sensitivity of their device low and not well controlled, but that a large offset was present as well.

One successful deployment of capacitive based pressure sensing is in the case of CardioMEMS' [11] EndoSure sensor. This sensor represents the latest commercialization work for wireless sensing of cardiovascular pressure monitoring, which incorporates a MEMs based capacitive pressure cell. The sensor is installed with a stent graft during endovascular repair and is entirely passive, consisting only of an inductor, capacitor, and a diode. The sensor operates by ex-vivo wireless power stimulation, which results in a resonant frequency proportional to pressure induced capacitance. The resonance frequency is detected by an external radio receiver, which typically results in a sensitivity of 10 kHz per millimeter of mercury (i.e. 13.6 mm H_2O) [25]. Allen also reports that typical frequencies for such a sensor operates around 30 to 40 MHz and with Q-factors of approximately 50. He indicated ex-vivo readout distances of approximately eight inches. While the EndoSure provides a novel means of cardiovascular pressure interrogation, the pressures associated with that of blood pressure only begin at the extreme maximums of those necessary for ICP.

Micro-Strain Sensing and Readout

Samaun et. al. [26] described some of the early work of silicon microstrain sensing for biomedical instrumentation, in particular for intravascular cardiac measurements. In

their work they developed a thin silicon pressure diaphragm for the measurement of low stress with alternate oriented p-type implanted resistors. They go on to describe proper orientation for achieving magnification of stress measurement through the use of a bridge network in which two resistors decrease resistance with induced strain and the other two likewise increase. Properties of pressure detection with diaphragm mechanics was also thoroughly described whereby sensitivity increases by the square of the ratio of the diameter to the diaphragm's thickness. Additionally, linear regions of operation limited to about 40% deflection compared to the thickness was described. The researches fabricated two piezoresistive sensors in which a sensitivity of 83 μV/Vsupply/mmHg and 14 μV/Vsupply/mmHg was achieved for diaphragm diameters of 1.2 and 0.5mm, respectively. After calibration and temperature compensation their work resulted in pressure sensors accurate to within 1 mmHg (13.6 mm H_20) and with a range of up to 150 mmHg (2,039 mm H_2O). Samaun also described drift issues with the silicon microstrain sensing technique where temperature sensitivity of the diffused piezoresistors was significant, but correctable. Additionally, Samaun found that mechanical creep due to different expansion coefficients between the sensor and mounting also contributed to drift over time and could very well dominate long term drift.

Yurish [27] reviewed a variety of techniques in the readout of piezo-resistive strain sensors. His review covered high end analog to digital approaches and more cost sensitive microcontroller readout techniques. However, he cautioned against clock trigger noise affecting readout with microcontroller techniques. Yurish provided an overview of modern day application specific integrated circuits available through

commercial means for dedicated readout of microstrain sensors. Most of the ASICs were digital outputs with either I^2C or SPI. He cited Smartec as offering a pulse width modulated (PWM) output, but that it was only compatible with resistive bridges ranging from 10Ω to 250Ω. Yurish noted that often, for remote sensing applications, the sensor signal is converted to a frequency or duty cycle signal. Yurish's work consisted of developing a variable frequency output, representative of the entire bridge resistance, with a variable duty cycle, representative of the bridge's unbalance for a very wide variety of bridge parameters. In this way, Yurish approached the problem of bridge temperature variation by encoding the common mode effects into the circuit's frequency output and then the bridge's strain signal into the duty cycle.

Similar to Yurish, Crescini et. al. [28] also developed a readout circuit for a piezo-resistive pressure sensor, but with the intentions of high temperature applications. Crescini's readout circuit measured the overall bridge resistance of the sensor and encoded this into an output square wave carrier frequency. The duty cycle of the square wave depended upon the imbalance within the bridge, representing the incident pressure. Crescini, in agreement with Yurish, explained the advantage of such an approach in that the electronics can be located safely away from the sensor with a minimal degradation in accuracy. Important to Crescini's application was that the implied temperature was encoded by the carrier frequency. Crescini claimed the sensor's output transmission was highly noise-immune and could be directly interfaced to a microcontroller for A/D conversion.

Non-Invasive Transponder Techniques

Non-invasive means of communication with human implantable devices have been shown within the art comprising optical means and inductive or high frequency radio techniques as reviewed by Townsend [29]. With regard to pressure readouts, the previously cited CardioMEMS for arterial blood pressure operated as a battery-less transponder, excited by ex-vivo radio frequency (RF) energy in which the transponder then responds with a resonant frequency proportional to a capacitive pressure sensor in parallel with an inductor. In a similar means, DeHennis and Wise [30] reported of an arterial blood pressure measurement means, also consisting of a vacuum sealed capacitive to frequency transponder, utilizing a backscatter modulated passive telemetry device, consuming only 340 μW. Illustrations of their device showed an approximate 5 mm^2 rectangular coil for inductive/RF coupling.

Many of the inductive power coupling means surveyed within the literature use an external Class E output to generate sinusoidal power signals to couple with in-vivo antennas with subsequent rectifiers and regulators. Ghovanloo et. al. [31] details such a circuit for an implantable CMOS integrated circuit (IC) offering rectification with back telemetry for RFID or other biomedical applications. The back telemetry utilized the same antenna as the power reception via load shift keying (LSK), which modulates the load of the receiving antenna. The modulated load reflects back to the ex-vivo transmitter as an alternate secondary impedance, which can be demodulated similar to amplitude modulation. Ghovanloo detailed the design's antenna parameters, their circuit design, as well as their measurement results.

Power transfer with inductive telemetry techniques have also been demonstrated by Hussnain, et. al. [32] where they achieved a 40 mW back-telemetry response with a small 24 turn antenna at the transponder. Hussnain used a Class E ex-vivo transmitter of 100 mW to achieve a 40% back link efficiency. Their circuit, including rectification, measurements, and complete antenna parameters are provided within their paper along with illustrations of an approximate thumb size antenna. Additional power transfer metrics was demonstrated by Wang et. al. [33] where they achieved an implantable 250 mW transfer with greater than 15V on the secondary also utilizing an external Class E transmitter. They developed an optimization circuit for power transfer based upon load requirements in which they modulated a DC-DC converter to achieve up to 66% coupling efficiency. They also achieved 250 mW without the optimization, but at a 36% link efficiency. Their design also incorporated load shift keying for readout of transponder data and the parameters of their antenna, as well as circuitry, are outlined within their paper. With regard to achievements in voltage regulation circuitry and load regulation, Van Ham and Puers [34] demonstrated a transcutaneous inductive transfer design capable of 2.1% load regulation with a line regulation of 3.7 mV/V. Additionally, their circuit design achieved a power supply rejection ratio (PSRR) at the carrier frequency of 1MHz is as high as 61 dB.

Chapter 3 - Methodology

Overview

The goal of this thesis is to evaluate the sensing and electronic readout potential for a long term implantable bio pressure sensor for low pressure resolutions (i.e. < 13 mm H_2O), for non-invasive intracranial pressure readout. Given the consensus provided within the literature, which describes that intraventricular sensing yields the most accurate ICP, a ventricular catheter design in communication with a subcutaneous pressure transponder would satisfy the prerequisite for an accurate ICP measurement based upon a physiological point of view. The pressure sensor utilized in such a configuration would require an accurate biocompatible pressure transducer, capable of communicating through bodily fluid and tissue, with high signal to noise integrity, low drift, and low operating power over the range of intracranial pressures. Based on the literature, out of all the various techniques and methods of quantifying ICP, there are two dominant transduction means with the sensitivity required for measuring CSF pressure: fiber optic and micro-strain sensing, both based upon diaphragm translation.

Results from Koskinen and Olivecrona show micro-strain sensing to offer the lowest drift measurements over time and temperature, except for the manometer, when compared to other literature results against fiber optic means. Furthermore, micro-strain sensing offers a bio-compatible interface to CSF and brain tissue. Therefore, in an effort to accomplish the goal of this work, micro-strain sensing will be evaluated as a possible solution. Given the sensor will only be dedicated for readout diagnostics, external powering and passive interrogation is acceptable, which simplifies and improves the

reliability and cost of the implantable design. Therefore, an inductive, or optionally, an optically powered biocompatible silicon micro strain sensor with a radio frequency (RF) or optical readout would provide a basis for which to evaluate a concept to satisfy the transponder goal. Based upon the literature review, much success within the inductive and RF telemetry approach has been demonstrated with power couplings up to 250 mW offering a compatible range to satisfy the biosensing.

Approach

Sensor

Micro-strain pressure sensors are based upon measuring the strain within the deflection of a pressure diaphragm. This is often accomplished by measuring the conductivity of a resistive foil pattern joined to a non-conducting pressure diaphragm substrate. Figure 5 illustrates an example resistive pattern in which two electrical terminals are provided to the left of the figure, which are connected to an interwoven conductive design. The resistivity of the segments is given by Ohm's law:

$$R = \frac{\rho l}{A}$$

where ρ is the specific electrical resistance of the material, l is the length, and A is the conductor's cross sectional area. When lateral forces (i.e. horizontal to the page) extend the design, the interwoven conductive lines become elongated, resulting in a longer more narrow line, which increases resistance. Alternatively, when lateral forces compress the design, the lines broaden and shorten, thereby decreasing resistance [35]. The serpentine layout serves to increase the gain of the sensor since strain

applied to the sensor not only affects one resistive line, but multiple parallel lines in series, as well.

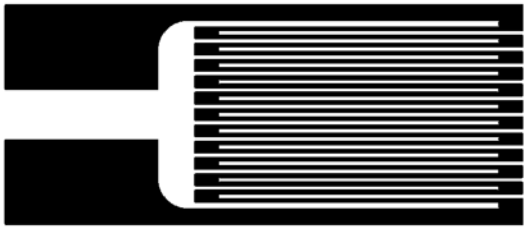

Figure 5 – Typical micro-strain resistive pattern.

The gauge factor is essentially the gain of the device providing the change in resistance for an applied strain. The gauge factor is defined as:

$$GF = \frac{\frac{\partial \rho}{\rho}}{\varepsilon}$$

where ε is the applied strain to the device.

Pressure transducers utilizing a diaphragm with strain gauges typically employ four such strain sensors allowing the formation of a Wheatstone bridge [36]. The diaphragm is usually designed such that two strain sensors increase in resistance with incident pressure, while the other two sensors decrease resistance, thereby increasing the gain of the overall transducer.

Figure 6 illustrates a schematic of a pressure transducer's resistive strain sensors arrangement into a Wheatstone bridge. Sensors designated by R1 and R3 decrease resistance upon incident pressure to the transducer's diaphragm. R2 and R4, however, increase resistance and therefore improve the sensitivity of the transducer.

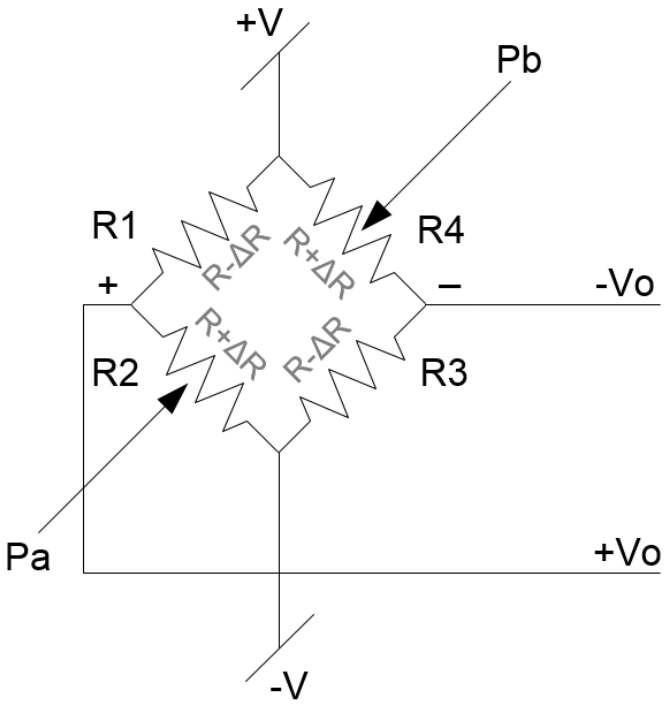

Figure 6 – Pressure transducer strain sensor configuration for a Wheatstone bridge.

Letting Vo = +Vo – (-Vo) and a supply voltage Vs = +V – (-V), it can be formulated from the schematic:

$$V_o = V_S\left(\frac{R_2}{R_1 + R_2} - \frac{R_3}{R_3 + R_4}\right)$$

The output voltage is zero when the bridge is in balance according to the condition:

$$\frac{R_1}{R_2} = \frac{R_3}{R_4}$$

A change in resistance for each of the four strain sensors results in:

$$V_o = V_S\left(\frac{R_2 + \Delta R_2}{R_1 + \Delta R_1 + R_2 + \Delta R_2} - \frac{R_3 + \Delta R_3}{R_3 + \Delta R_3 + R_4 + \Delta R_4}\right)$$

If $R_1 = R_2$ and $R_3 = R_4$ then expanding the equation above and substituting provides:

$$V_o = V_S\left(\frac{R_1(\Delta R_3 + \Delta R_4) - R_3(\Delta R_1 + \Delta R_2) + 2R_3\Delta R_1 - 2R_1\Delta R_4}{4R_1R_3 + 2R_1\Delta R_3 + 2R_1\Delta R_4 + 2R_3\Delta R_1 + 2R_3\Delta R_2}\right)$$

By making an assumption that $\Delta R/R << 1$ and that $R_x \bullet \Delta R_y << R_x \bullet R_y$, then the expression above can be shown [37], with corrections, to simplify to:

$$\frac{V_o}{V_S} = \frac{1}{4}\left(\frac{\Delta R_1}{R_1} - \frac{\Delta R_2}{R_2} + \frac{\Delta R_3}{R_3} - \frac{\Delta R_4}{R_4}\right)$$

And by utilizing the gauge factor, GF, the expression further simplifies to:

$$\frac{V_o}{V_S} = \frac{GF}{4}(\varepsilon_1 - \varepsilon_2 + \varepsilon_3 - \varepsilon_4)$$

Therefore, this simplified derivation relies upon two important points: that the two bridge leg resistances are equal and that R is quite large such that $\Delta R/R$ is very small. Furthermore, in order to improve temperature stability, it is preferable that all four resistances be equal [35].

In selecting a pressure sensor for ICP monitoring, the following considerations must be taken into account:

1. Miniature size.
2. Biocompatible materials.
3. Compatible over the range of CSF pressures.
4. High sensitivity and resolution.
5. Low drift over time.

Given that the pressure sensor is intended to be implanted, temperature compensation is not of primary importance, so long as the sensor is stable over normal body temperatures. Lastly, a sensor meeting the objectives of this research would satisfy the foregoing assumptions of equal strain resistances of a relatively high resistance, but not such as to create undue thermal noise, thereby depleting resolution.

The deployment of the pressure transducer is intended to be in fluid communication with the ventricles by way of a ventricular catheter. As repeatedly found within the literature, ventricular cannulation remains the “gold standard” of ICP. Although Luerssen cited infection rates of up to ten percent in ICP monitoring through ventricular cannulation, these findings were based upon lengthy (i.e. several days) open incision ICP measurements and not for an entirely implantable device. Hydrocephalus patients who undergo ventriculoperitoneal shunting often possess ventricular catheters, infection free, for years. Therefore, this design will incorporate a subcutaneous pressure transducer just under the scalp, connected to a ventricular catheter. Figure 7 illustrates the

intended deployment of the bio-pressure transponder. In the figure there is shown a right angle pressure connection to a ventricular catheter. These types of catheters are typically of one millimeter inner diameter Silastic. The figure further shows a barometric fluid bladder for use with a differential pressure sensor that's offset by atmospheric pressure. However, nothing in the transponder design prevents an absolute pressure sensor, having a sealed pressure reference, from being utilized in order to eliminate the bladder. Never the less, it is quite common that subcutaneous flexible fluid chambers are used in the case of shunting to allow flushing of shunts with the use of occluders. Furthermore, since such a bladder would be placed at or near the top of the head, it's not expected that incidental pressure would be of any issue such as in other parts of the body. Therefore, this design will plan to incorporate a differential pressure valve and utilize a barometric bladder in order to allow a much smaller pressure range so as to improve resolution. Such a pressure range, according to the literature review, would typically span from ~60 mm H_2O to over 500 mm H_2O for severe hyper intracranial pressures. In the case of an absolute pressure sensor, these pressures would be in addition to the full range of barometric conditions possible. Such ranges can span from 0.86 atmospheres up to 1.06 atmospheres [38, 39, 40]. These pressures would correlate to an absolute pressure sensor capable of 8,872 mm H_2O on the low end up to 11,472 mm H2O for the highest recorded atmospheric pressure including 500 mm H_2O. Therefore, utilizing the barometric bladder allows for an order of magnitude lower pressure range, which would possibly allow for higher resolutions over a smaller span of pressures.

Table 1 outlines the basic requirements for the pressure sensor based upon the pressure ranges described, as well as the desired resolutions and drifts interpreted from the literature. Based upon the criteria, selection of currently available sensors was quickly limited by the pressure ranges and resolutions necessary for CSF measurement, especially with regard to physical size. Only two commercial manufacturers were identified as potential candidates possessing the aforementioned qualities. The two manufacturers identified were Measurement Specialties of Hampton, Virginia and All Sensors of Morgan Hill, California.

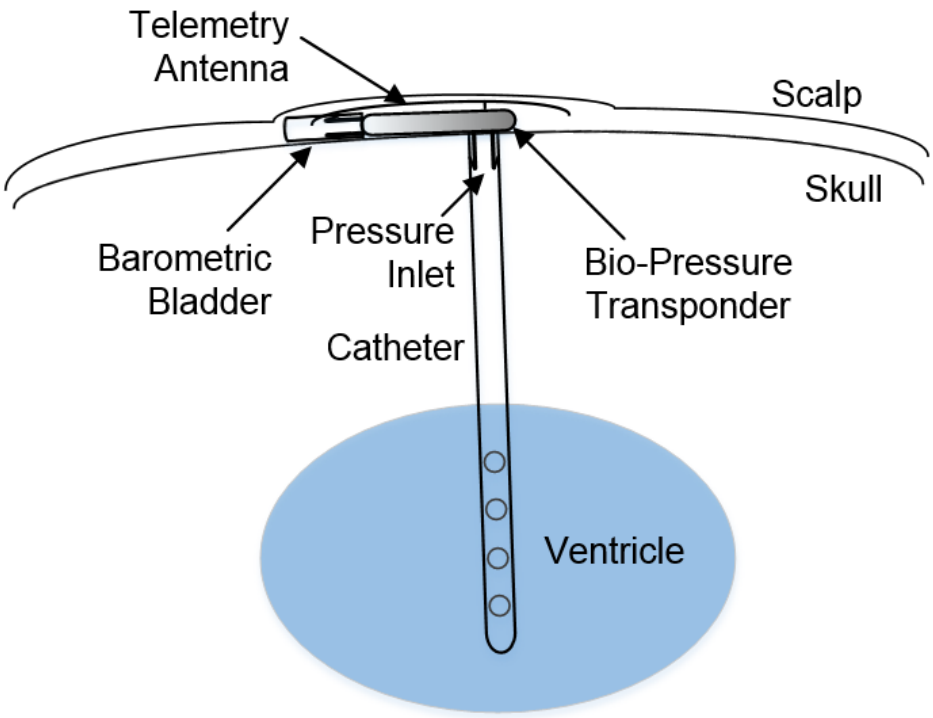

Figure 7 – Bio-Pressure transponder deployment.

Measurement Specialties produces a range of bare die MEMs pressure sensors in both absolute and differential configurations. The closest sensing range device offered was the MS763, which uses a piezo-resistive approach, providing a 0 to 300 mmHg range. The device is marketed for use as a biocompatible implantable pressure sensor and offers all connections on one side of the die. The die size is 1.0 x 2.20 mm^2 and is specified with a 3kΩ bridge resistance, thereby indicating that each strain resistor in the bridge is also 3kΩ. The device specifications, unfortunately don't indicate a drift specification and the pressure range is almost ten times the intended range of the ventricular bio-pressure sensor. The full scale span of the sensor for 5V operation is specified to be 18 to 27 mV with 22.5 mV typical.

Table 1 – Basic requirements for the selection of an ICP bio-pressure transducer.

Merit	Figure	Units
Type	Differential BioCompatible	
Size	< 1	cm^2
Tranduction	Micro-Strain	
Pressure (low)	60	mm H_2O
Pressure (high)	> 500	mm H_2O
Resolution	< 20	mm H_2O
Drift	< 5	mm H_2O per year

All Sensors also produces biocompatible pressure transducers based upon a micro-strain gauge approach that are marketed for low drift performance with what the manufacturer claims as a trade secret in the construction of the sensor that alleviates long term mechanical creep. Further, their low voltage series of sensors allows for 5V operation, which is preferred versus their 12V sensors since a lower operating voltage will reduce quiescent power conditions in the transponder design as well as ease requirements of telemetry power transfer. Various ranges are offered by All Sensors within the span of several inches of water pressure. The MLV-L30D operates within the ±30 in H_2O (i.e. 762 mm H_2O) and has a corresponding output signal between 19 and 21 mV with 20 mV typical. Very importantly, All Sensors specifies the sensor for long term drift of ±100μV over a one year time period. Translated over the full scale range of the device, this figure indicates an expected drift of ±3.8 mm H_2O per year. The device is temperature compensated and very importantly can be parylene coated, which not only offers biocompatibility, but is also resistant to bio-matter. Specifications indicate the bridge input resistance is 12 kΩ with an output of 3 kΩ, which as shown later within the Timing Electronics section, results in a 3.5 kΩ strain resistance. Compared to Measurement Specialties, this sensor utilizes a higher strain resistance, which improves linearity as shown within the bridge derivation above whereby a $\Delta R/R << 1$ results in the output essentially becoming a product of the strain, ϵ, and gauge factor, GF. Further, when compared with Measurement Specialties, the MLV-L30D provides greater gain since the sensor's span is 762 mm H_2O versus the large range of the MS763 (4,079 mm H_2O) for what is a very similar sensor output. Lastly, when compared to

Measurement Specialties, the MLV-L30D specifies a long term drift value that's acceptable within the intentions of the ventricular bio-pressure transponder. Figure 8 shows a picture of the All Sensors die used within the MLV-L30D, utilizing two center micro-strain sensors and two pairs of micro-strain sensors along the periphery.

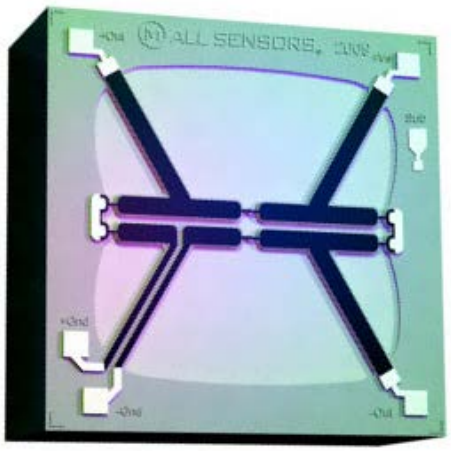

Figure 8 – All Sensors MLV-L30D pressure sensor die, approximately 2 mm^2.

Therefore, the All Sensors differential MLV-L30D was chosen for the design with a sensitivity of 2.62uV/mm H_2O, a span of ±762 mmH_2O, 3.5 kΩ strain resistances, 5V operation, and parylene biocompatibility in a package of approximately 2 mm^2. With regard to resolution, the sensor is specified with a linearity and/or hysteresis error of 0.30% FSS, which equates to 2.3 mm H_2O. Complete specifications of the device are provided within the Appendix.

Implantation and Deployment

Figure 7 illustrates the general approach intended for human implantation, as described within the former section, whereby a ventricular cannulation is utilized to access the most precise ICP available, according to the literature review. The cannulation allows for a subcutaneous transponder design for improved telemetry coupling when compared to a deep implant. The pressure transponder is intended to be titanium encased with a glass seal for a telemetry antenna. All pressure interfaces would be parylene coated for a low bio-affinity and biocompatible interface.

Shown in Figure 7 is the pressure transponder along with an antenna for inductive coupling. Although the design, given its subcutaneous placement, could be a candidate for optical coupling, hair upon the scalp could significantly impede such an approach. Therefore, this design will be intended for an electromagnetic telemetry approach for both power, via inductive coupling, and high frequency pressure readout communications. Therefore, the transponder will be entirely passive without any internal power source.

Due to the non-invasive transponder approach, the deployment necessitates low power consumption with a high signal to noise ratio output. Therefore, the design approach must minimize the readout electronics while encoding the pressure data in an optimized way to avoid interference from other wireless devices or noise. While a digital output would be preferred by way of frequency, phase, or amplitude shift keying, such an approach would add significant circuitry to the back-end of the transponder, increase power consumption compared to other potential analog methods, and potentially

decrease reliability due to complexity while increasing cost. Therefore, an analog approach is preferred for this design in order to negate these consequences. Amplitude or frequency modulation are two approaches, which would satisfy the general approach. However, amplitude modulation is very susceptible to extraneous noise, while frequency modulation could be susceptible to carrier drift. Alternatively, a fixed A.C. frequency pulse width modulation (PWM) scheme would be significantly immune to signal output amplitude, due to coupling variations or interference, and also to a certain extent, carrier drift.

Figure 9 illustrates the concept of the transponder and readout deployment whereby the pressure sensor is amplified and compared to a ramp or sweep signal. The comparator therefore acts as an amplitude-to-time converter and gates a fixed frequency oscillator for transmission of a temporally encoded pressure signal to a readout device ex-vivo, which then demodulates the signal and transposes it into a human readable form. The telemetry units also transfers power inductively from the readout device into the transponder.

In this deployment, a low power front end analog circuit is expeditiously converted into a temporally encoded pressure signal that's significantly immune to noise encountered by the telemetry transfer and the signal to noise is primarily dominated only by the front end amplitude noise, gate jitter, and is optimized by the readout's band pass filtering.

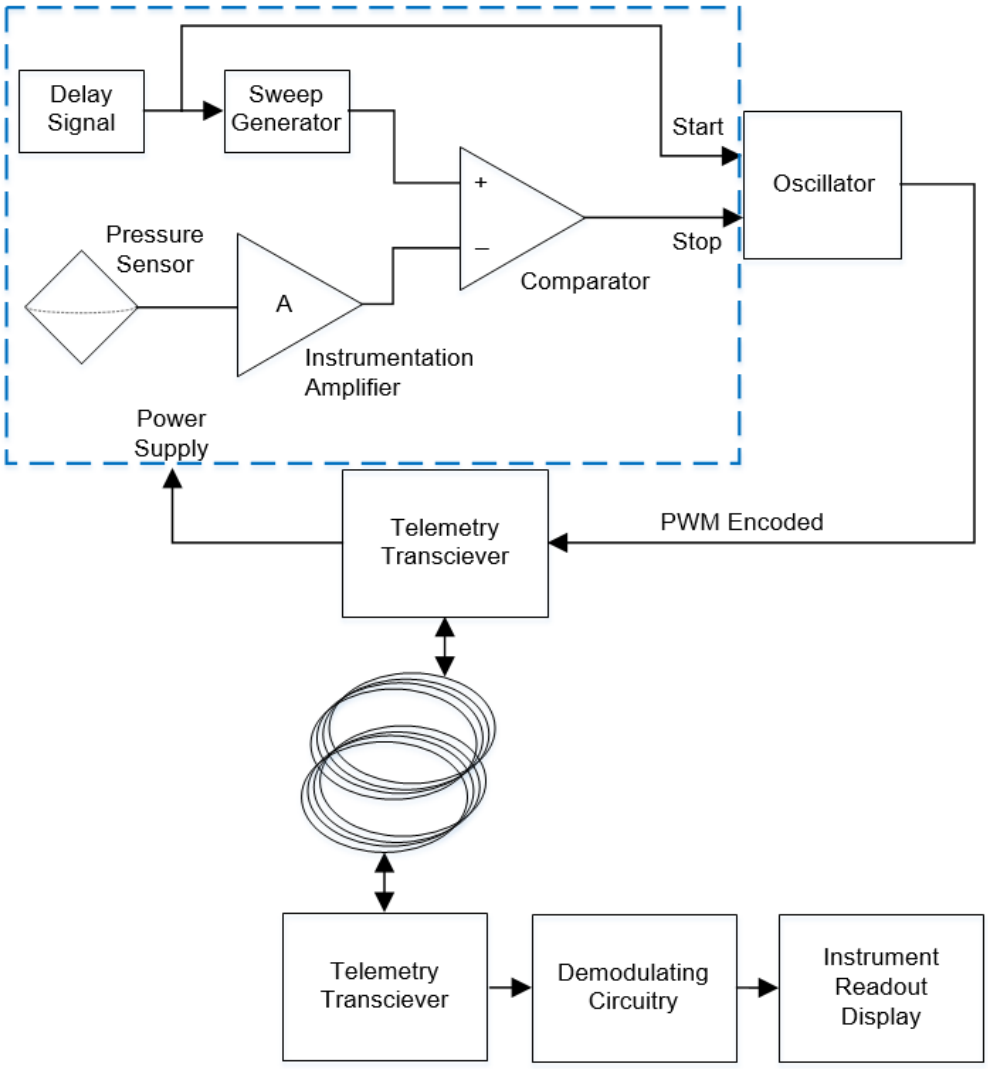

Figure 9 – Transponder and readout deployment block diagram (research focus outlined in blue).

Electronics Readout Overview

The readout of ICP pressure according to the deployment described within the prior sections is comprised of a two part assembly. The first encompasses the ex-vivo

powering and demodulating unit for physician or patient use and interpretation. The second consists of the implantable pressure transponder, which receives power from the first and responds with a pressure encoded signal. The transponder's circuitry is the object of research within this thesis.

Figure 9 lays out the general approach of the pressure transponder and readout mechanism. Beginning with the sensor, its output signal is fed into an amplifier which then supplies an analog representation of pressure to a comparator. The non-inverting leg of the comparator comprises a delay signal to accommodate the settling of the pressure sensor, which then triggers a sweep generator consisting of an analog ramp output. Once the sensor has settled, the sweep generator begins a ramp signal which is compared with the sensor's amplified output. Since the sweep generator is an analog ramp as a function of time, the output of the comparator is a time mark proportional to the amount of time necessary for an equal comparison between the sweep signal and the pressure analog signal.

As shown in Figure 9, a Start and Stop signal is generated in which the period is proportional to the sensor's pressure. The Start and Stop can be utilized to gate an oscillator such that its output is a carrier frequency transmitting through a telemetry antenna for a time period determined by the transponder's pressure input.

The power of the transponder is supplied by the telemetry transceiver in which a relatively low frequency, as compared to the signal output, is received by the antenna and rectified for regulation as to provide a stable supply voltage to the core circuitry.

The investigation of this thesis is focused upon the identification of a stable means of very low pressure transduction suitable for long term ICP measurement and a low power method of encoding the pressure signal for a high signal to noise compatible mode of transmission by means of telemetry. The extent of Figure 9 addressed within this research is the transponder up to the point of Start and Stop since there are several examples explored with the literature review for means of transcutaneous transmission of power and signal.

Analog Channel Electronics

Amplification of the sensor's low voltage signal is necessary in order to produce an adequate signal-to-noise ratio with a low output impedance voltage driver for the remainder of the transponder circuit to utilize. The sensor's output is a differential signal generated by a Wheatstone bridge and an amplifier with a very high input impedance minimizes input loading effects. Since the sensor's output signal is only 26.2 μV/mm H_2O, a high gain is needed very close to the sensor in order to boost an unadulterated sensor signal above the noise floor inevitably present within the remainder of the transponder's circuit. Furthermore, it is necessary to amplify the sensor's signal in order to produce a practical comparison of the pressure signal to the timing channel's ramp output. Since the pressure sensor is intended to operate within a relatively stable pressure environment and with a sample and read approach, a low bandwidth analog channel is all that's required, which helps to reduce power and noise. With these considerations in mind, an operational amplifier topology was evaluated in a differential

mode. Figure 10 shows the topology of an operational amplifier differential configuration.

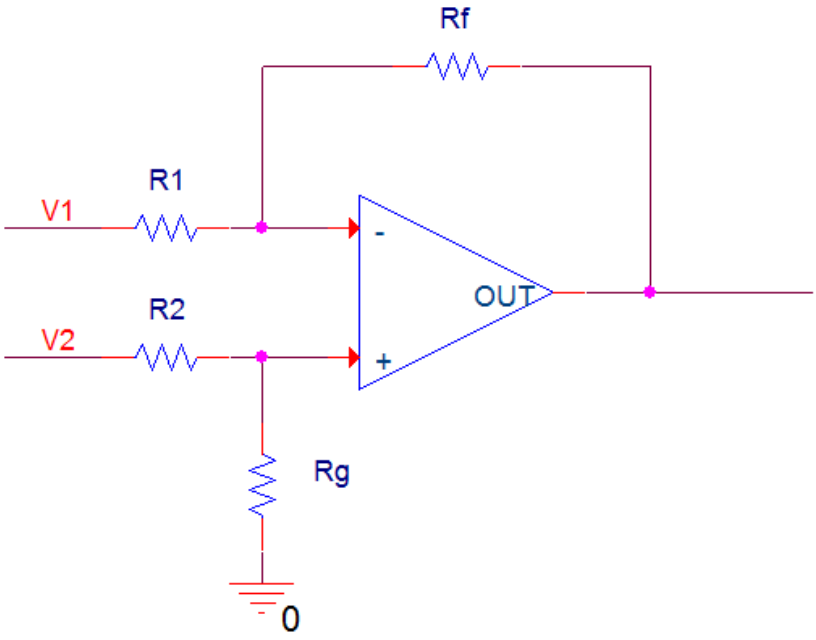

Figure 10 – Operational amplifier differential configuration.

For the differential amplifier, as shown in Figure 10, the gain is given by:

$$\frac{v_o}{v_1 - v_2} = -\frac{R_f}{R_1}$$

and the input impedance is:

$$R_{diff} = R_1 + R_2$$

Since this design is seeking a very high input impedance, as well as a high gain, it can be quickly seen that in order to have a high gain with a high input impedance, R_f would quickly become huge. A large resistance can be challenging to control and in the deployment of an implantable transponder, such a large resistance determining the gain could become detrimental when considering moisture intrusion may affect its value.

An alternative approach to buffering the sensor's differential signal is the use of an instrumentation amplifier as shown in Figure 11. For a CMOS or JFET instrumentation amplifier, the input impedance looking into the non-inverting inputs is nearly infinite with extremely low bias currents and therefore the gain of the amplification stage is independent of the input signal's impedance. The second stage of the instrumentation amplifier is simply the differential amplifier of Figure 10.

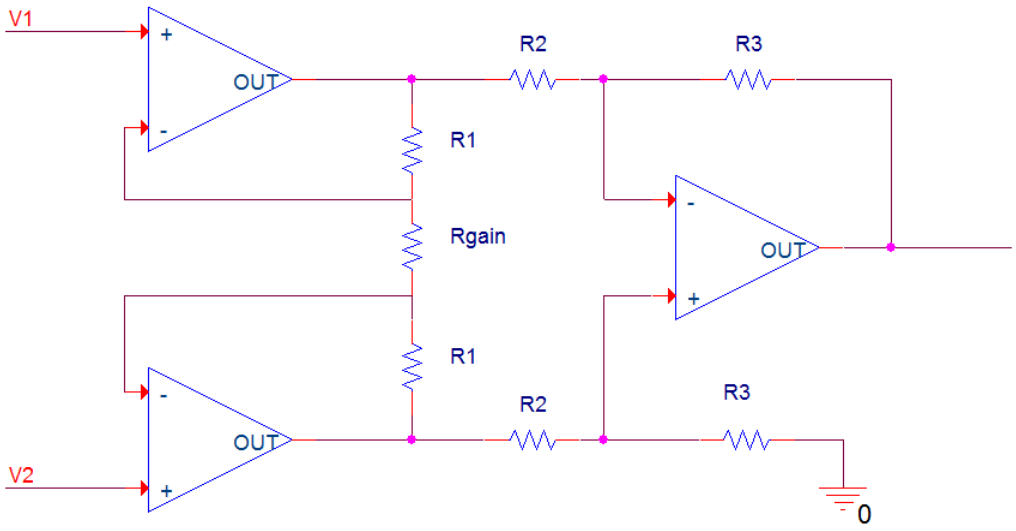

Figure 11 – Instrumentation amplifier.

The gain of the instrumentation amplifier can be shown [35] to be:

$$\frac{v_{out}}{v_1 - v_2} = -\frac{R_3}{R_2}\left(1 + \frac{2R_1}{R_{gain}}\right)$$

Therefore the gain of the amplifier can be adjusted by one resistor, which is typically external for instrumentation amplifier integrated circuits (IC). In addition to very high input impedances and a topology allowing high gains, it can also be shown [35] that the instrumentation amplifier possesses very high common mode rejection (i.e. ≥ 100 dB typically) in cases where the amplifiers gain resistors are very well matched, as is typically the case in modern ICs. An additional benefit of the instrumentation amplifier is the node presented by R3, whereby a ground connection can be substituted with an offsetting reference. As will be seen later in the design, this feature becomes attractive to allowing low voltage operation of the transponder. The downside of the instrumentation amplifier is that it can be more power consuming and potentially more expensive.

A search was conducted for a low power, low offset voltage instrumentation amplifier with a high gain potential (i.e. >10) to mitigate the transponder's typical noise floor. A noise floor of >1 mV rms over a bandwidth of 1 MHz at the output of the amplifier was anticipated for the transponder circuit design, thereby necessitating a gain of 100 or more. In consideration of the dynamic range, however, a gain of 100 for a sensor spanning 20 mV would necessitate an output voltage swing of 2V. Counteracting this dynamic range is the desire to minimize the power supply rails in order to minimize the circuit's quiescent current and transmission efficiency necessary for the telemetry power

unit. As provided by the operation of the pressure sensor, a 5V design was sought since this is the minimum recommendation for the sensor. Additionally, in order to reduce any common mode effects a split power supply of +2.5V and -2.5V was desired. Therefore, these goals constrained the gain of the instrumentation amplifier to what can be supported with regard to rail to rail operation of an amplifier.

Figure 12 shows a narrowed selection of instrumentation amplifiers from the conglomerate Texas Instruments (TI). The selection was narrowed based upon low power and then evaluated for the other requirements. The INA-141 was selected as an evaluation candidate since it possessed a low noise figure, high CMRR, low input bias currents, supports split power supplies less than 5V total, offered a very low offset voltage of only 50μV, and was commercially available.

Compare Parts	INA126	INA141	INA129-EP
Status	ACTIVE	ACTIVE	ACTIVE
Vs (Min) (V)	2.7	4.5	4.5
Vs (Max) (V)	36	36	36
Input Bias Current (+/-) (Max) (nA)	25	5	5
Input Offset Drift (+/-) (Max) (uV/Degrees Celsius)	3	0.5	0.5
Noise at 1kHz (Typ) (nV/rt(Hz))	35	8	8
CMRR (Min) (dB)	83	117	120
Non-Linearity (+/-) (Max) (%)	0.002	0.002	0.002
Bandwidth at G=100 (Min) (kHz)	9	200	200
Iq (Typ) (mA)	0.175	0.75	0.7
Rating	Catalog	Catalog	HiRel Enhanced Product
Pin/Package	8PDIP 8SOIC 8VSSOP	8SOIC	8SOIC
Operating Temperature Range (C)		-40 to 85	-55 to 125
Approx. Price (US$)	1.05 | 1ku	3.55 | 1ku	

Figure 12 – Low power instrumentation amplifiers from Texas Instruments.

The dynamic range of the INA-141 offers, in the worst case, VDD-1.4 and VSS+1.4. So in +2.5V and -2.5V supply rails, the output dynamic range could swing +1.1V down to -1.1V. Therefore, a gain of 100 was nearly the maximum dynamic range afforded by the instrumentation amplifier, but would suffice to boost the sensor's signal above the minimum anticipated noise floor or >1mV rms. The reference could be utilized to offset the amplifier's output signal to a -1V level, in consideration that the pressure sensor always outputs a positive pressure signal referenced from ground.

Timing Channel Electronics

As shown in Figure 9, the timing channel consists of the delay generator, sweep generator, and comparator circuit. The selected sensor specifications indicate a typical settling time of 500 μsec for 10 to 90%. Consequently, a delay generator is necessary to prevent the timing conversion from occurring while the sensor is still yet settling. In an effort to minimize any error induced by sampling the sensor's output signal, it was desirable to understand the settling time of the sensor to less than 1% error. The 10 to 90% rise time of a circuit modeled by a single time constant (e.g. an RC circuit) can be described by:

$$t_{rise} \cong 2.2\tau$$

Since the sensor manufacturer specifies a 500 μsec 10 to 90% rise time, a single time constant estimation was calculated. Substituting into the equation results in a τ of 228 μsec. For less than a 1% settling, more than four exponential time constants are

required and therefore, five was chosen in order to arrive at a metric necessary for the delay circuit. Five time constants results in a delay of 1.14 msec.

Taken a step further toward modelling the sensor, the sensor manufacturer specifies an input impedance of 12kΩ and an output impedance of 3kΩ. All Sensors also shows a schematic representation of a bridge circuit with series resistors on the power supply inputs. Likewise, to model the sensor, the schematic was replicated and strain resistances of 3.5kΩ along with 4.25kΩ input resistors was used to replicate the equivalent 12kΩ input resistance while presenting a 3kΩ output impedance. Since a single time constant circuit can be configured from an equivalent resistor and capacitor, then a capacitor can be derived from the single time constant equation of 500 µsec = 2.2•3kΩ•C, where C equates to 76 nF. The manufacturer's model of the sensor is shown in Figure 13, while the derived model is shown in Figure 14.

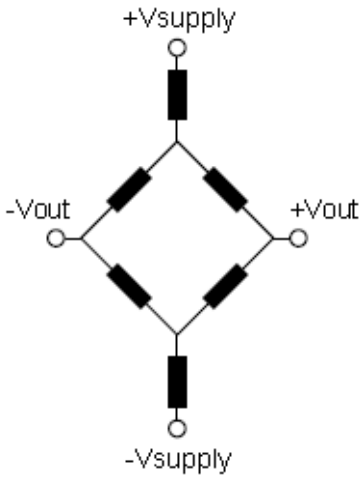

Figure 13 – All Sensors published equivalent circuit.

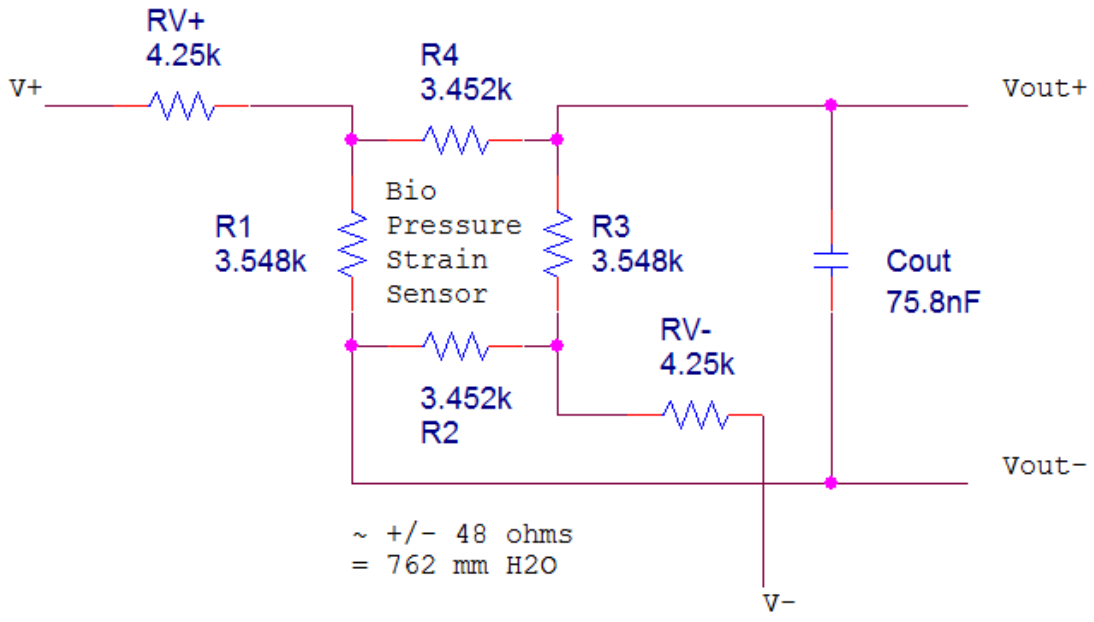

Figure 14 – Derived sensor model (values shown for approximately 762 mm H_2O).

In order to provide a sharp edge timing delay, the timing circuit of Figure 15 was conceived by utilizing a comparator and a single time constant RC circuit. The voltage produced by R5 and C2 behaves according to:

$$v_c(t) = VDD(1 - e^{-\frac{t}{RC}})$$

Since R6 and R9 compose a simple resistor divider between VDD and ground, V(R9) = 1.25V for a +2.5V VDD. Arbitrarily choosing C2 for a standard value capacitor at 100 nF provides for a value of R5 at 14.4kΩ to result in a 1 msec delay. It will be shown later in the timing channel that a benign portion of the ramp circuit produces the additional delay necessary for the 1.14 msec. Never the less, the delay essentially just

needs to allow the sensor to stabilize and is not an essential timing constraint from an encoding point of view, since it will be later seen that this delay will produce a Start signal. The nearest standard 1% value resistor is a 14.3kΩ and again, given the lack of precision necessary in the Start of conversion, the standard value should suffice without necessitating multiple resistors for exact values.

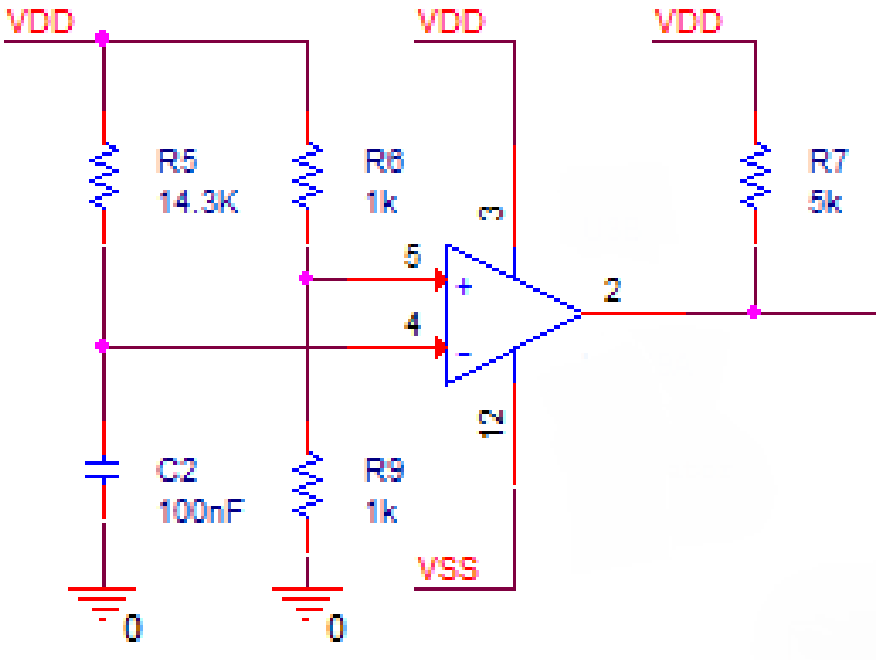

Figure 15 - Delay signal comparator circuit.

The sweep generator block develops a ramp output signal in order to sweep the Stop comparator against the buffered sensor output signal. Therefore, this circuit sets the gain of the output modulation since the slope of the ramp correlates to the amplitude of

the pressure measured. The ramp time was selected based upon anticipating a microcontroller based telemetry readout unit used ex-vivo. A survey of traditional and current microcontrollers was conducted in order to arrive at a fast frequency typically supported by basic microcontroller timers. It was found that most of the basic microcontrollers supported at least up to 8 MHz timers, correlating to a period of 125 nsec. Choosing a factor of four for encoding a millimeter of water signal output from the sensor resulted in a ramp of 500 nsec/mm H_2O. Therefore, the uncertainty in demodulating the encoded signal by a typical microcontroller is ¼ of a millimeter of water. Given the sensor spans 762 mm H_2O, this results in a ramp of 381 μsec in total for a signal span of 2V post sensor amplification.

In order to generate the ramp signal, several different types of ramp generators were considered, including discrete Miller capacitance types. However, the stability of an operational amplifier over the full dynamic range desired ultimately prevailed and the circuit of Figure 16 was developed.

Figure 16 illustrates an operational amplifier integrator, which behaves according to:

$$v_o(t) = -\frac{1}{RC}\int_0^t v_i(t)\,dt - V_C(0)$$

which for a constant $v_i(t)$, becomes V_i and the integral evaluates to:

$$v_o(t) = -V_i\frac{t}{RC} - V_C(0)$$

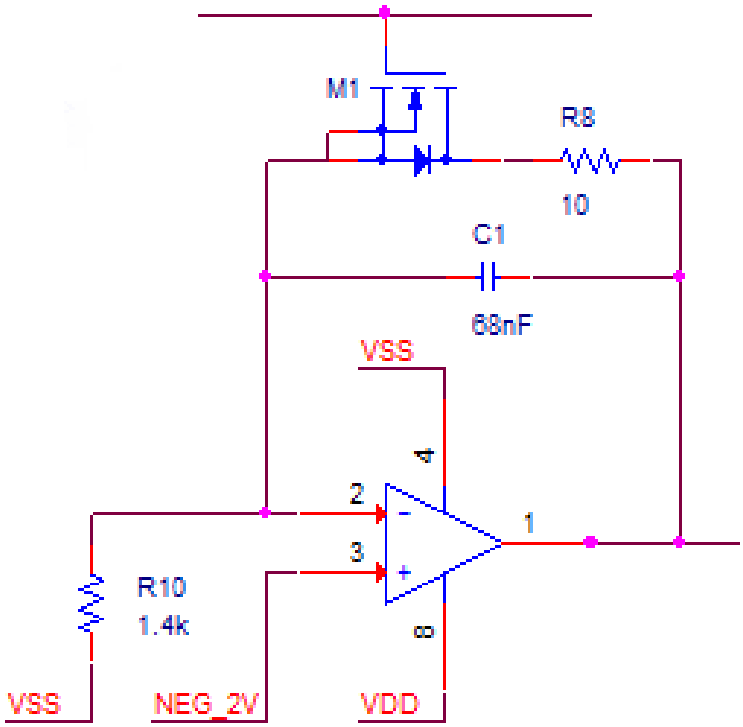

Figure 16 – Ramp generation sweep circuit based upon op-amp integrator.

In the case of Figure 16, V_i is equal to -2.5V (i.e. VSS). The MOSFET, M1, is provided such that the integrating capacitor can be held shorted until the conversion needs to start. Therefore, the gate of M1 is intended to be connected to an active low Start signal. R8 is utilized, in addition to the NMOS's on resistance, simply to mitigate an in-rush of current upon a reset of C1. Therefore, VC(0) = 0 since the MOSFET shorts the capacitor until a Start occurs. The non-inverting bias of -2V sets the initial ramp voltage to -2V. As formerly described, since the dynamic range of the instrumentation amplifier constrains operation of the output to around Vxx±1.4V, then utilizing a gain of 100 for a

20 mV sensor requires offsetting the instrumentation amplifier's output to -1V. Therefore the ramp needs to start at most at -1V. In order to allow a buffer for any transients resulting from the gated capacitor, and to facilitate an additional sensor settling delay, a ramp starting voltage of -2V was chosen. The initial 1V buffer zone also allows a bias for the output oscillator pulse width such that there is a minimum period aside from any modulation. Therefore, even for a zero pressure output, there will still be an output signal accordingly. Further, the -2V reference sets the ramp to begin outside of the VSS rail (i.e. > -2.5V), which negates non-linear saturation related delays. Hence, once an active low Start signal occurs, the MOSFET will turn off and a ramp will begin at -2V rising until saturation of the operational amplifier at VDD, or +2.5V. The delay from -2V to the sensor positive pressure zone beginning at -1V is 190 μsec. This delay facilitates obtaining the necessary 1.14 msec minimum described earlier that is needed for the sensor signal to settle. Since the startup delay circuit provides 1 msec, the -2V to -1V delay adds another 0.190 msec thereby exceeding the minimum 1.14 msec requirement by 50 μsec, allowing a startup delay buffer.

The input signal in the case of Figure 16 is the difference between the non-inverting input and the inverting input of the amplifier. With VSS at -2.5V and the non-inverting reference set at -2V, V_i results in -0.5V. Therefore the transfer function is:

$$v_o(t) = -Vin\frac{t}{RC} - V(0)$$

$$v_o(t) = 0.5\frac{t}{95.25\cdot 10^{-6}} - 2$$

Figure 17 shows a graph of the transfer function illustrating the range of temporal encoding for the analog pressure signal output. The range from -1V to 1V spans 381 μsec, yielding a gain of 500 nsec per millimeter of water (or 2.62 mV) over the full dynamic range of 762 mm H_2O. The circuit of Figure 16 was designed based upon the desired transfer function, whereby an arbitrary, but relatively small standard value of capacitance was chosen of 68 nF, such as to minimize in-rush current for a reset of the capacitor. Substituting the selected 68 nF capacitance into the integrating equation provided a desired resistance of 1.4 kΩ.

The in-rush current upon resetting the capacitor is described by:

$$i(t) = C\frac{dv}{dt}$$

And therefore, the faster the discharge, the larger the dissipating current. Adding a series resistance into the circuit of the MOSFET and capacitor results in a simple parallel RC discharge by a countercurrent, which can be modeled based upon a derivation from Kirchhoff's voltage law, in that the sum of the voltages around the RC loop, must equal zero. Therefore, the transient current of shorting the integrating capacitor with an initial voltage can be described by:

$$v_R(t) + v_C(t) - V_C(0) = 0$$

$$i(t)\cdot R + \frac{1}{C}\int_0^t i(t)\,dt - V_C(0) = 0$$

and now multiplying by C and differentiating both sides,

$$RC\frac{di(t)}{dt} + i(t) = 0$$

The solution to the differential equation becomes:

$$i(t) = \frac{V_C(0)}{R}e^{\frac{-t}{RC}}$$

Where $V_C(0)/R$ is the initial current resulting from the charged capacitor. For a capacitor voltage of 2.5V-(-2.0V), then a 4.5V discharge into a ten ohm dissipating resistor, would equate to a peak current of 450 mA. The on resistance of a MOSFET would only decrease the peak current. Given the small current allowed by a ten ohm resistor, a search was conducted for a compatible MOSFET to allow gating of the integrator. The Fairchild FDN327N was identified and selected since it can withstand a continuous 2 A of current with peaks up to 8 A. Its maximum drain to source voltage, V_{DSS} can withstand 20 V, and can support a gate to source voltage of ±8 V. The MOSFET has a low V_{GS} of 0.7 V typically and its $R_{DS(ON)}$ is within the milli-ohms range, which is inconsequential to the circuit.

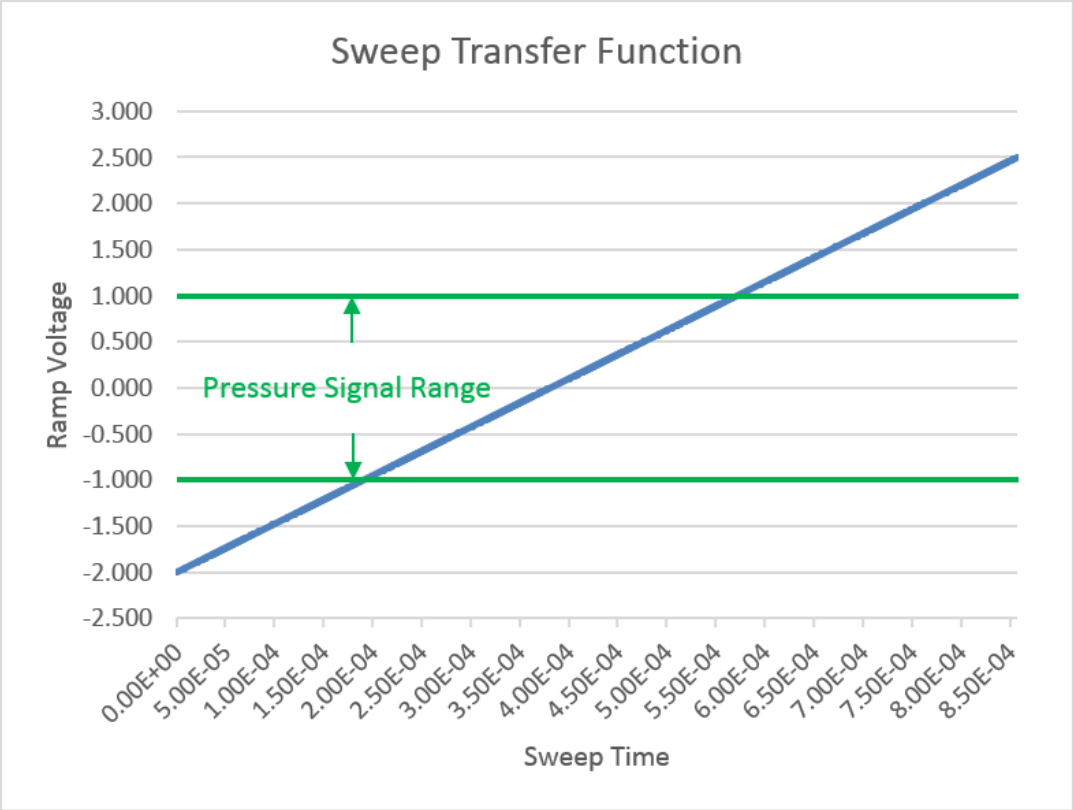

Figure 17 – Sweep transfer function for 500 nsec per mm H2O over 2 V signal span.

A search for a low power operational amplifier for the sweep circuit was undertaken. Again Texas Instruments, with its numerous acquisitions and operating units was examined first. Figure 18 shows a narrowed selection of low power operational amplifiers provided by TI. Similar to the instrumentation amplifier criteria, the OPA-2170 was selected based upon its low operating power supplies compatible with the design intentions, high common mode rejection ratio (CMRR), and very low input bias currents and offset voltage, which typically is only a quarter of a millivolt, but can be as high as 1.8 mV.

Compare Parts	OPA2170	TLC2262	TLV2432
Status	ACTIVE	ACTIVE	ACTIVE
Number of Channels	2	2	2
Total Supply Voltage (Min) (+5V=5, +/-5V=10)	2.7	4.4	2.7
Total Supply Voltage (Max) (+5V=5, +/-5V=10)	36	16	10
Iq per channel (Max) (mA)	0.145	0.25	0.125
GBW (Typ) (MHz)	1.2	0.71	0.5
Slew Rate (Typ) (V/us)	0.5	0.55	0.25
Vn at 1kHz (Typ) (nV/rtHz)	19	12	18
CMRR (Min) (dB)	104	70	70
IIB (Max) (pA)	15	100	60
Rail-Rail	Out	Out	Out
Rating	Catalog	Catalog	Catalog
Operating Temperature Range (C)	-40 to 125	-40 to 125 0 to 70	-40 to 125 -40 to 85 0 to 70
Pin/Package	8SOIC 8US8 8VSSOP	8SOIC 8PDIP 8TSSOP	8SOIC
Approx. Price (US$)	0.60 | 1ku	0.60 | 1ku	0.55 | 1ku

Figure 18 – Texas Instruments narrowed selection of low power operational amplifiers.

A SPICE model of the TI OPA-2170 was utilized within initial simulations of the integrator, in which convergence issues were encountered. Relaxing of the convergence conditions and increasing the number of iterations improved the simulations. However, there was a problem within the simulator PSPICE from Cadence whereby the model affected other parts of the netlist and wouldn't allow initial capacitance conditions to be set. After a long period of time with support from the distributor and manufacturer of the software, a different operational amplifier was ultimately chosen in order to ensure a proper simulation could be conducted prior to prototyping.

The Analog Devices ADA4692 was chosen among their offering of low power, low noise, operational amplifiers. The ADA4692 typically only consumes a low 180 μA quiescent with half pico-amp input bias currents and an offset voltage of about 500 μV, typically. A SPICE model of the device was obtained and simulated fine within the Cadence PSPICE environment.

The last block of the timing channel shown in Figure 9 is the comparator for ultimately transforming the ramp and sensor analog voltage into a time encoded representation. A low power comparator was sought to satisfy requirements for a split rail supply, low voltage operation, low jitter, low input bias and offsets, but primarily for low jitter. Evaluating TI's offering of comparators, the selection was quickly narrowed from 171 parts to only 15 once the low voltage and power criteria was applied and an offset voltage of typically ≤ 2 mV was selected. Out of the 15 parts, only a few families of comparators were available. The LM339A was selected upon the overall criteria and because it offers the fastest edge and lowest jitter when compared to the other remaining parts. The comparator offers a 300 nsec, low to high response, which is the dominant response time of the comparator, since it is an open collector output and the fall time is much faster with active sink current. While the offset voltage of 2 mV is higher than desired for an equivalent 2.6 mV/mm H_2O comparison, there were no other comparators with a lower offset voltage available that met the overall criteria.

In considering comparator timing errors, the inaccuracies result primarily from two sources of variations including propagation delay (i.e. time walk) and noise induced jitter

[41]. The time walk of a comparator stems from disparities in the amplitude of the input signal whereby the amount of underdrive or overdrive, relative to the comparator's threshold voltage, alters the propagation delay through the comparator. Figure 19 shows the time walk performance of the LM339A for various overdrive voltages. It has also been shown [42] that the input signal slope at the time of threshold crossing also affects the walk of the comparator and that both the amount of overdrive and signal slope influence the response time due to the necessary exchange of charge at the input device.

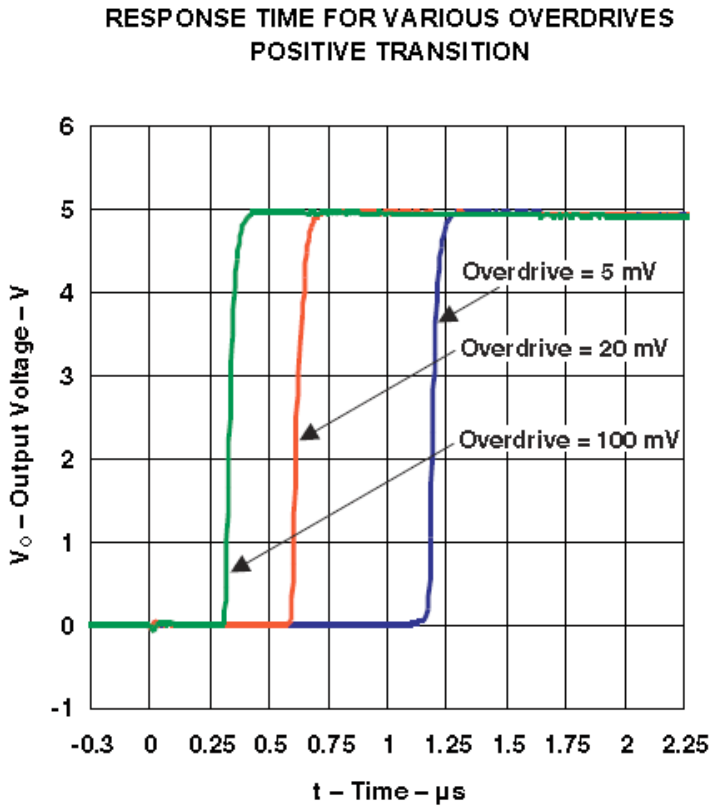

Figure 19 – LM339A comparator timing jitter for various levels of input overdrive.

Jitter induced errors produce repeated timing variations in the comparator output signal for identical input signals. This type of error originates from electronic noise within the comparator and produces uncertainty as to when the input threshold crossing took place. The uncertainty can be modeled, assuming a Gaussian probability density of noise amplitude, according to the triangular rule [43] as:

$$\sigma_T = \frac{\sigma_v}{\frac{\partial V(t)}{\partial t}\Big|_{t=T}}$$

where σ_v is the rms value of input signal noise of V(t) and σ_T is the resulting rms timing uncertainty induced in the output signal which represents the input threshold crossing occurring at time T.

As can be seen, overall timing uncertainty is minimized for low dynamic range input signals with fast rise times and for a minimum of noise present throughout the system. Producing high bandwidth fast edge timing signals capable of fast slew rates in the presence of parasitic capacitances requires ample bias current. The timing performance achieved comes at the expense of power consumption [44] and necessitates an optimization of performance requirements versus power constraints.

Fortunate for this application is that the sensor is within a stable pressure environment over the intended period of one sample, which allows for a relatively slow time encoding or, in other words, a high output timing gain (i.e. $\partial t_{out}/\partial v_{sensor}$). This convenience affords a relatively forgiving timing jitter in order to still meet the intended resolutions and power constraints of the transponder since the magnitude of the timing encoding is much

larger than that typically found in comparator jitter values. This is especially true in this application, since the input slope will always be the same from the ramp generator that extends to a maximum overdrive (i.e. VDD) against the stable (i.e. essentially D.C.) sensor input.

Power

A low voltage power supply was sought for the transponder in order to reduce telemetry coupling efficiency and voltages, as well as to reduce quiescent power conditions. Based upon examples within the literature review for telemetry, a design less than 250 mW was desired. Further, split rail supplies were anticipated in order to reference the sensor input to ground, thereby reducing any common mode errors upon the analog channel. Since the transponder is designed with the intent to be powered via inductive coupling, an effective center tapped transformer was assumed.

Since the sensor gain is a product of the supply voltages, it's important that the supply rails be stable. Therefore, active regulation was pursued in order to minimize measurement errors. Both positive and negative series regulators were surveyed for use within the design with the primarily intent of evaluating the circuit, rather than being a final solution for the implant. Since the aim of the transponder is to be less than 250 mW, this would only require approximately 100 mA from each regulator. Therefore, a search for a low dropout, low voltage and low quiescent power regulators was ensued. From Texas Instruments, the LM1086 was identified as providing a fixed +2.5V output, with a typical line regulation of 300 μV. The drop out voltage was specified at 1.3 V

normally, but up to 1.5 V maximum. The quiescent current was specified at 5 mA typical and 10 mA, maximum.

A negative series voltage regulator was searched, but no fixed -2.5V regulator was identified within the low dropout and power range sought. The Texas Instruments LM337 adjustable regulator was finally selected. The LM337 is specified for a line regulation of 0.01%/V typically. Therefore, for a 1 V input change, the output would change 250 μV. The maximum input voltage specified is -3 V. The quiescent current required is based upon the adjustment resistors, which are typically 120 Ω according to the data sheet. However, 250 Ω was selected in order to minimize the quiescent and still meet the specifications for minimum loading required for regulation. Therefore, the quiescent current was designed for 5V/500Ω or 10mA.

Since precise -1 V and -2 V references are needed to support the low voltage dual rail design, an operational amplifier reference was designed. The operational amplifier configuration was chosen, because the references do not require large currents and because of their very low output impedance. The TI INA-141 instrumentation amplifier specifies that for a resistance of only 8 Ω into the reference pin, the amplifier's common mode rejection degrades down to 80 dB. The operational amplifier ADA4692 offers an open loop gain of 90 dB, minimum, and 100 dB, typically. With this large of an open loop gain, the low gains needed for a reference at D.C. would result in a negligible output impedance by virtue of a very large loop gain. Figure 20 shows the design of a dual inverting operational amplifier, whereby a standard bandgap reference of 1.225V,

supplied by the LM4051, is utilized along with the gain of each inverting amp, $-R_f/R_{in}$, to provide the desired -1 V and -2 V references. The pull-up resistor of the reference maintains a quiescent current while also supporting the current into each of the operational amplifiers (e.g. ~1 mA each).

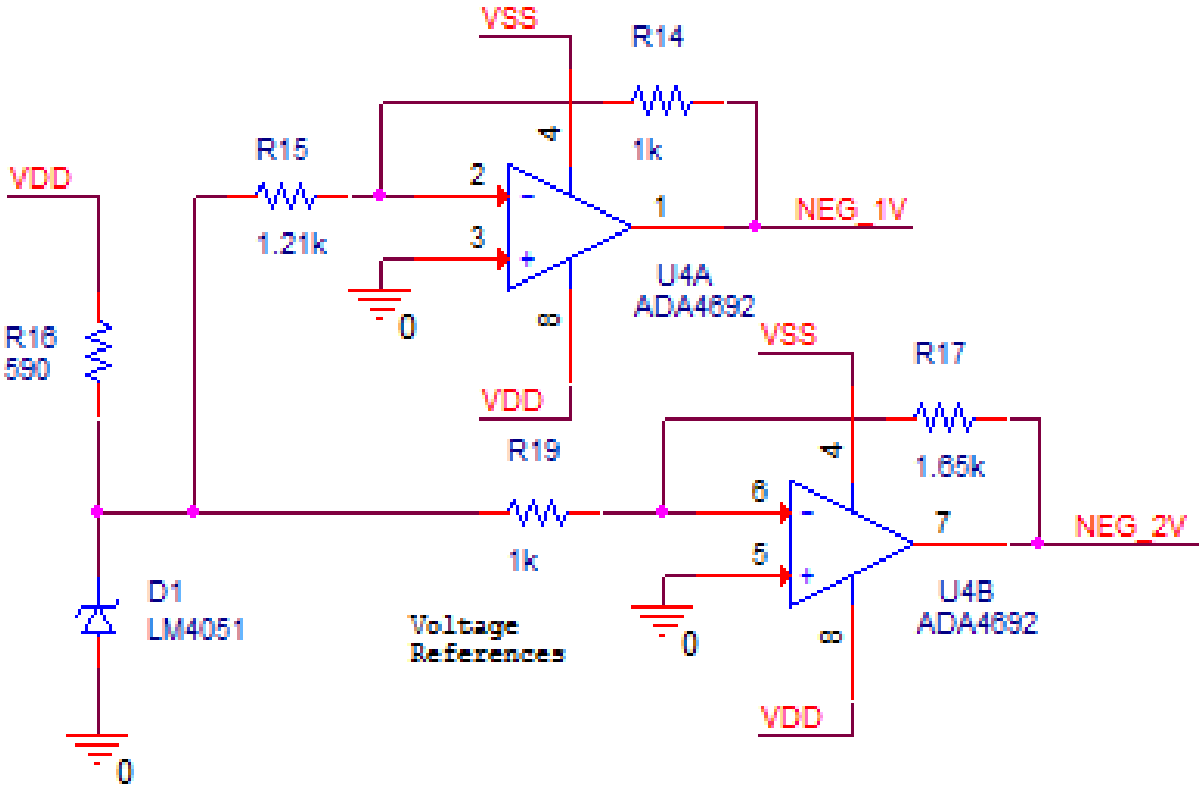

Figure 20 – Reference voltages necessary for analog and timing channels.

Methods

Circuit Overview

Figure 21 shows the overall circuit diagram of the approach described in the former sections. The pressure sensor was modeled as described in the Approach with a bridge configuration. For simulations, a 76 nF capacitor was placed differentially to the sensor outputs, to model the settling time of the sensor, as derived from within the Approach section. The bottom of the schematic shows the power regulation and references generated to support the analog and timing channels. To the right of the schematic are the output nets labeled /START and STOP, where the Start signal is active low. The ideal transfer function for the transponder circuit is given in Figure 22, which shows a timing bias for zero pressure of 191 μsec as described within the Approach for the -2 V initial ramp until the -1 V sensor signal begins comparison. Therefore, the transponder will always respond with a Start and Stop signal, even for zero pressure readout values.

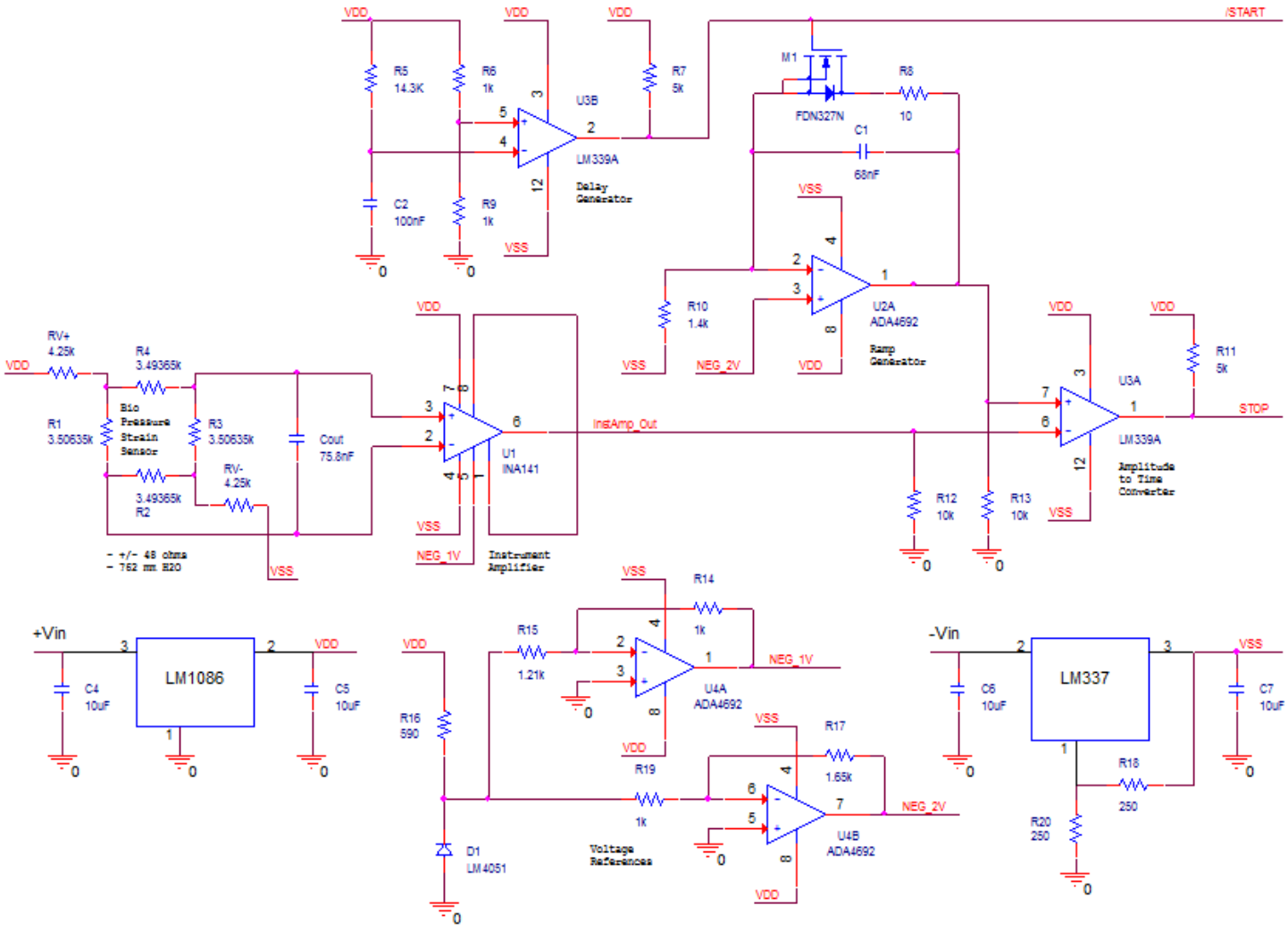

Figure 21 – Overall circuit diagram of transponder timing readout electronics.

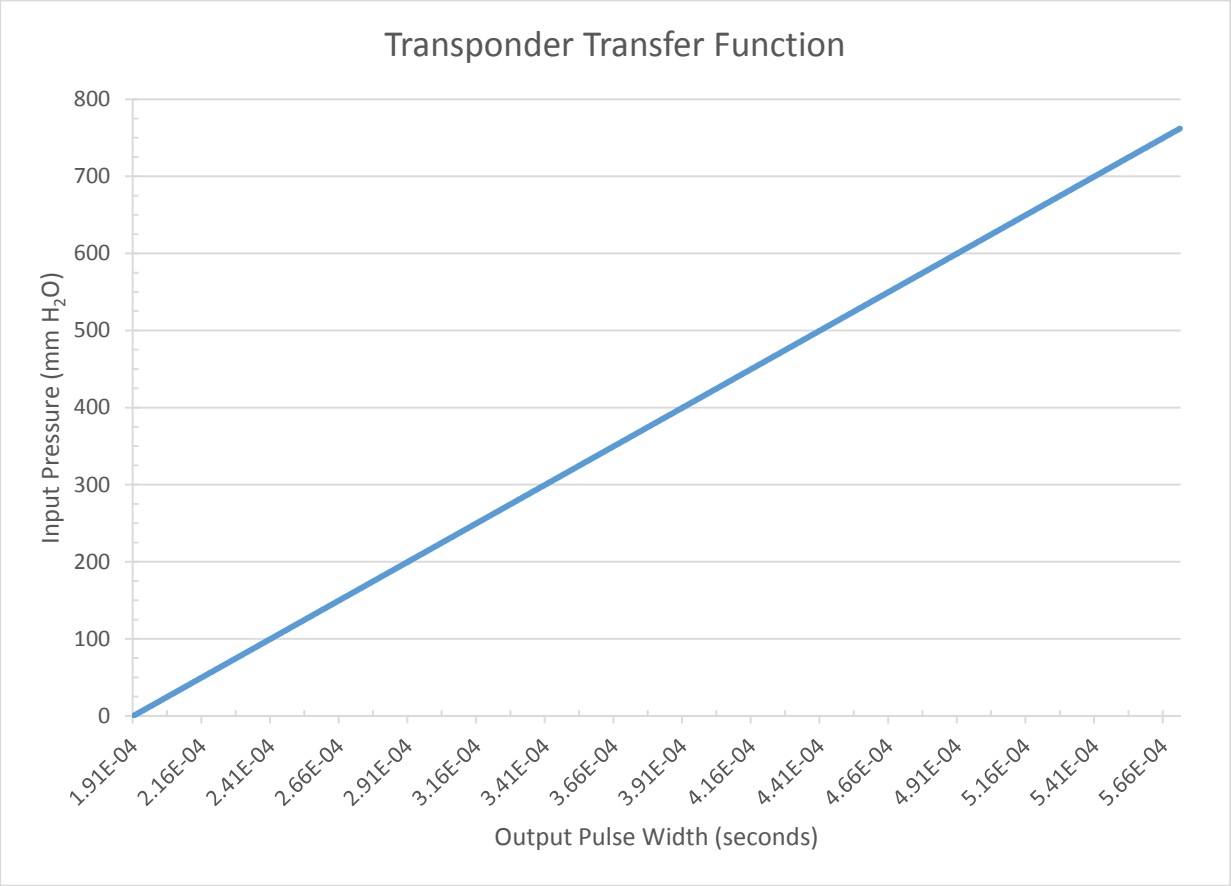

Figure 22 - Transponder transfer function.

Error and Noise Analysis

For the transponder, there are three primary types of errors introduced by its components. One is the offset errors that are present upon manufacturing. These errors arise from imperfections of resistor matching in the sensor, operational amplifier offsets, resistor tolerancing affecting the reference voltages, comparator offset voltages, ramp circuit component tolerancing and so on. These types of errors, which are not

expected to shift over time, can be compensated for by adjusting the gain of the ramp circuit and/or references, or calibrated otherwise. Alternatively, the sum of the measured errors can be recorded and corrected by the method of readout. Either case is straight forward and can occur at the time of manufacture.

The second type of error that occurs within the transponder is drift, which occurs over time. This type of error must be minimized by design since there are no non-invasive means of pressure calibration available. This type of error is of primary concern in the sensor itself, since drift of the electronics typically only occur over temperature. Given the final transponder design will be human implantable, a stable temperature very close to 37°C can be safely assumed due to thermoregulation. Therefore, in this design, drift of the sensor itself is of primary concern and is more related to the diaphragm plasticity and structural creep. Thirdly, the transponder itself generates errors due to thermal and electronic device noise. These noises directly affect the integrity of the measurement output and must be considered. In this design, thermal noise, shot noise, flicker noise, and avalanche noise are assumed, not including coupling noise effects, which may be mitigated by a later design incorporating shielding and other countermeasures. Analyzing the schematic of Figure 21 section by section provides the noise sources provided within Table 2 and Table 3. R5 through R9 and U3B are not within the signal chain since they only serve to delay start of a conversion.

Table 2 outlines the noise contributions of the resistive components within the circuit. These contributions are primarily thermal noise sources since metal film resistors were employed and result in a white power spectral density. The bandwidths utilized within

both charts are based upon the bandwidths available to the noise source into the signal chain. For example, in the case of the instrumentation amplifier, the specified 3 dB bandwidth at a gain of 100 is given at 200 kHz. Assuming a single time constant transfer function, the equivalent noise bandwidth is a factor of 1.57. Table 3 lists the active noise sources, whereby the instrumentation amplifier's noise and gain dominates the signal chain. A distant second active noise source are the regulators followed by the reference operational amplifiers. The reference amplifiers could be low pass filtered to alleviate a large part of their noise contribution, but due to the prototype construction and lack of significance within the chain, they were left unfiltered during testing, as was the instrumentation amplifier.

Table 2 – Noise contributions of signal chain passive components.

Source	Value	Conditions	Dominant Type(s)	Source	Noise BW	Noise e_n (rms)
R1	3,500	37°C	Thermal	$(kTR\Delta f)^{0.5}$	314 kHz	2.2 µV
R2	3,500	37°C	Thermal	$(kTR\Delta f)^{0.5}$	314 kHz	2.2 µV
R3	3,500	37°C	Thermal	$(kTR\Delta f)^{0.5}$	314 kHz	2.2 µV
R4	3,500	37°C	Thermal	$(kTR\Delta f)^{0.5}$	314 kHz	2.2 µV
RV+	4,250	37°C	Thermal	$(kTR\Delta f)^{0.5}$	314 kHz	2.4 µV
RV-	4,250	37°C	Thermal	$(kTR\Delta f)^{0.5}$	314 kHz	2.4 µV
R10	1,400	Metal Film, 37°C	Thermal	$(kTR\Delta f)^{0.5}$	2.6 kHz	0.1 µV
R11	5,000	Metal Film, 37°C	Thermal	$(kTR\Delta f)^{0.5}$	100 kHz	1.5 µV
R12	10,000	Metal Film, 37°C	Thermal	$(kTR\Delta f)^{0.5}$	100 kHz	2.1 µV
R13	10,000	Metal Film, 37°C	Thermal	$(kTR\Delta f)^{0.5}$	100 kHz	2.1 µV
R14	1,000	Metal Film, 37°C	Thermal	$(kTR\Delta f)^{0.5}$	5.65 MHz	4.9 µV
R15	1,210	Metal Film, 37°C	Thermal	$(kTR\Delta f)^{0.5}$	5.65 MHz	5.4 µV
R16	590	Metal Film, 37°C	Thermal	$(kTR\Delta f)^{0.5}$	1 MHz	1.6 µV
R17	1,650	Metal Film, 37°C	Thermal	$(kTR\Delta f)^{0.5}$	5.65 MHz	6.3 µV
R18	250	Metal Film, 37°C	Thermal	$(kTR\Delta f)^{0.5}$	10 kHz	0.1 µV
R19	1,000	Metal Film, 37°C	Thermal	$(kTR\Delta f)^{0.5}$	5.65 MHz	4.9 µV
R20	250	Metal Film, 37°C	Thermal	$(kTR\Delta f)^{0.5}$	10 kHz	0.1 µV

Table 3 – Noise contributions of signal chain active components.

Source	Conditions	Dominant Type(s)	Figure, RTI	Noise BW	Output Noise e_n (rms)
U1	AV=100	Thermal, Shot, Flicker	$8nV*Hz^{-0.5}$	314 kHz	448 µV
U2		Thermal, Shot, Flicker	$13nV*Hz^{-0.5}$	2.6 kHz	0.7 µV
U3A		Thermal, Shot, Flicker	N/A	N/A	N/A
U4A		Thermal, Shot, Flicker	$13nV*Hz^{-0.5}$	5.65 MHz	31 µV
U4B		Thermal, Shot, Flicker	$13nV*Hz^{-0.5}$	5.65 MHz	31 µV
D1	100 µA	Shot, Avalanche	N/A	10 kHz	20 µV
LM337	-2.5V	Thermal, Shot, Flicker	0.003%Vout	10 kHz	75 µV
LM1086	+2.5V	Thermal, Shot, Flicker	0.003%Vout	10 kHz	75 µV

For hand calculations, a course estimate of the output noise can be derived by summing the equivalent input noise contributors in variance to the instrumentation amplifier as a product of the gain and then comparing this to the ramp circuit's equivalent output noise. Given the sensor's output impedance is resistive and equivalent to 3kΩ, the resulting thermal noise is 2.0 µVrms. The amplifiers noise, referred to the input is 4.5 µVrms. The regulator noise also contributes to the input noise and is specified as 0.003% per volt of output over 10 kHz. Deducing this figure for 2.5V into an equivalent noise figure results in e_n=750 $nV \cdot Hz^{-1/2}$. Now, given the sensor bandwidth is very low and modeled with a 12kΩ input resistance with a 76 nF capacitance, the resulting single pole noise bandwidth equates to only 274 Hz. The integrated noise over 274 Hz from

the regulator then becomes 12.4 μVrms. Summing the noise sources in variance and taking the square root yields an equivalent input noise of 18 μVrms, as shown below:

$$e_n = \sqrt{(2.0{\cdot}10^{-6})^2 + (4.5{\cdot}10^{-6})^2 + (12.4{\cdot}10^{-6})^2 + (12.4{\cdot}10^{-6})^2}$$

$$= 18.2\ \mu Vrms\ input\ noise$$

This input noise is dominated by the regulator noise, which exists upon the input as a common mode, but uncorrelated. The CMRR of the instrumentation amplifier may reduce this figure and the above expression estimates a worst case hand calculation. The input current noise sources will present as common mode noise given symmetry of the input sensor and will be attenuated at a specified CMRR of 125 dB. Now, applying the gain of 100 to the equivalent input noise of the instrumentation amplifier results in a noise estimation of about 1.8 mVrms, which will be presented to the non-inverting input of the comparator.

From the ramp circuit, the very low frequency filtering of the integrator results in an almost negligible amount of noise amounting to roughly 1 μV. For the purpose of this dominant noise estimation, this source will be ignored since its negligible compared to the analog channel's noise. However, another source of noise in the ramp circuit arises from the turn-off time of the MOSFET, since any variable delay within the integrator will result in a jitter noise on the output. The datasheet specification gives a worst case turn-off time of only 29 nsec, which in some circuits could be very significant. However, in the case of 1 mm H_2O being 500 nsec, this source will also be ignored for the rough noise estimation.

Therefore, an overall hand estimation from the dominant sources of noise within the circuit arises from the 1.8 mVrms noise from the analog channel. The power supply noise and regulation are assumed small as compared with the analog channel's output since the instrumentation amplifier is specified at over 100 dB of rejection ratio (PSRR) and the operational amplifiers are specified at 80 dB minimum. Although the sensor itself is very susceptible to power supply variations, in this application the transponder is intended for inductive power coupling into a center tapped transformer. Therefore, any fluctuations in voltage coupling would be prevalent upon both legs of the transformer and also common mode to the split rail sensor configuration. Therefore, the dual supply bridge circuit configuration can provide an optimal interface against common mode noises [35].

The noise or jitter of the comparator wasn't specified within the datasheet from the manufacturer, but was discussed within the Approach's Timing Channel Electronics analysis. Assuming the comparator as ideal, the 530 μV of noise can be multiplied by the timing gain of the circuit to result in an overall hand estimation of output noise. The timing gain of the transponder is 500 nsec per mm H_2O or 2.62 mV. 1.8 mVrms of input noise to the comparator results in an output jitter of 343 nsec rms or 0.69 mm H_2O. Simulations will be performed to gain a better prediction of actual output performance and will be compared to the hand estimations.

Simulations

Circuit simulations of the transponder were performed with Cadence PSPICE 16.6. A SPICE model for the instrumentation amplifier was unavailable from TI, but a very

similar part from the same family, primarily different only in temperature range, was selected as a substitute for simulations. Instead of the INA-141, the INA-129 was utilized in simulations. Figure 23 shows the comparison of the parts illustrating only a CMRR difference and slight bias current delta. Primarily, the difference was in temperature range, as the INA-129 is a military grade part.

Compare Parts	INA129	INA141
Status	ACTIVE	ACTIVE
Vs (Min) (V)	4.5	4.5
Vs (Max) (V)	36	36
Input Bias Current (+/-) (Max) (nA)	5	5
Input Offset Drift (+/-) (Max) (uV/Degrees Celsius)	0.5	0.5
Noise at 1kHz (Typ) (nV/rt(Hz))	8	8
CMRR (Min) (dB)	120	117
Non-Linearity (+/-) (Max) (%)	0.002	0.002
Bandwidth at G=100 (Min) (kHz)	200	200
Iq (Typ) (mA)	0.7	0.75

Figure 23 – Texas Instruments INA-129 to INA-141 comparison.

PSPICE models of the regulators were unavailable and these were modeled with DC voltage sources within PSPICE. Figure 24 shows an overall conversion process simulated within PSPICE illustrating the active low /Start signal and active high Stop occurring at the crossover point of the ramp signal and the sensor's amplified output (-749 mV).

Figure 25 shows the simulation of the sensor signal at the output of the instrumentation amplifier for an approximate 100 mm H_2O. The simulation replicates the specifications for a 500 μsec 10%-90% rise time with an equivalent 76 nF capacitance and shows an almost completely settled signal by 1 msec (approximately five time constants).

In order for the transponder to allow the sensor signal to settle to less than 1%, 1.14 msec is necessary. The delay circuit is designed to provide a 1 msec delay, which when combined with the first volt of the ramp, equates to an approximate 1.19 msec. Figure 26 shows the PSPICE simulation for the startup delay circuit with a resulting 0.994 msec delay. The difference in 6 μsec arises from the choice of a standard 1% value resistor 14.3 kΩ versus the calculated 14.4 kΩ.

Figure 27 shows the simulation of the ramp circuit beginning at -2.016 and rising linearly thereafter. Figure 28 compares the simulation to an ideal transfer function of the integrator. As can be seen from the figure, there is a negative gain error in the simulated results, which calculates to -4%. Also, there is an offset beginning at -2.016V. The offset is due to the -2V reference simulating to -2.020, which is tied to the non-inverting input of the integrator. Further, the operational amplifier simulated with a resulting 1 mV input offset, setting the inverting input to -2.019V. Finally, the MOSFET and 10Ω resistor resulted in 3.5mV IR drop, thereby placing the output voltage at -2.016V. The gain error again arises from the -2.020 reference error, and operational amplifier 1 mV offset, which resulted in the integrating resistor's voltage being 0.481V,

as shown in Figure 29, versus the ideal 0.500V. As the following equation shows, the integrator input voltage directly affects the gain of the circuit:

$$v_o(t) = -Vin\frac{t}{RC} - V(0)$$

and the 0.481/0.500 results in a -3.8% error. The remainder of the difference between the -3.8% and the simulated -4.0% is in a simulated 1.3 μA leakage current through the MOSFET.

Figure 30 shows the simulation outputs for the reference and the derived voltage references of -1V and -2V. The LM4051 simulates at a specified 1.225V. The derived references simulate at -1.0114V and -2.0197V. The errors arise from the limitation of standard value resistor choices and about a half millivolt offset on the operational amplifiers. A correction for these resistors could be implemented with the use of smaller resistor values and series potentiometers for use in the feedback path.

Figure 31 shows the simulated output noise at the instrumentation amplifier. Note the power supply sources used during the simulation were ideal since the regulator manufacturers didn't offer models. Never the less, even without the regulator models, the PSPICE simulation underestimates the noise compared to the former hand analysis. The simulation only shows about 0.8 μVrms of output noise compared to the 1.8 mVrms hand calculated, which was dominated by regulator noise. The PSPICE noise simulation for the ramp output resulted in less than only a microvolt and is in agreement with that predicted by the hand analysis.

Figure 32 shows the PSPICE simulation output for 0 to 20 mV sensor inputs in steps of 2 mV. Figure 33 compares the simulated results to that of the ideal transfer function. The negative gain ramp earlier examined (-4.0%) resulted in a positive gain error (3.5%) at the output. This is intuitive since a slower ramp signal would result in a longer time conversion from Start to Stop by the output comparator. The delta between the 4.0% and 3.5% is actually gain error simulated in the instrumentation amplifier as shown in Figure 34 that amounts to approximately 0.5%.

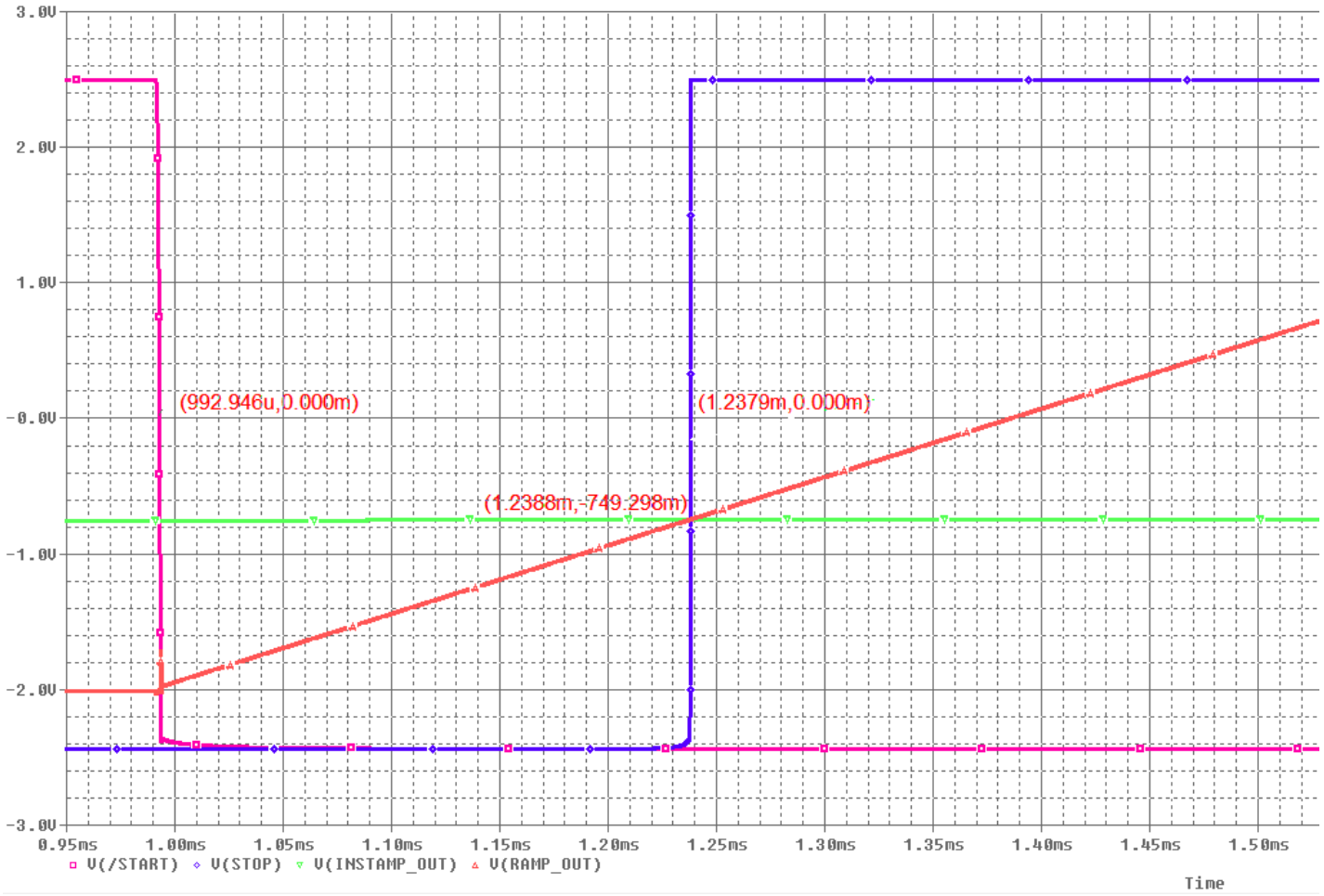

Figure 24 – Transponder simulation showing /Start (magenta), amplified sensor signal (green), ramp signal (red), and Stop (blue).

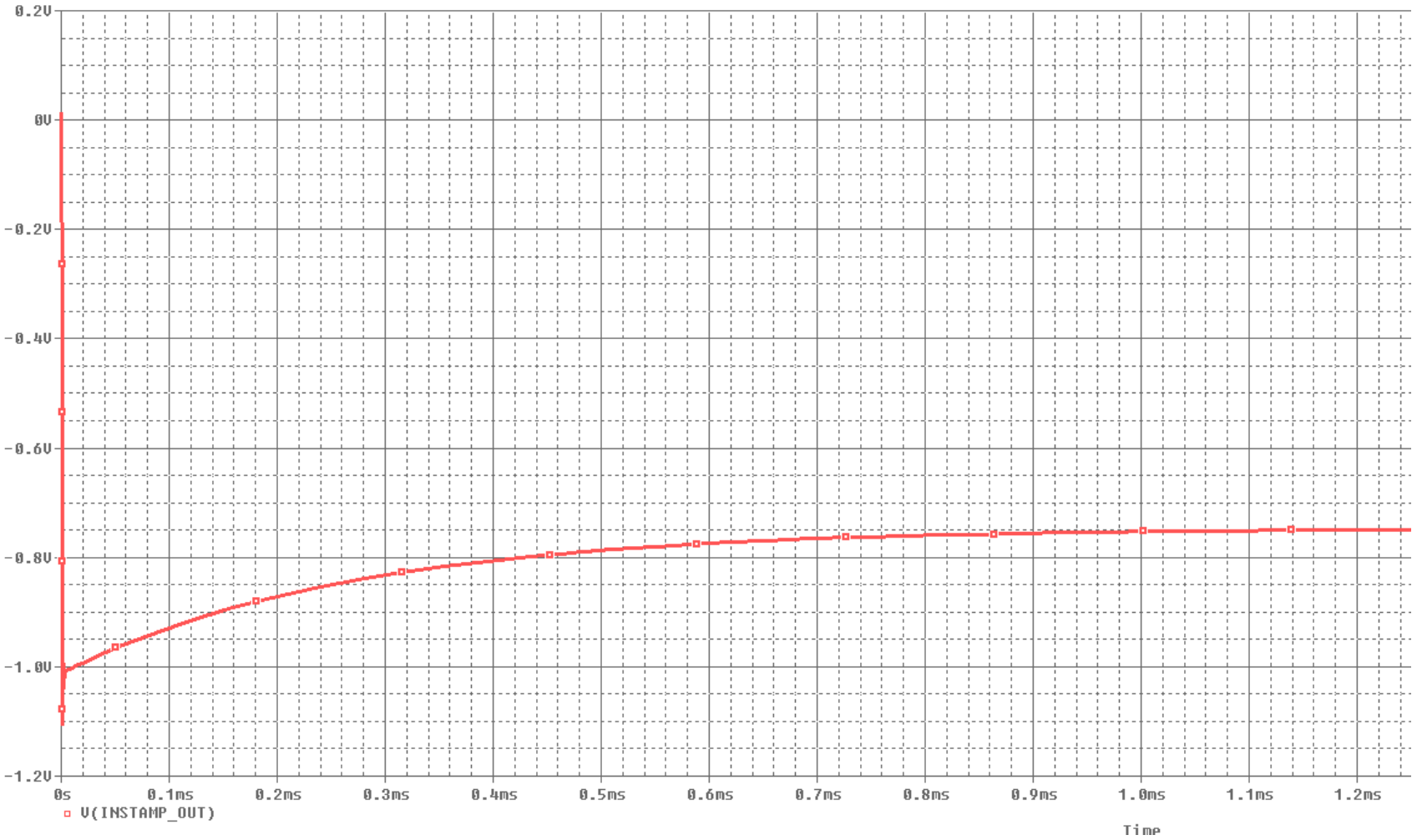

Figure 25 – Sensor output for approximate 100 mm H_2O.

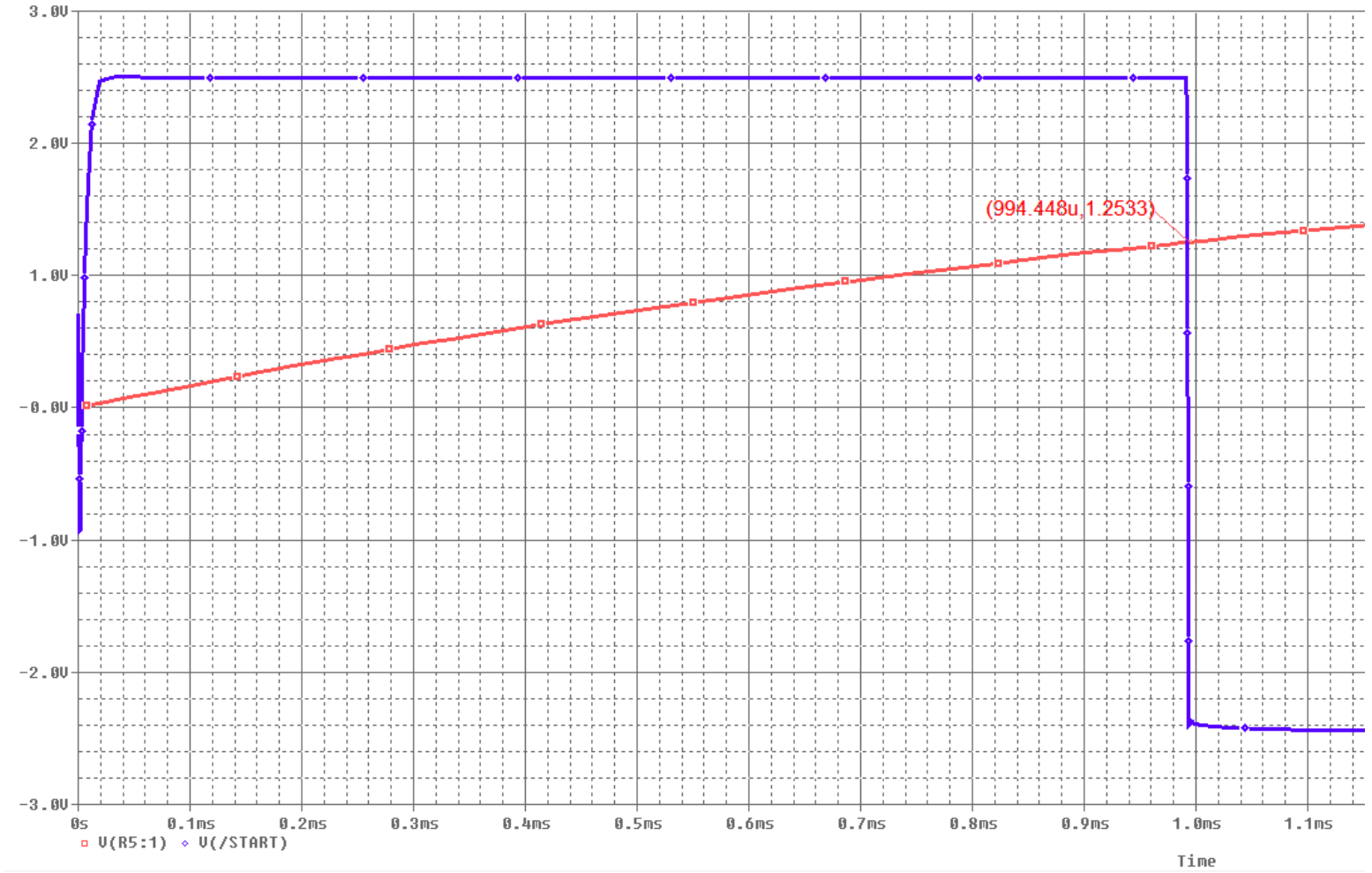

Figure 26 – Startup delay and trigger.

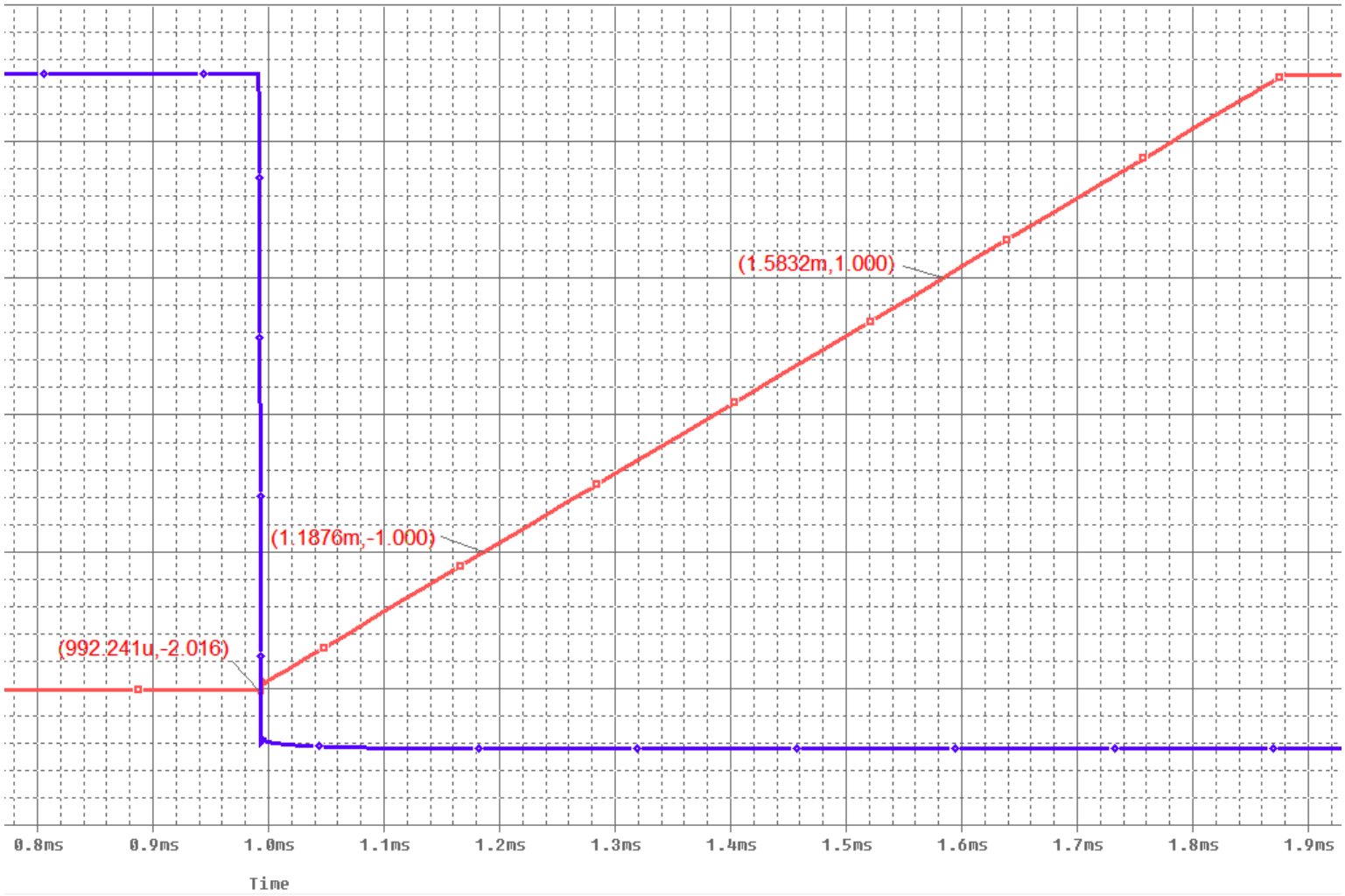

Figure 27 – Start and ramp output.

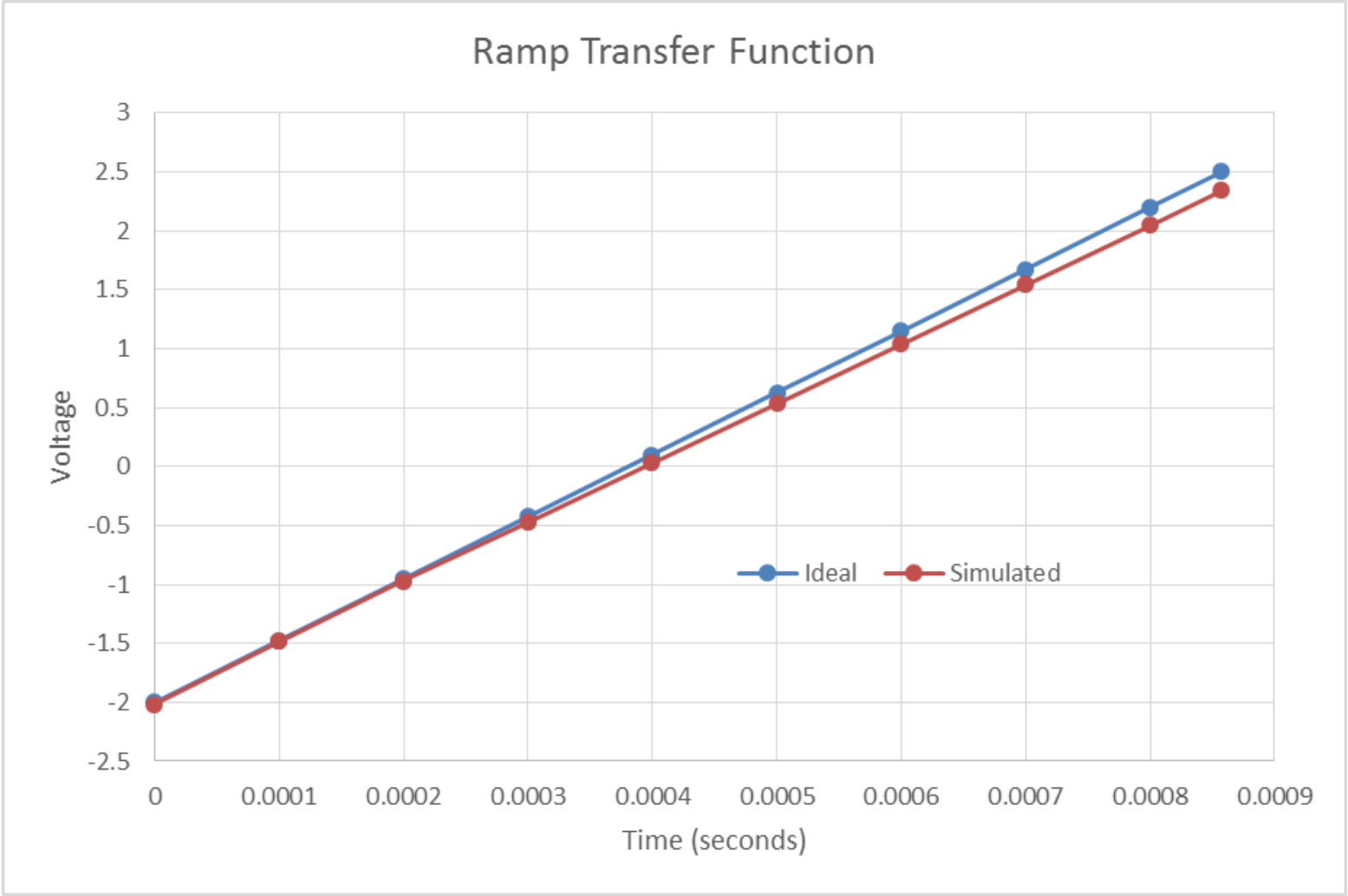

Figure 28 – Plot of ideal ramp output versus simulated output.

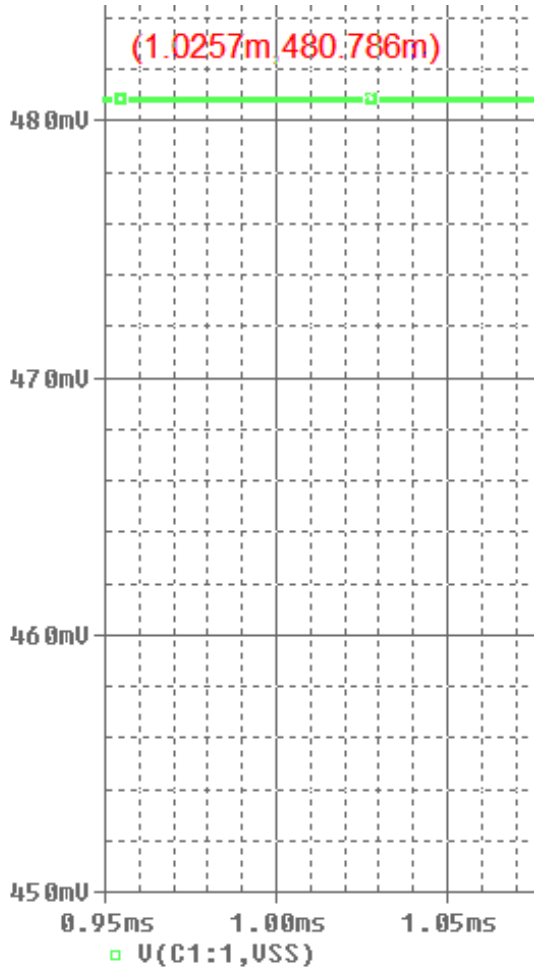

Figure 29 – Integrator input resistor differential voltage (0.481 V vs. ideal 0.500 V) resulting in a gain error.

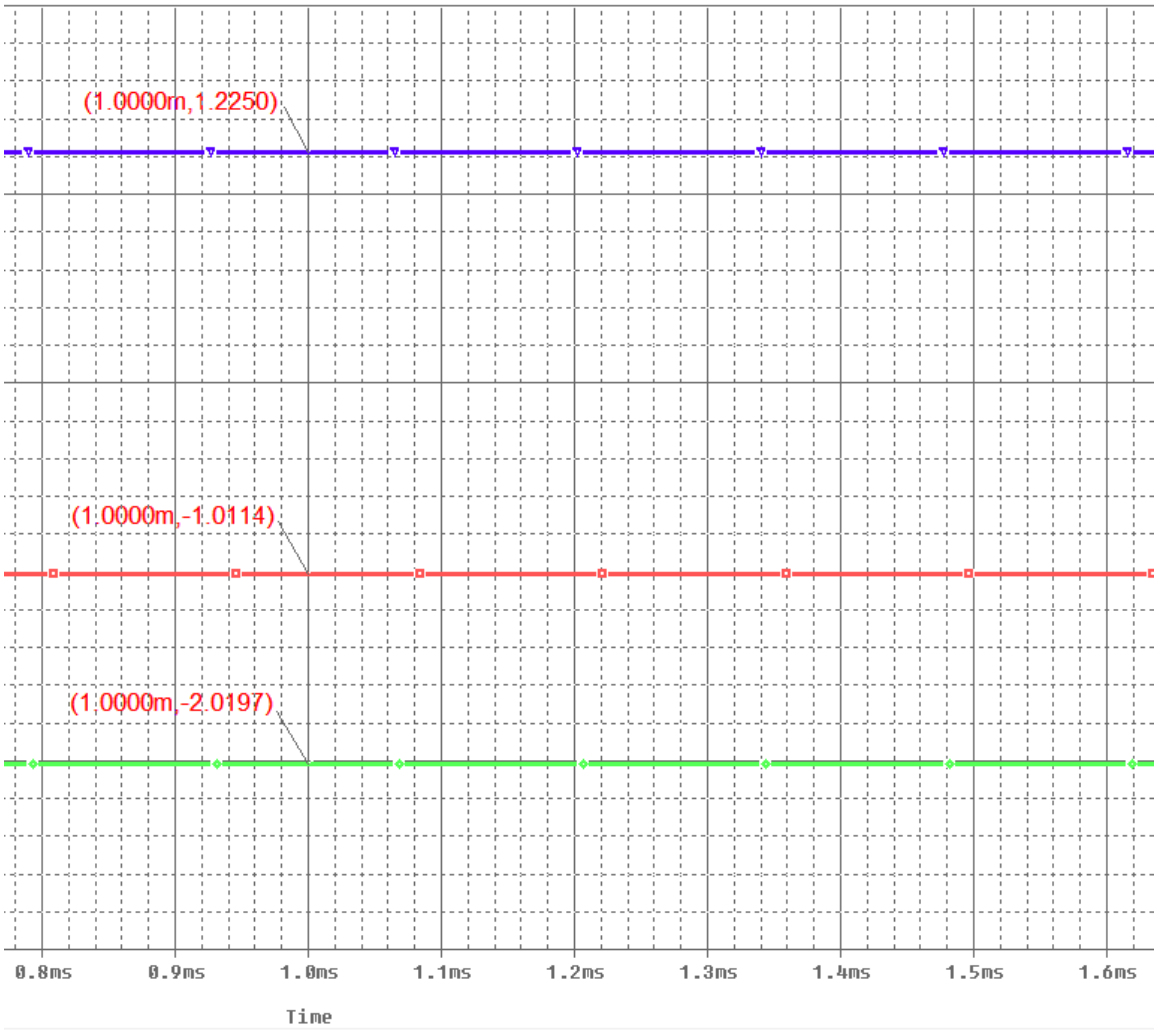

Figure 30 – Operational amplifier reference voltage and outputs.

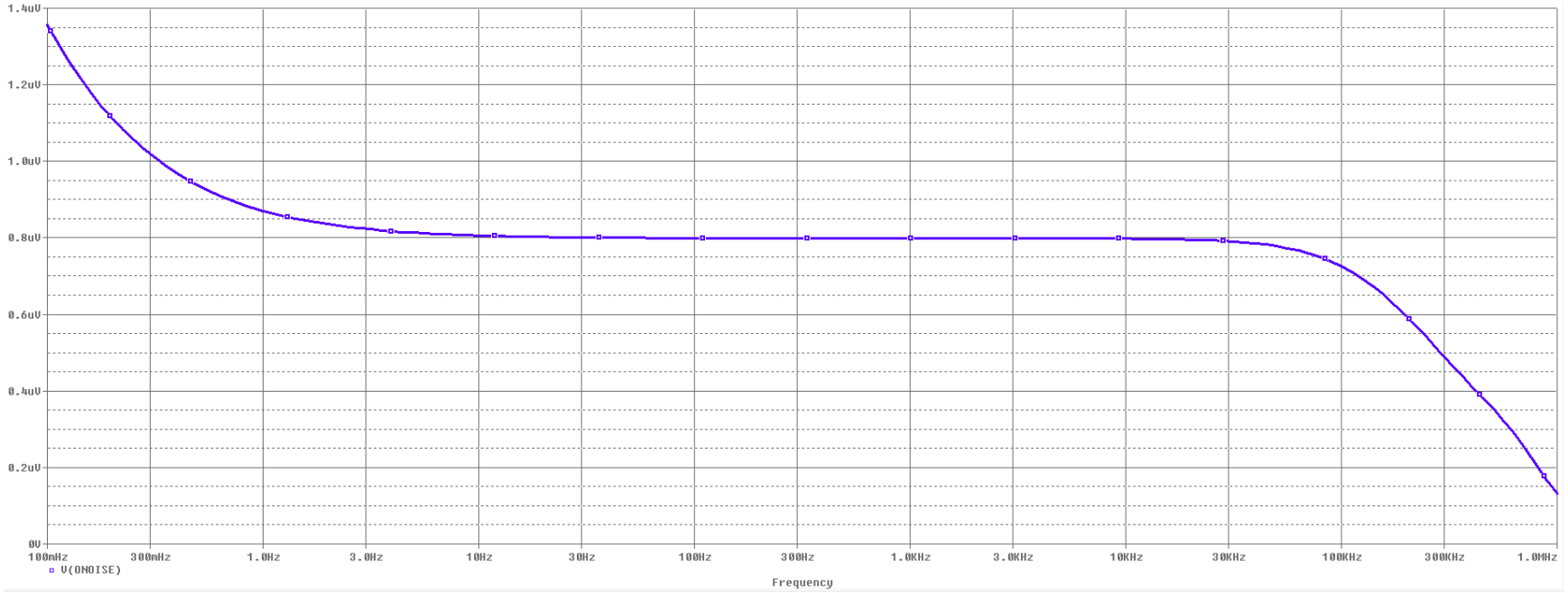

Figure 31 – RMS summed output noise for instrumentation amplifier (w/t ideal power supplies).

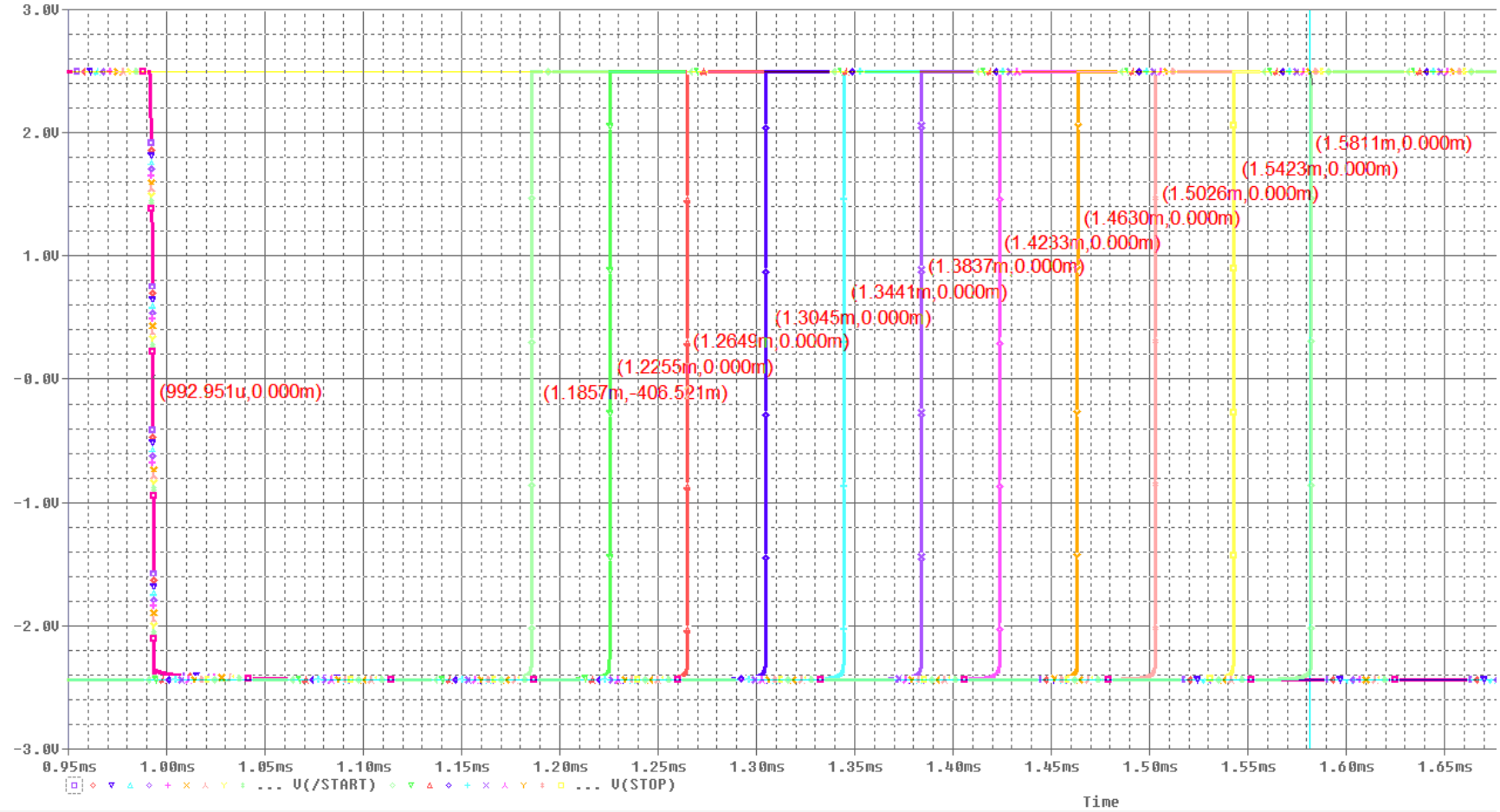

Figure 32 – /Start and Stop output signals for the full range of sensor input (20 mV).

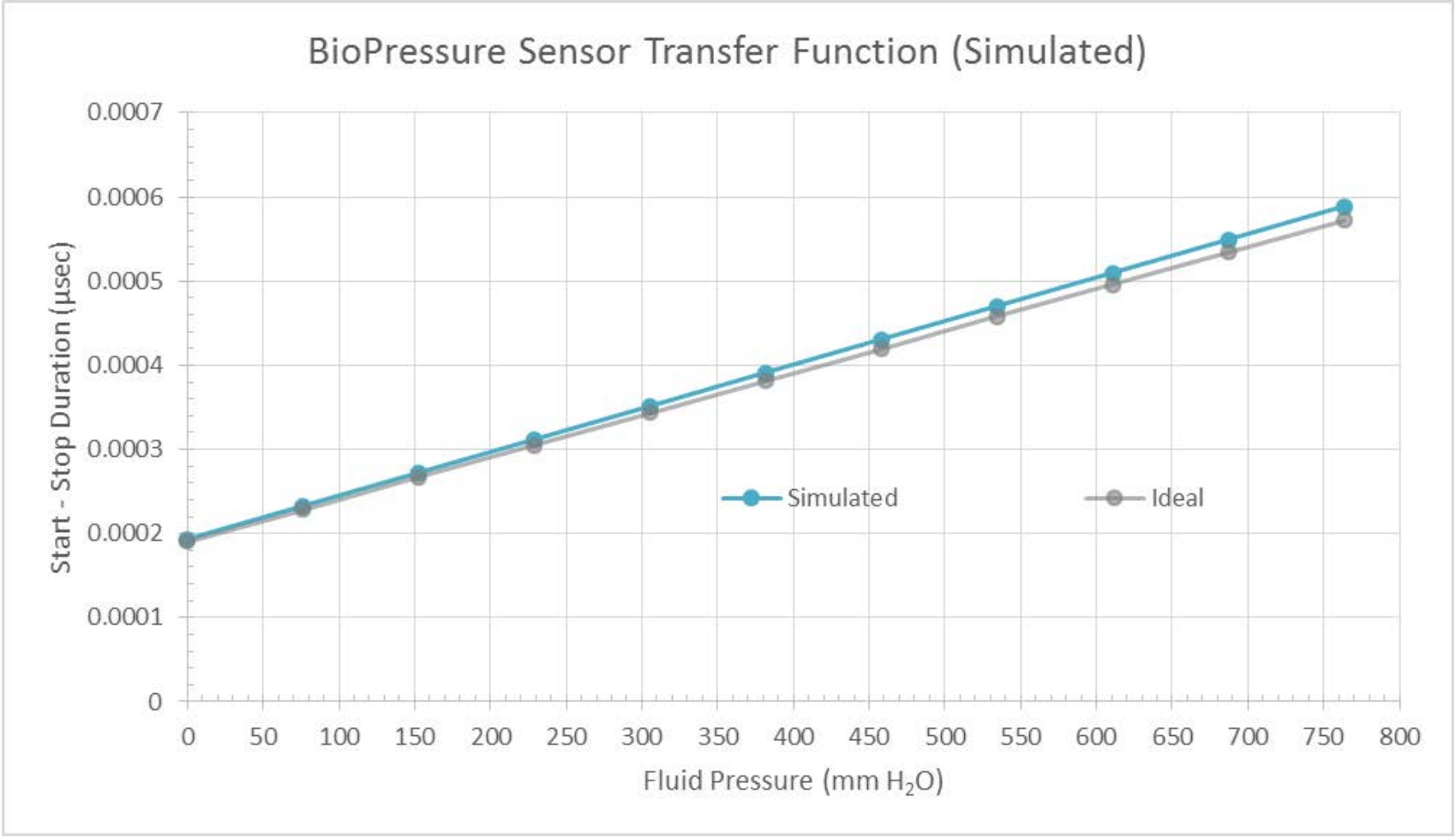

Figure 33 – Simulated versus ideal transponder transfer function.

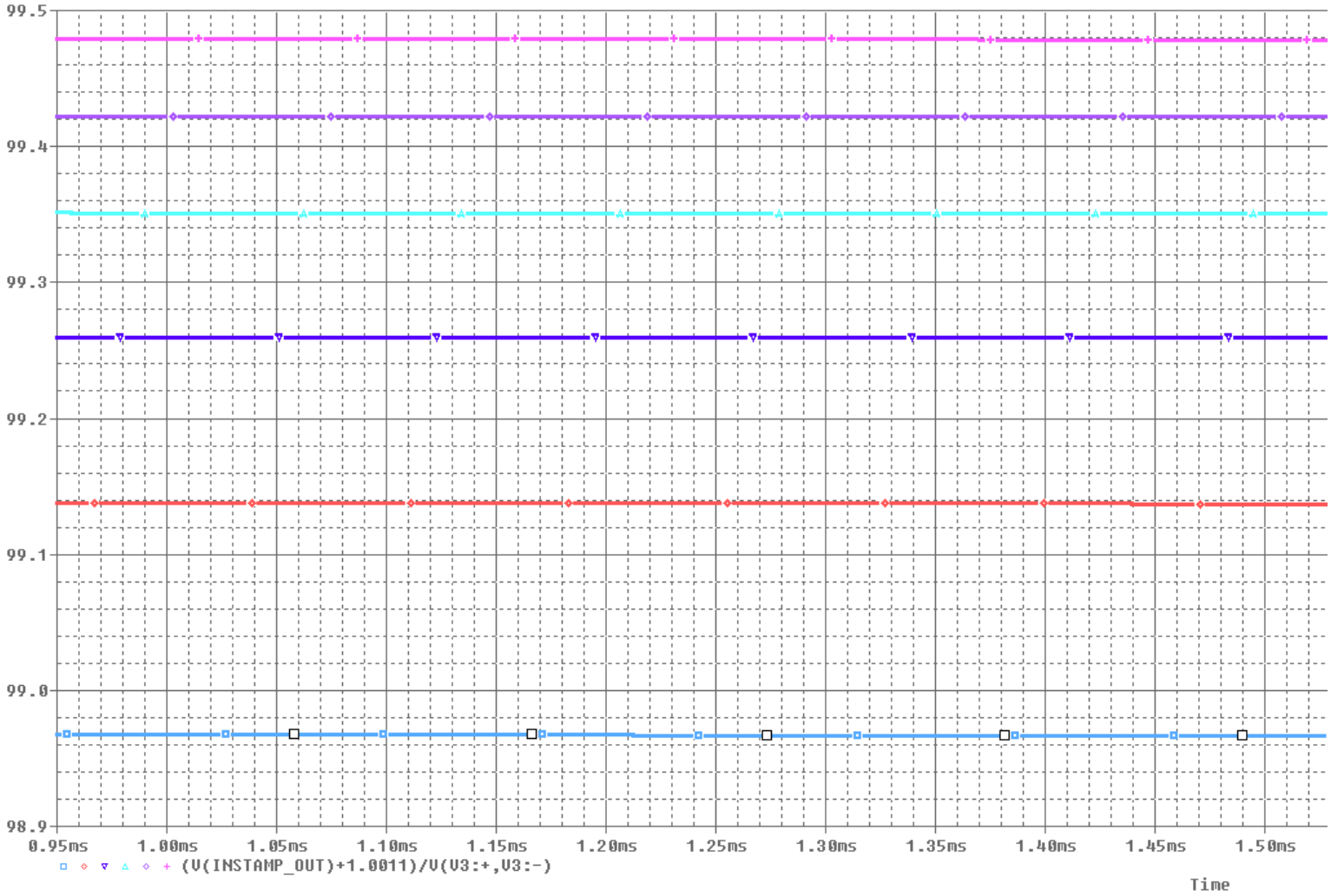

Figure 34 – Instrumentation amplifier gain over input range.

Prototyping

The transponder circuit was constructed upon a copper clad substrate routed for the integrated circuits. Surface mount components were used for all the integrated circuits (IC), except that the sensor was through hole. A socket was used for mounting the sensor to the board to allow for alternate sensor studies in the future. Leaded through hole passives were soldered to the board to complete the circuitry. Banana jacks were utilized for power connections. The finished prototype is shown in Figure 35.

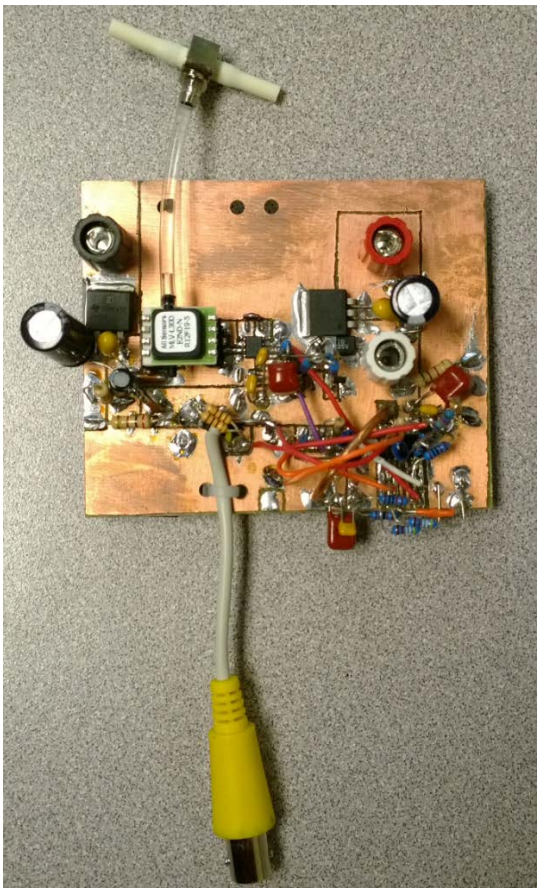

Figure 35 – Transponder test circuit prototype.

Evaluation

The test setup for the transponder evaluation is shown in Figure 36. A ¼" polyurethane tube was mounted to a measuring rod and then marked to be used in producing the fluid pressure upon the inlet port. The ¼" tubing was large enough to prevent surface tension from trapping air within the tubing. Graduations of 10 mm of fluid was marked for the first 100 mm of H_2O. Thereafter graduations of 100 mm H_2O was marked and water was dispensed through a dropper for the test fluid. Reducing fittings were used to adapt the ¼" tubing to 0.066" polyurethane tubing compatible with the sensor input port. A tee was used to introduce the fluid to the pressure sensor inlet port (Port A), while also allowing a fluid drain. Air was bled from the input system such that the water was incident upon the sensor's diaphragm. The second sensor port (Port B) was left open as an atmospheric reference.

An Agilent digital storage oscilloscope, model DSO-X 3104A, was used during the testing of the transponder circuit, which offered a 1 GHz bandwidth and 5 GSa/sec. A Topward 6302D power supply powered the transponder with ±5V and a Fluke model 87 multimeter was used for various measurements though out the testing. An Agilent 33220A, 20 MHz waveform generator, was used to generate a gating pulse for periodic resetting of the transponder in most of the statistical studies. The pulse generation was set to a 50 Hz rate, 50% duty cycle.

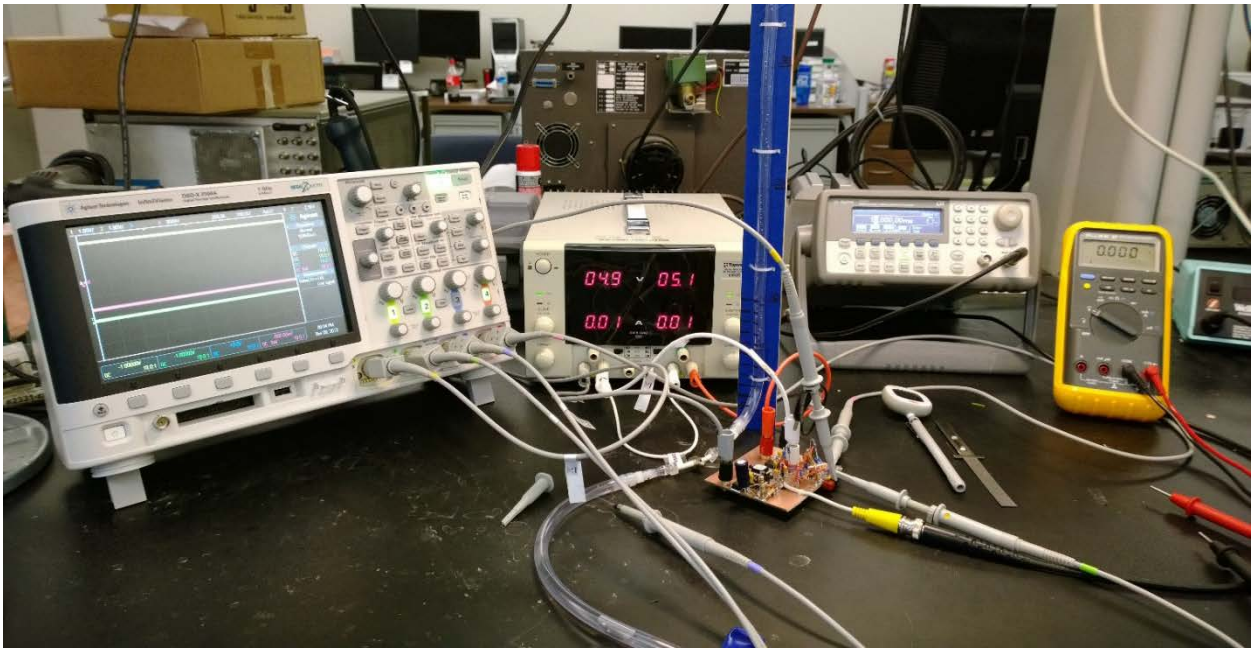

Figure 36 – Test setup for transponder pressure testing.

Chapter 4 - Results and Discussion

Measurements were made for bias conditions, noise, transient responses, transfer functions, statistical metrics, as well as drift and a limit of detection determination. The following sections describe the results from each of these types of measurements and then follows with a discussion of the challenges presented during the testing.

Bias Conditions

Table 4 shows the recorded bias conditions for the transponder. The sensor input port was offset from the table top by 22 mm and therefore, the water column pressure calculations accounted for this offset. The overall power consumption of the transponder was 71 mW, which fared well with earlier literature reviews of inductive telemetry demonstrations of 100 mW or 250 mW capabilities. The 71 mW allows future headroom for the oscillator power consumption. Offset of the instrumentation amplifier was -19 mV arising from the measured Neg_1V reference error and a very small input offset present at the output after a gain of 100. The sensor output at the 22 mm H_2O datum was -1.020 V.

Table 4 – Measured bias conditions.

Item	Conditions (23.6°C)	Metric	Unit
Sensor Port Offset		22	mm
VDD	+5V In	2.506	V
IDD	2.506 output	17	mA
VSS	-5V In	-2.552	V
ISS	-2.552 output	11	mA
Power		71	mW
Inst Amp Offset	Inputs Shorted	-1.019	V
Reference		1.225	V
Neg_1V		-1.018	V
Neg_2V		-2.016	V
Sensor Output	Zeroed with 22 mm water column.	-1.020	V

Noise Measurements

Figure 37 shows the wideband noise present upon the probe of the scope. Since the circuits within the transponder are of low bandwidth (i.e. generally below 1 MHz), further noise measurements were made with the band limited option of the scope, which limits the bandwidth to approximately 20 MHz. Figure 38 and Figure 39 show the measured noise of the +2.5V and -2.5V rails consisting of 1.25 mV and 1.31 mV, respectively. Figure 40 shows the output noise of the instrumentation amplifier of 1.39 mV rms, which compares well with the hand calculations based on dominant noise contributors. Lastly, the noise of the integrator output was measured by fast sampling the ramp such that the amplitude could be examined. Figure 41 shows the integrator output noise with a peak to peak measurement and sigma of about 2.2 mV.

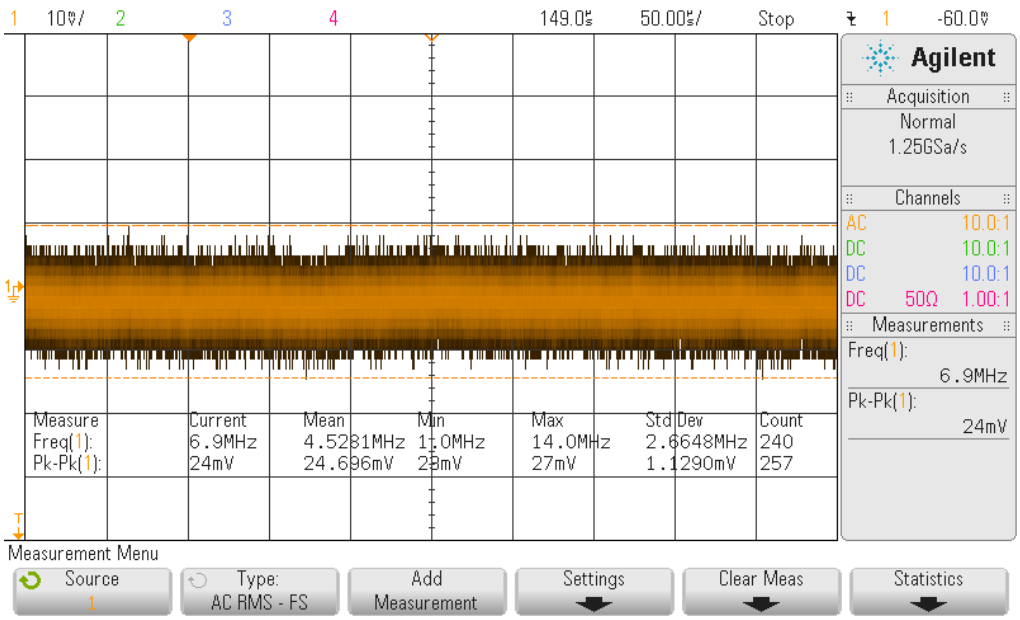

Figure 37 – Wideband (1 GHz) noise present upon oscilloscope probe.

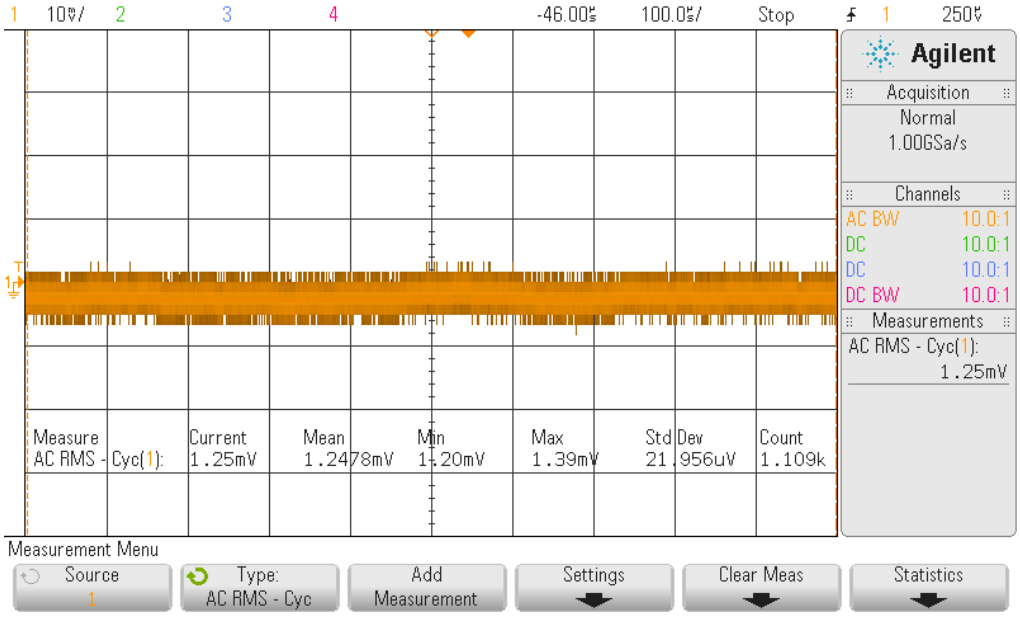

Figure 38 – Positive 2.5 V measured noise (1.25 mV rms).

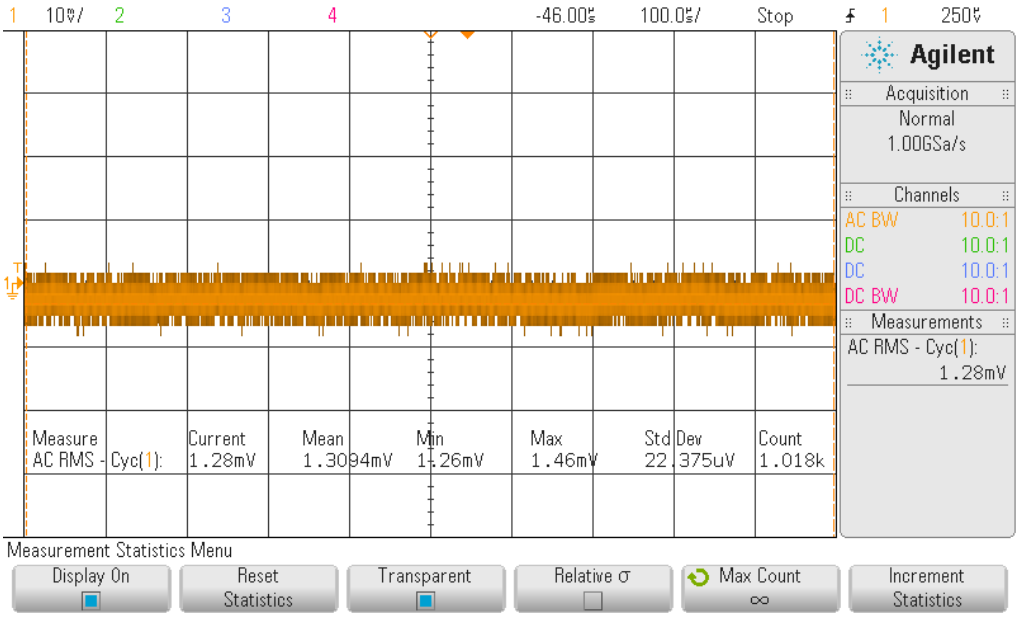

Figure 39 – Negative 2.5 V measured noise (1.31 mV rms)

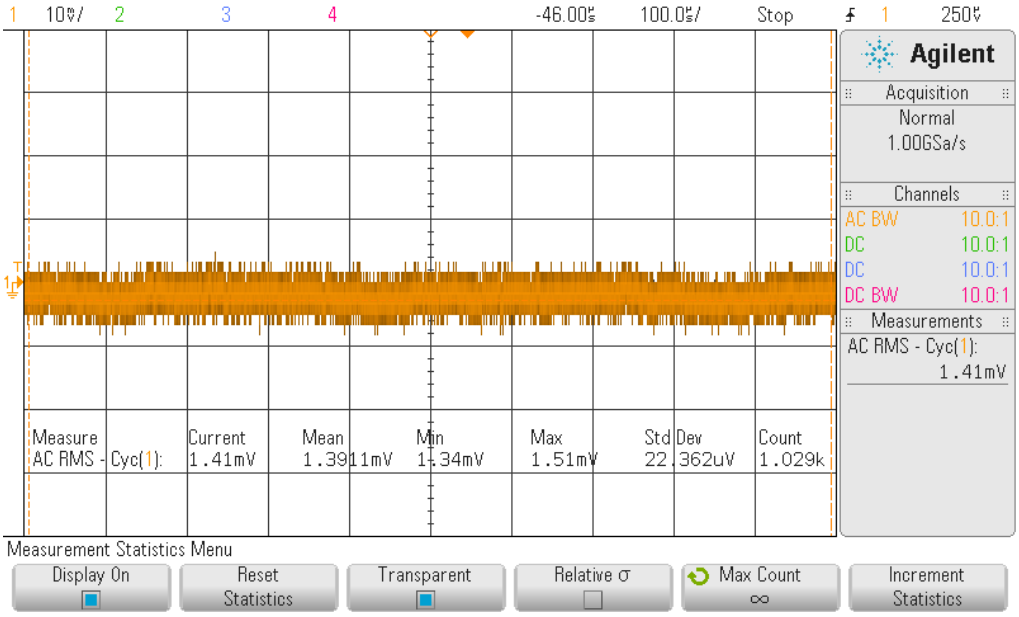

Figure 40 – Instrumentation amplifier output noise (1.39 mV rms)

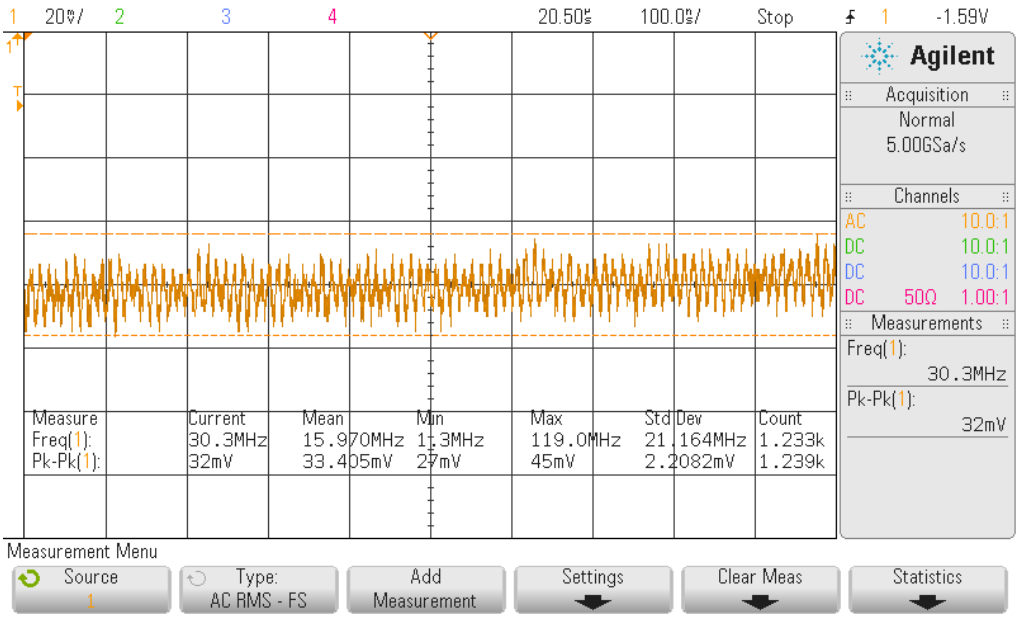

Figure 41 - Integrator output noise.

Transient Responses

Figure 42 shows a conversion for the datum point at 22 mm H_2O (i.e. effectively 0 mm H_2O). Once the active low /Start signal begins, the ramp circuit increases steadily from approximately -2 V. At the point where the ramp signal equates to the sensor amplified signal, the active high Stop rises. Figure 43 shows a 60 mm H_2O /Start to Stop conversion.

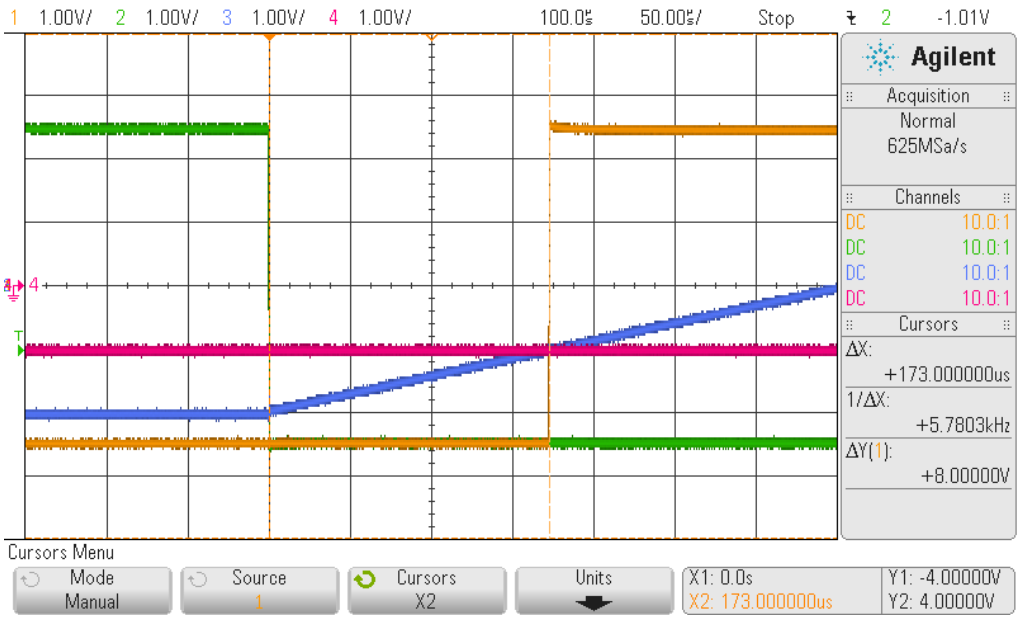

Figure 42 – Pressure conversion (/Start in green, Stop in yellow, sensor signal in magenta, integrator output in blue).

The integrator's ramp output is shown in Figure 44, measured at 800 µsec. The ramp begins rising from an approximate -2.013 V until the operational amplifier saturates near

2.463 V. Ideally, the ramp would terminate at approximately 852 µsec for 2.463 volts using a gain of 500 nsec per 2.62 mV (i.e. 1 mm H_2O). Figure 45 compares the measured ramp versus simulated and ideal. The measured ramp calculates to a +6.3% gain error compared to ideal. The simulated ramp was formerly calculated to have a negative gain error of about -4%. In the simulated case, the gain error was dominated by the reduced input voltage resulting from an error by the -2V reference and then secondly slowed by a MOSFET leakage current. The same is true in the actual case except for a positive gain error, where the bias conditions, shown in Table 4, present a VSS of -2.552 V with a -2V reference of -2.016 V (i.e. integrator input of -0.536 V). These non-ideal voltages amount to about an estimated +7% positive gain error. In large part, the reduction from the estimated +7% to the measured +6.3% is predicted from the simulated leakage current of the gating MOSFET (~0.5%).

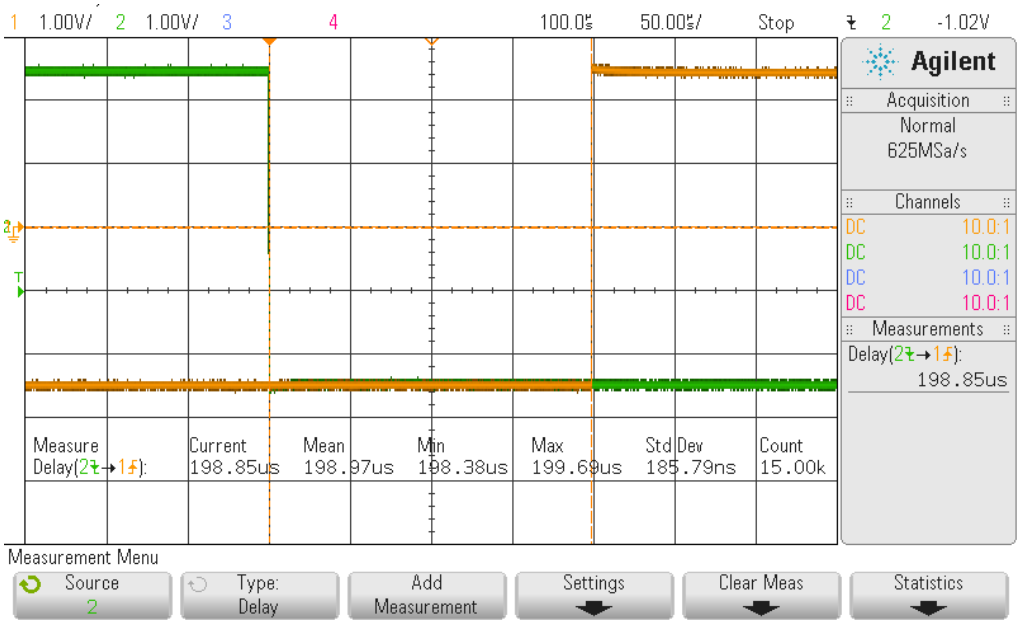

Figure 43 –Pressure conversion for effective 60 mm H2O (/Start in green, Stop in yellow).

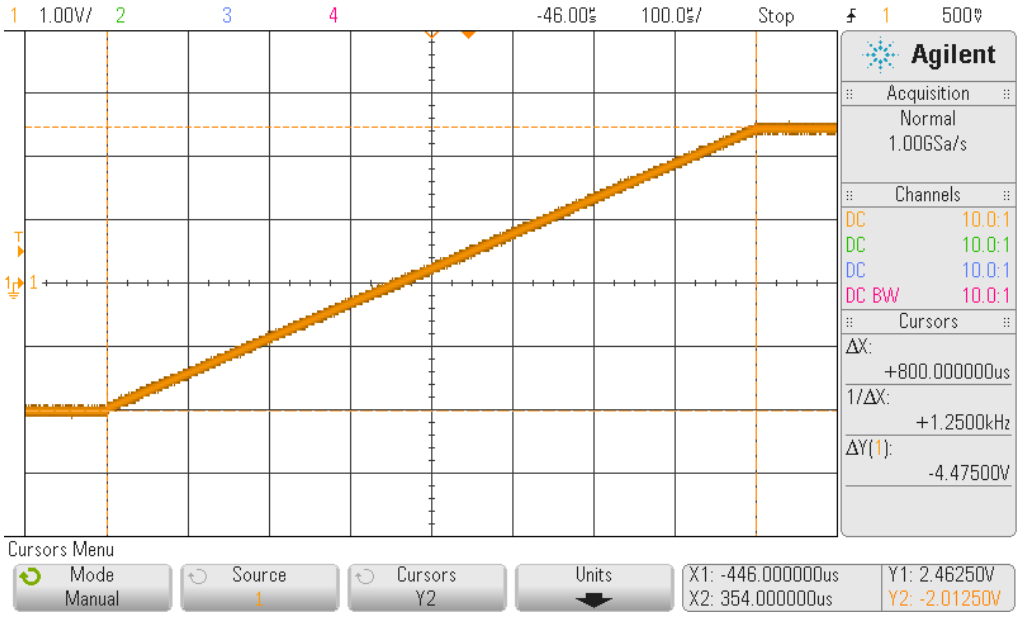

Figure 44 –Integrator ramp output (~800 µsec).

Transfer Functions

Figure 46 shows the results of measuring the instrumentation amplifier's output over the full range of pressure inputs. Both increasing pressure and decreasing pressure was measured in order to assess any hysteresis effects. As can be seen from the figure, the band of pressures from 300 to 500 mm H_20 presented some hysteresis effects. This results in a worst case average non-linearity of 1.5% of the full scale value. The average of all non-linearity was only 0.2%. The offset, which was due to the -1V reference error, was -20 mV.

Figure 47 shows the measured time encoding, which is a result of the comparator's comparison of the ramp function graphed in Figure 45 to the amplified sensor signal illustrated in Figure 46. The transponder timing output worst case non-linearity calculated to 0.85% with an overall average non-linearity of only 0.02% of the full scale value. The output function was offset by -18 µsec. It also possessed a gain error of -5% resulting in an actual gain of 475.5 nsec/mm H_2O. Both of these effects are due to the gain error present within the ramp function. Since the ramp begins at approximately -2 V, a gain error in the ramp results in an offset occurring at -1 V for timing encoding. Based on the +6.3% ramp gain error, this calculates to a -10 µsec timing offset at -1 V. Also, because the instrumentation amplifier is offset by -20 mV, this results in a -4 µsec offset at the output of the comparator. Further, input voltage offset for the LM339A is typically specified for 2 mV, but can be up to 4 mV, accounting for almost another 1 µsec. The additional difference is likely a result of the uncertainty in the cursor measurement of the 800 µsec ramp period shown in Figure 44. The output timing gain

error of -5% is a result of the integrator's positive ramp gain error. As described in the simulation results, a positive gain error of the ramp function will generate a negative gain error at the output, which is intuitive given that a faster ramp will result in shorter Start to Stop intervals.

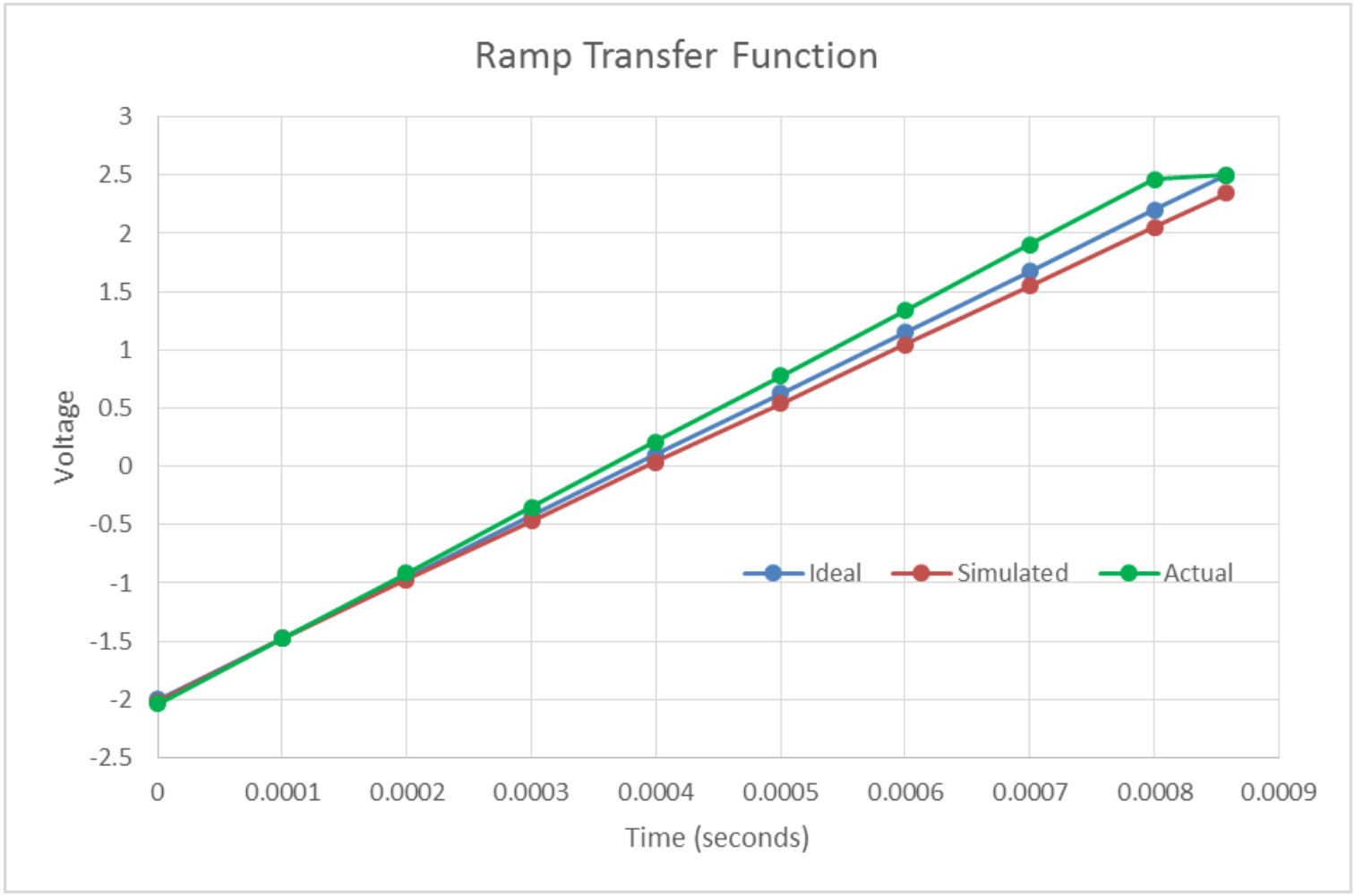

Figure 45 – Measured versus ideal and simulated for the integrator ramp output.

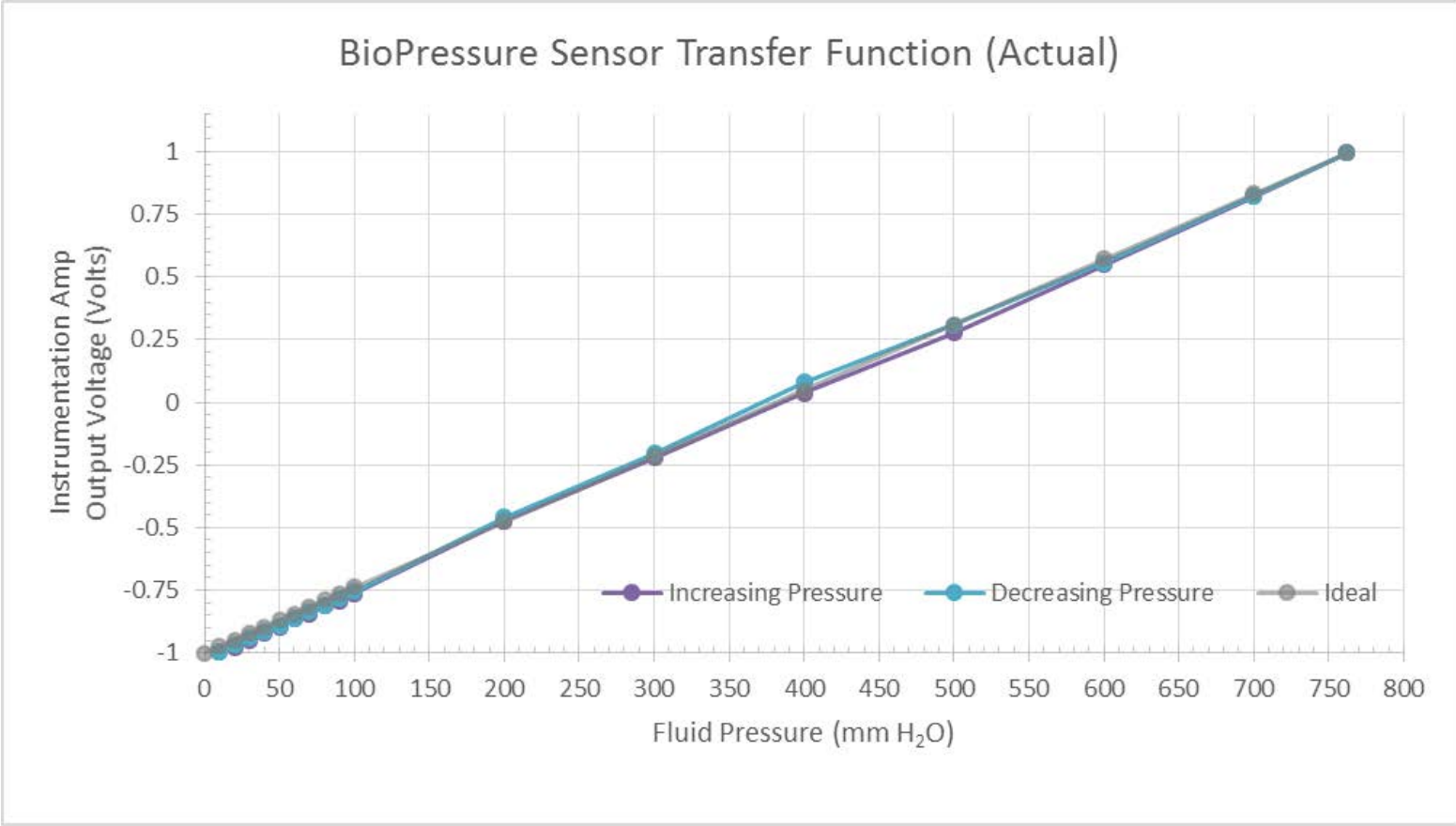

Figure 46 –Instrumentation amplifier output over range of pressure inputs.

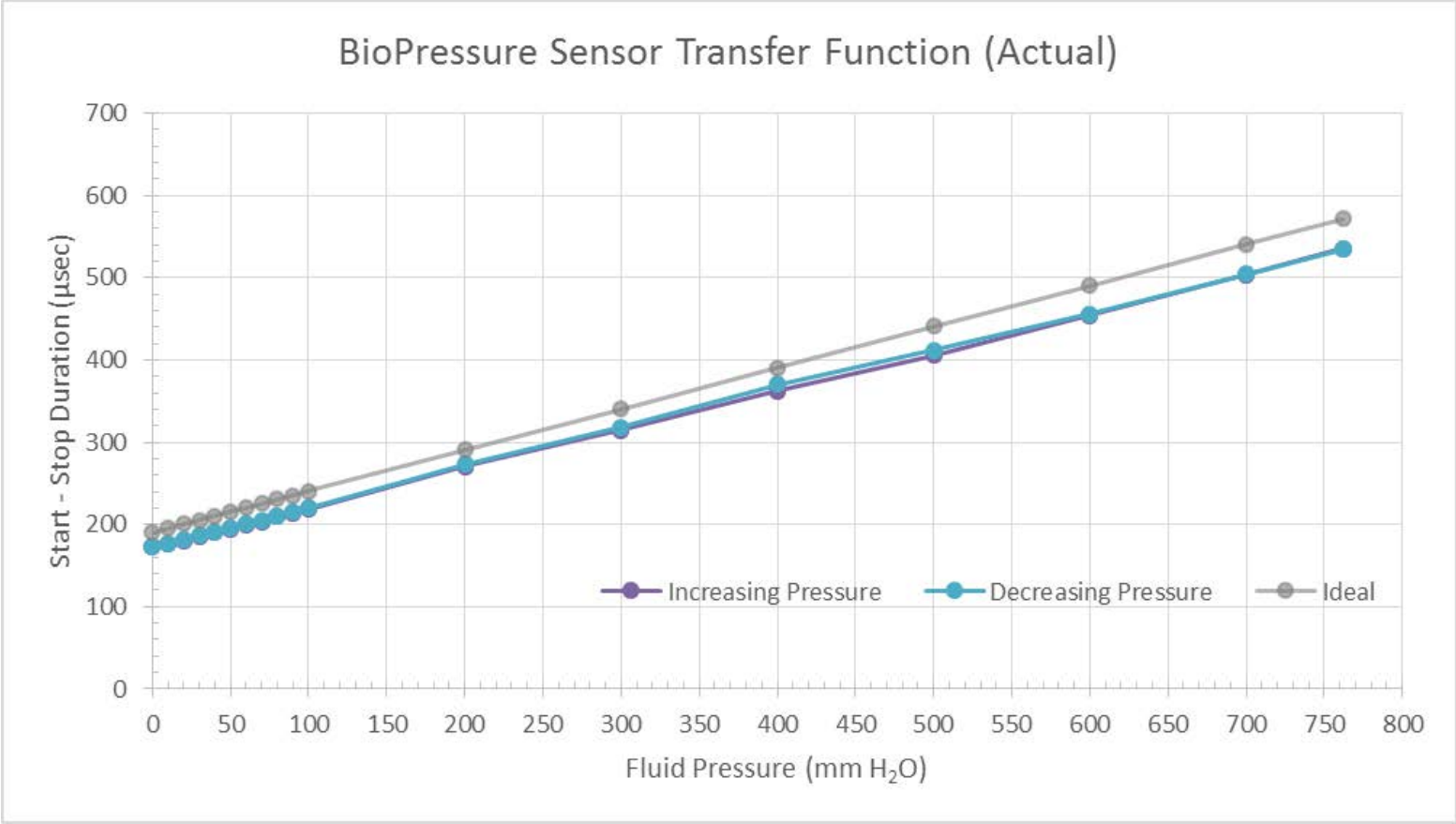

Figure 47 – Transponder output over range of pressure inputs.

Drift

Daily pressure values were recorded for 60 mm H_2O to assess any drift of the transponder. 60 mm H_20 was chosen since it represents the low end of normal ICP, while yet allowing a significant pressure magnitude to reduce measurement error in reproducing the test day to day. Figure 48 shows the recorded values from the output of the instrumentation amplifier. The mean value was -0.8577 V representing 61.96 mm H_2O. The standard deviation was 16 mV or 2.08 mm H_2O. The overall drift was calculated to be -0.05 mm H_2O per day or -17 mm H_2O per year.

Limit of Detection

Figure 49 shows the results for a limit of detection test whereby the transponder output was recorded for approximately 1,000 samples. 0 mm H_2O was recorded at a mean of 171.88 µsec while 1 mm H_2O was recorded at 172.80 µsec. Both measurements had a standard deviation of 148 nsec. There is a six sigma separation between the two measurements and therefore represents a well differentiated detection level of 1 mm H_2O.

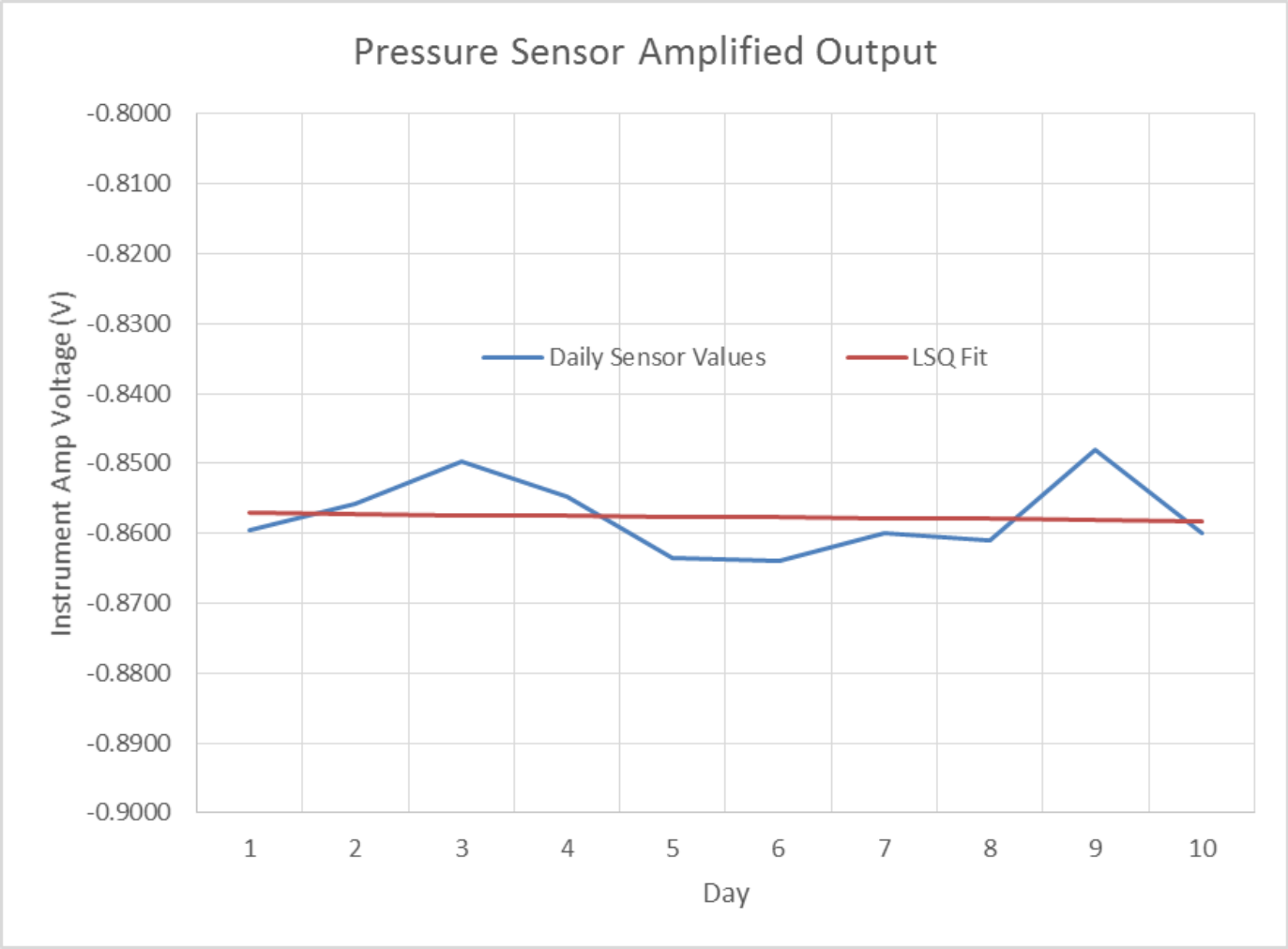

Figure 48 –Measured ten day drift for 60 mm H_2O.

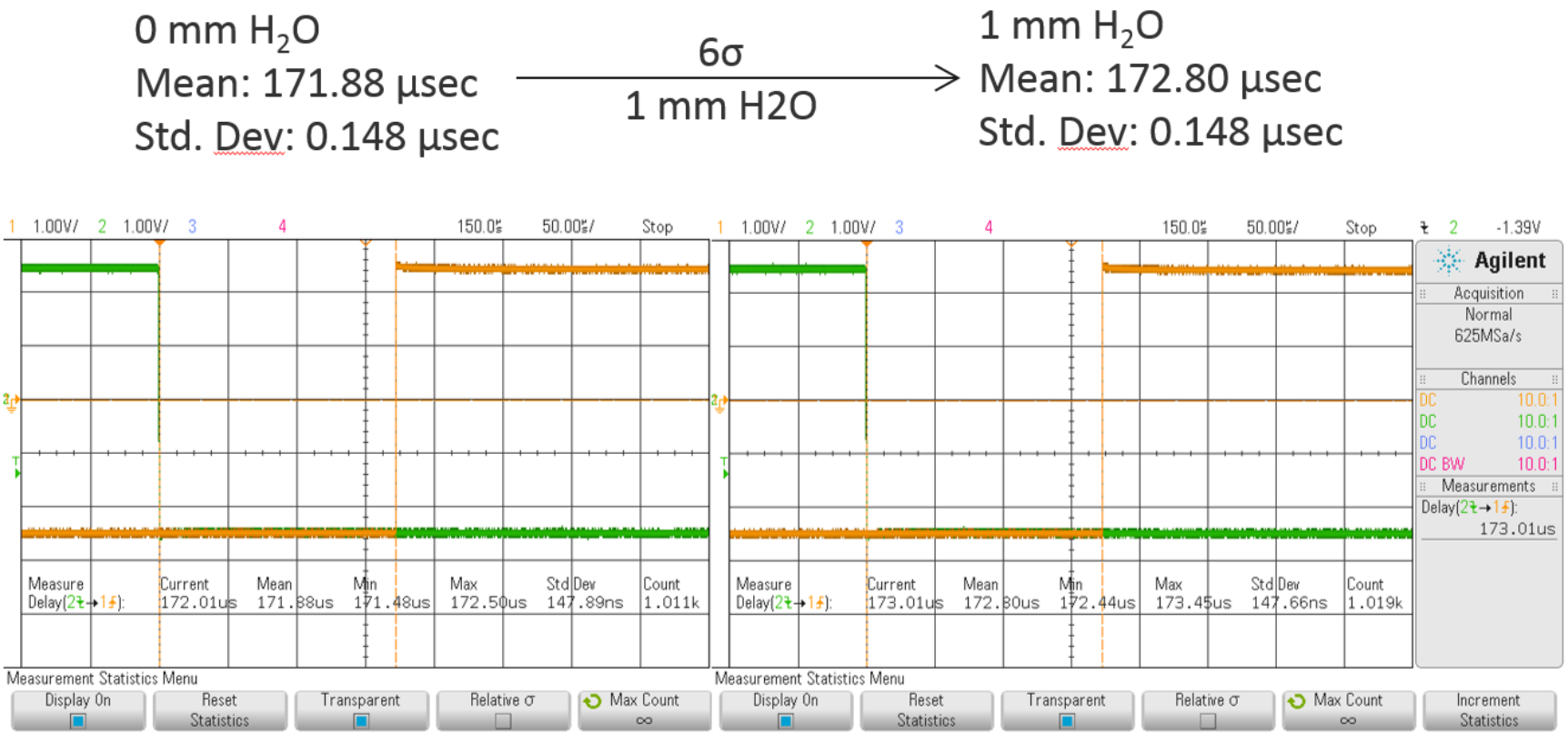

Figure 49 –Limit of detection test for 0 mm H_2O versus 1 mm H_2O.

Challenges

The design, construction, and testing of the transponder presented a number of challenges. These range from the low voltage configuration of the transponder through various offsets, to the copper clad surface mount prototyping, and to the setup and repeatability of very low fluid pressures. Additionally, there were a couple of power up testing issues, which were captured, as described below.

Triangular wave noise was observed upon the Stop signal in its low state during the course of testing. The noise was also observed in other areas of the circuitry, including the gain setting resistor of the instrumentation amplifier. With further debugging, the source of the noise was discovered to be the -2.5 V regulator comprised of about a 300 mV p-p triangular wave as shown in Figure 50. The regulator's output filtering capacitor had become disconnected due to a dry solder joint. After rewetting the solder joint, the noise fell to 1.31 mV rms as shown in Figure 39.

A more challenging issue, however, was that discovered during startup testing illustrated in Figure 51. In the figure, it can be noticed that a Stop had already occurred by the time power up settling occurs and that /Start begins immediately with -2.5 V power settling. The issue is apparent that the -2.5 V regulator possesses a delay, which results in the startup delay circuit's RC being charged before the -2.5 V powers the remainder of the circuitry. This causes an immediate /Start condition. Furthermore, since the -2.5 V regulator is actually about +0.75 V until stabilization, it temporarily offsets the instrumentation amplifier's output to a positive voltage instead of at -1V

baseline, which compared with the -2V ramp output, causes an immediate Stop at the onset of power.

To remedy the -2.5 V regulator delay, which rendered the startup RC inadequate, an extra comparator was utilized as shown in Figure 52. In the figure it can be seen that an open collector comparator output is used to pull down the startup delay circuit's RC, which will remain in high impedance until the comparator activates. The comparator is configured such that its open collector activates once VSS, on the non-inverting input, drops below ground level present upon the inverting input. At which point, the comparator output, capable of at least 6 mA, will pull down R5 and C2, which only requires 350 μA, maximum. The existing 14.3 kΩ resistor will also extend the delay circuit timing since the RC now becomes charged across VDD-VSS instead of only VDD-ground. The delay extends to a calculated 1.35 msec.

Figure 53 shows the measured results of the attempted countermeasure, whereby the Stop has still already occurred by the time the circuit powers up and /Start essentially follows the slow powering of the -2.5 V. Other measurements showed that the comparator output was non-linear and actually pulling current even though the -2.5 V regulator was supplying about +0.75 V. This drain of current in the delay's RC still caused the capacitor to be charged by the time the -2.5 V regulator stabilized, which resulted in an immediate /Start condition, as well as an already present Stop.

To finally resolve the power up issue, the circuit of Figure 54 was employed whereby an N-MOS was used with its gate tied to ground and its source to VSS. In this way, no

current will sink into the MOSFET's drain until VSS goes negative and applies the minimum gate to source voltage of 0.4V. Furthermore, the RC delay was increased to 5 msec with a 36 kΩ resistor. As can be seen from Figure 55, the countermeasure resolved the problem and delays a /Start condition until approximately 5 msec post negative regulator power up, thereby allowing the sensor output to stabilize.

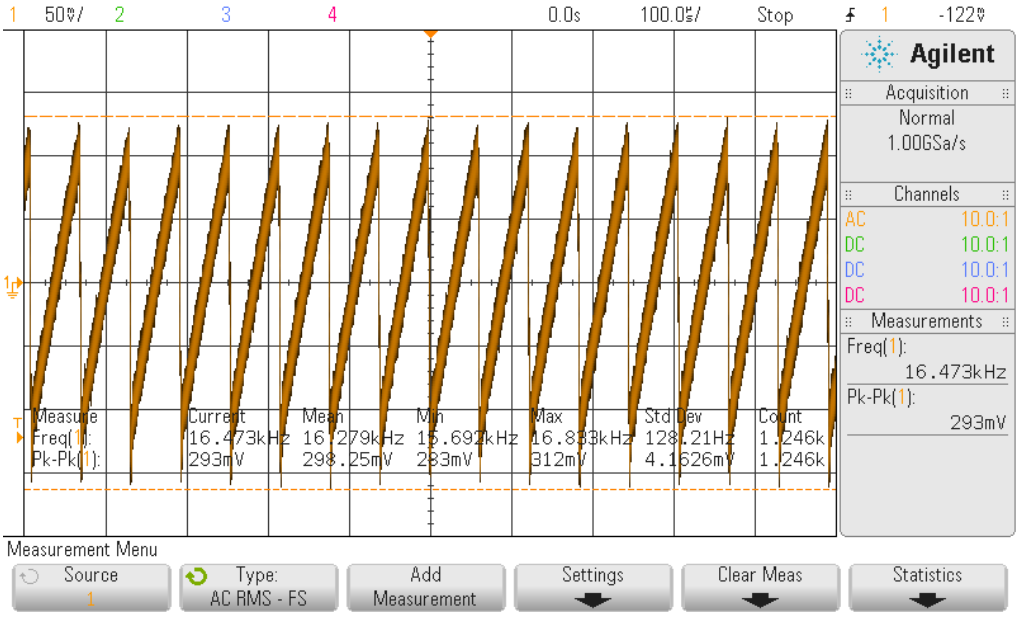

Figure 50 – Power supply noise present upon the -2.5V.

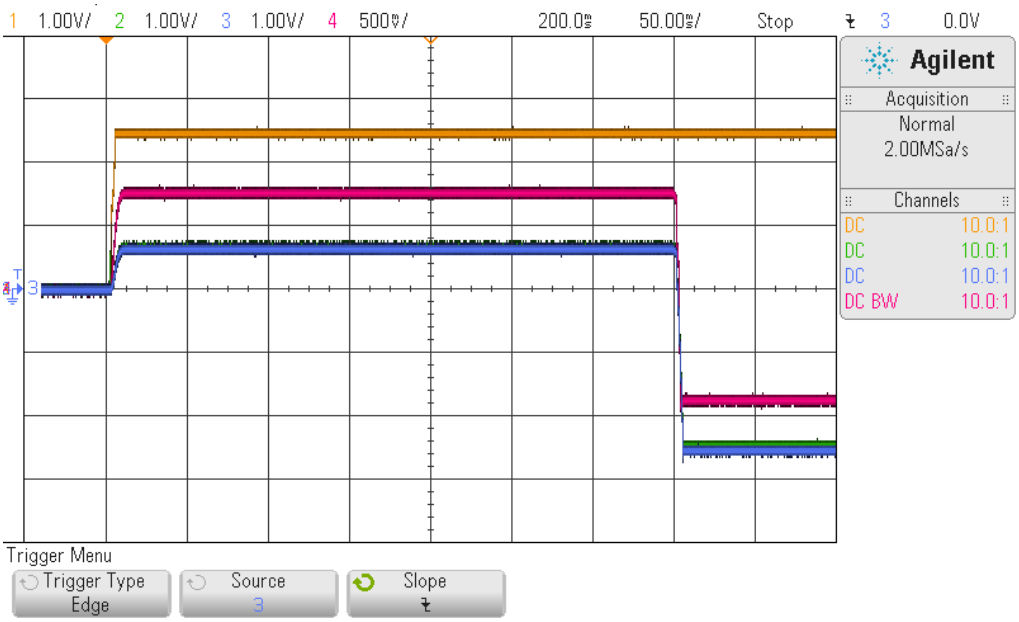

Figure 51 –Initial startup conditions (Stop in yellow, /Start in green, instrumentation amplifier output in magenta, -2.5V in blue)

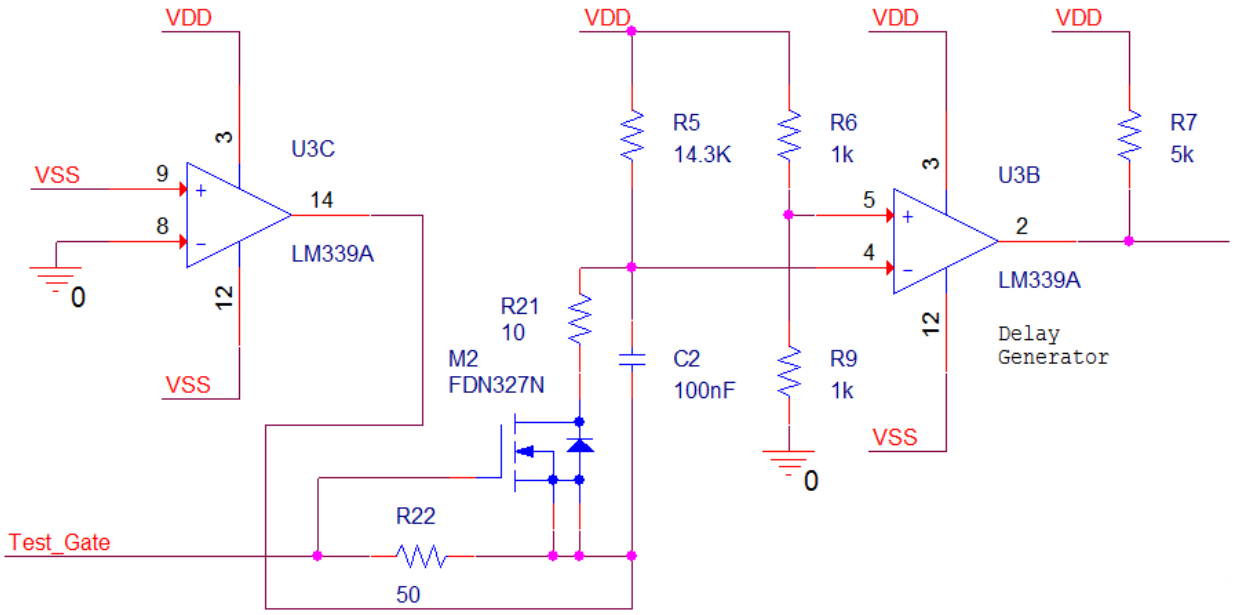

Figure 52 –Negative regulator delay startup mitigation.

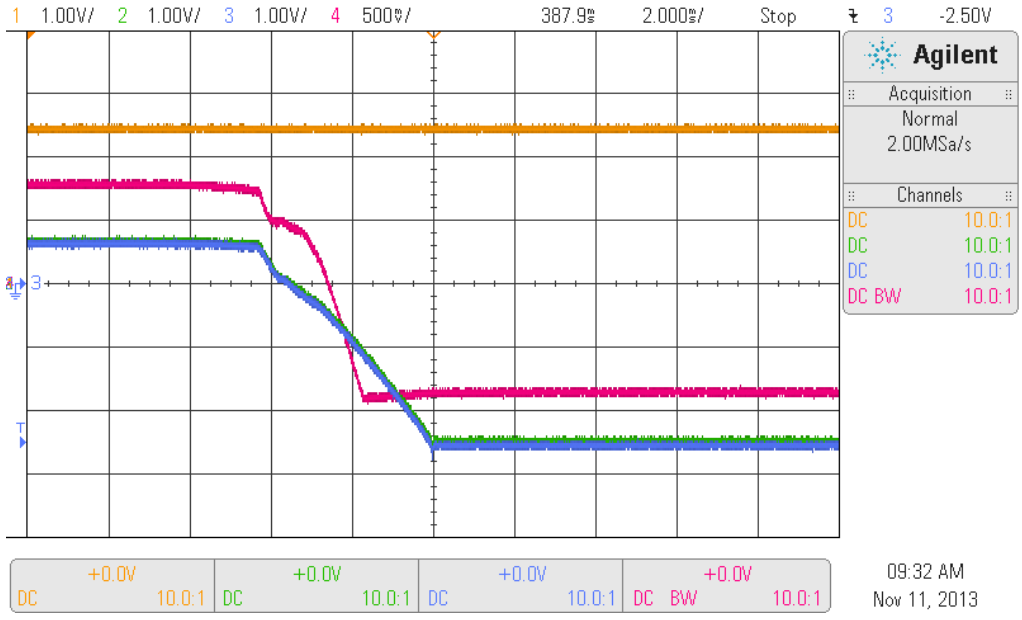

Figure 53 – Comparator mitigation startup results (Stop in yellow, /Start in green, instrumentation amplifier output in magenta, -2.5V in blue).

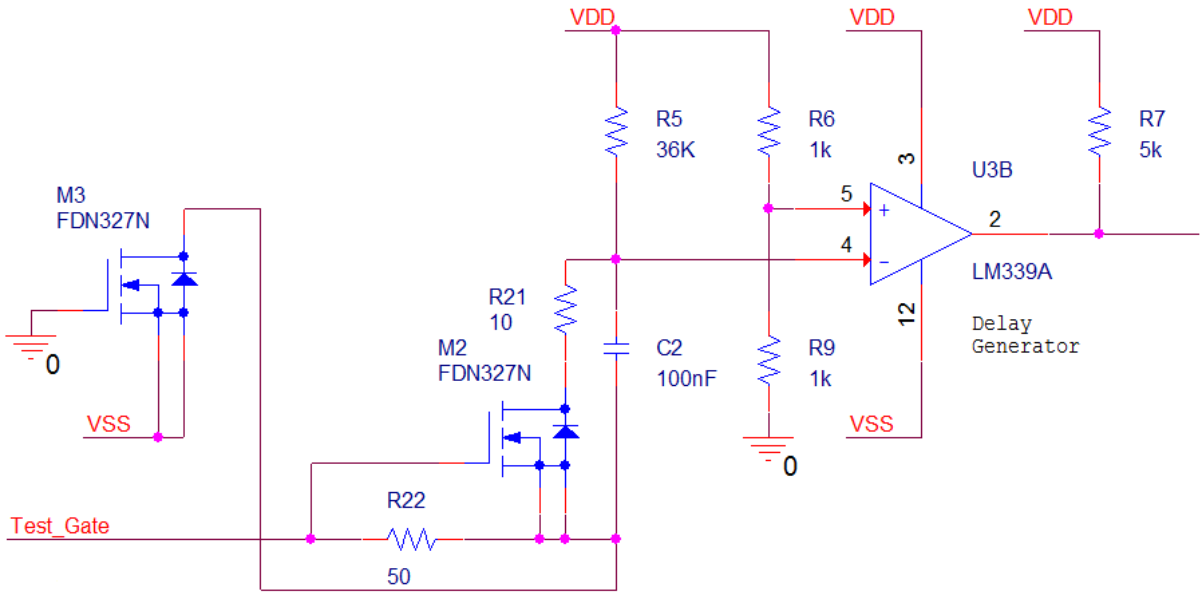

Figure 54 - Negative regulator delay final startup mitigation.

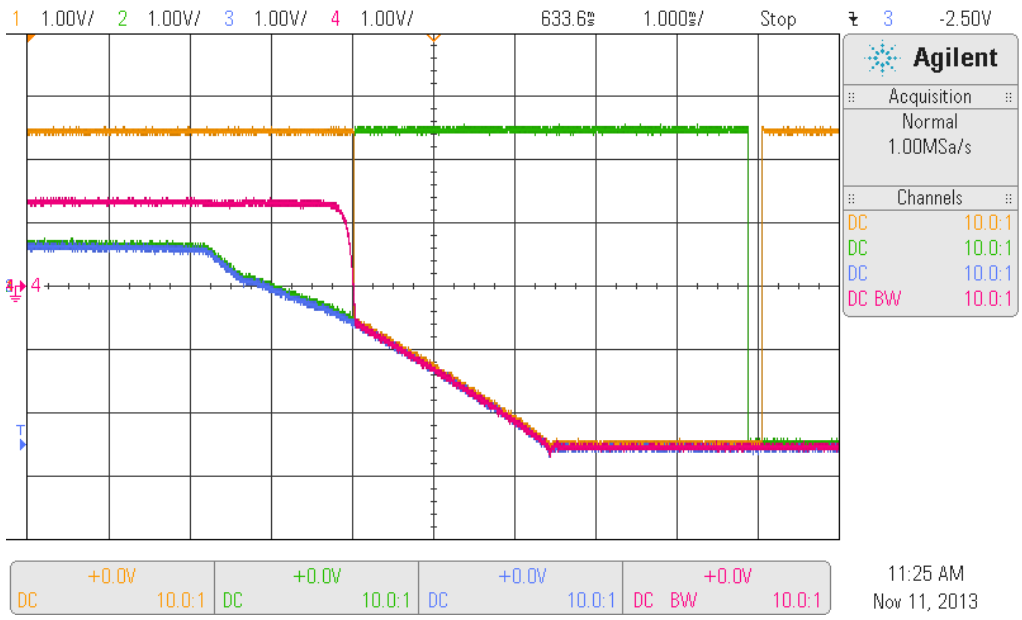

Figure 55 – Final mitigation startup results (Stop in yellow, /Start in green, instrumentation amplifier output in magenta, -2.5V in blue).

Chapter 5 - Conclusions and Recommendations

In this research, intracranial pressure (ICP) measurement techniques were investigated, which found that all quantitative means of assessment currently rely upon invasive penetration of the CSF space or of the brain's parenchyma. Prevailing commercial equipment for performing such measurements were found to all be configured upon a tethered sensor with bedside instrumentation readout, which has been shown to suffer significantly from drift. Not only is this approach expensive, requiring in hospital assessments, but it is also risky to the patient. The work of this thesis has been to develop and evaluate a sensor and low power transponder core to facilitate potential long-term implantation that would allow periodic pressure measurements non-invasively.

A literature review of the various types of ICP transduction indicated that micro-strain sensing presented the least amount of drift primarily due to temperature compensation availability, which compensates for ex-vivo zeroing versus in-vivo measurements. Therefore, this investigation evaluated a biocompatible micro-strain sensor, suitable for very low pressure transduction, along with a low power amplification circuit that, combined with an amplitude-to-time converter, provided a pulse width modulated output. The transponder circuit was constructed and a fluid pressure column was used to evaluate various performance aspects of the device, including drift.

The transponder circuit consumed only 71 mW of power at ±2.5V and as shown in the literature review, is easily compatible with prevailing examples of telemetric power and

data transfer techniques. Table 5 shows the performance metrics of the tested transponder. Linearity is shown at 0.85% worst case, but was typically 0.02%. The sensitivity, which was designed for 500 nsec per mm H_2O, was actually about 476 due to gain error within the sweep circuit. The resolution was taken at worst case signal noise conditions, which was at the output of the instrumentation amplifier yielding 1.25 mm H_2O. Limit of detection was shown at six sigma separation to be only 1 mm H_2O. Precision was derived from the daily drift values and was calculated at 6.25 mm H_2O while the drift equated to 17 mm H_2O per year based upon a least squares linear fit of the ten day data for 60 mm H_2O baseline.

Compared to fiber optic metrics reported within the literature, the transponder results were outstanding with an annual drift estimate of only 17 mm H_2O versus an average daily drift of 43.5 mm H_2O found in the fiber optic Camino devices. Furthermore, the results of this research exceed those found by Koskinen and Olivecrona in their study of the Codman Microsensor System, which presented a drift of ±27 mm H_2O over a week. Never the less, Koskinen and Olivecrona reported these results as clinically acceptable for such low drift. Although further study is warranted for long term drift of the device studied within this research, the initial results indicate the transponder evaluated to be a potential candidate for further development and possible preclinical studies.

Future work for the transponder includes the improvement of the prototype and test construction to minimize test repeatability error and to evaluate additional devices for accumulating statistical metrics from device to device. RF shielding is recommended to be added to the prototypes in order to minimize coupling noise. Trim circuitry for

zeroing output offsets and gain error could also be added to the voltage references and integrator circuitry. Furthermore, temperature testing in order to evaluate the test conditions influence, could be performed, especially at the desired in-vivo temperature of approximately 37°C. Lastly, the development of an integrated circuit in order to produce a compact implantable size could be pursued, including a telemetry unit, with the intent for a multi-chip module that includes the microstrain sensor within a biocompatible titanium encasement for further testing.

Table 5 – Transponder performance metrics.

Metric	Figure	Units	Notes
Linearity	0.85	% full scale.	Worst case figure.
Sensitivity	475.5	nsec/mm H_2O	
Resolution	1.25	mm H_2O	Worst case derived from noise of amplified sensor signal.
Limit of Detection	1	mm H_2O	6σ
Precision	6.25	mm H_2O	Derived from 3σ of ten day drift.
Drift	-17	mm H_2O per year.	Least squares fit of ten day drift.

References

[1] H. Kimelberg, "Water Homeostasis in the Brain: Basic Concepts," *Neuroscience,* vol. 129, pp. 851-860, 2004.

[2] R. Ravi and R. Morgan, "Intracranial Pressure Monitoring," *Current Anaesthesia and Critical Care,* vol. 14, pp. 229-235, 2003.

[3] N. Lundberg, "Continuous Recording and Control of Ventricular Fluid Pressure in Neurosurgical Practice," *Acta Psychiatrica Scandinavica Supplement,* vol. 36, no. Suppl 149, pp. 1-193, 1960.

[4] K. Holloway, T. Barnes and e. a. S. Choi, "Ventriculostomy infections: the effect of monitoring duration and catheter exchange in 584 patients.," *Journal of Neurosurgery,* vol. 85, pp. 419-424, 1996.

[5] I. Piper, A. Barnes, D. Smith and L. Dunn, "The Camino Intracranial Pressure Sensor: Is it Optimal Technology? An Internal Audit with a Review of Current Intracranial Pressure Monitoring Technologies," *Neurosurgery,* vol. 49, no. 5, pp. 1158-1165, 2001.

[6] M. Rosner and D. Becker, "ICP monitoring: Complications and Associated Factors," *Clinical Neurosurgery,* vol. 23, pp. 494-519, 1976.

[7] FISO, "Fiber Optic Sensing Solutions for the Medical Industry," 2009. [Online]. Available: http://www.fiso.com/section.php?p=11. [Accessed 8 July 2013].

[8] Integra LifeSciences, "Neuromonitoring Catalog," 2013. [Online]. Available: http://www.integralife.com/eCatalogs/Neuro-monitoring/Neuromonitoring%20Catalog%20NS897-10_09.pdf. [Accessed 22 August 2013].

[9] DePuy Synthes, "Codman Microsensor ICP Transducer," 22 August 2013. [Online]. Available: http://www.depuy.com/uk/healthcare-professionals/product-details/codman-microsensor. [Accessed 22 August 2013].

[10] L.-O. D. Koskinen and M. Olivecrona, "Clinical Experience with the Intraparenchymal Intracranial Pressure Monitoring Codman MicroSensor System," *Neurosurgery,* vol. 56, pp. 693-698, 2005.

[11] "CardioMEMS," CardioMEMS, Inc., 2012. [Online]. Available: www.cardiomems.com. [Accessed 7 November 2013].

[12] C. Wiegand and P. Richards, "Measurement of Intracranial Pressure in Children: A Critical Review of Current Methods," *Developmental Medicine adn Child Neurology,* vol. 49, pp. 935-941, 2007.

[13] W. Newman, A. Hollman, G. Dutton and R. Carachi, "Measurement of Optic Nerve Sheath Diameter by Ultrasound: A Means of Detecting Acute Raised Intracranial Pressure in Hydrocephalus," *British Journal of Ophthalmology ,* vol. 86, pp. 1109-1113, 2002.

[14] M. Czonsnka and J. Pickard, "Monitoring and Interpretation of Intracranial Pressure," *Journal of Neurology Neurosurgery Psychiatry,* vol. 75, pp. 813-821, 2004.

[15] L. Desch, "Longitudinal Stability of Visual Evoked Potentials in Children and Adolescents with Hydrocephalus.," *Developmental Medicine and Child Neurology,* vol. 43, pp. 113-117, 2001.

[16] Integra Life Sciences, "Integra Camino Complete Intracranial Pressure Kit," 2009. [Online]. Available: http://integralife.com/products%2FPDFs%2FNeuroCriticalCare%2FCamino%20Brochure.pdf. [Accessed 9 July 2013].

[17] DePuy (J&J Codman), "CODMAN MICROSENSOR ICP Transducer," 18 May 2011. [Online]. Available: http://www.depuy.com/sites/default/files/products/files/Microsensor%20IFU.pdf. [Accessed 9 July 2013].

[18] T. Luerssen, "Intracranial pressure: Current status in monitoring and management.," *Elsevier: Pediatric Neurology,* vol. 4, pp. 146-155, 1997.

[19] I. Pople, M. Muhlbauer, R. Sanford and e. al., "Results and Complications of Intraaranial Pressure Monitoring in 303 Children.," *Pediatric Neurosurgery,* vol. 23, pp. 64-67, 1995.

[20] S. Shapiro, R. Bowman, J. Callahan and e. al., "The Fiberoptic Intraparenchymal Cerbral Pressure Monitor in 244 Patients," *Surgical Neurology,* vol. 145, pp. 278-282, 1996.

[21] W. Young, Roark's Formulas for Stress and Strain, McGraw-Hill Professional, 2011.

[22] M. D. Giovanni, Flat and Corrugated Diaphragm Design Handbook, New York: Marcel Dekker, 1982.

[23] N. Ross and C. Eynon, "Intracranial Pressure Monitoring," *Current Anaesthesia and Critical Care,* vol. 16, pp. 255-261, 2005.

[24] A. George, W. P. Chan, M. Narducci, Z. H. Kong and M. Je, "CMOS-MEMS Capacitive Sensors for Intra-cranial Pressure Monitoring: Sensor Fabrication & System Design," *IEEE ISOCC,* pp. 375-378, 2012.

[25] M. G. Allen, "Micromachined Endovascularly-Implantable Wireless Aneurysm Pressure Sensors: From Concept to Clinic," in *IEEE Solid-State Sensors, Actuators and Microsystems*, Seoul, 2005.

[26] Samaun, K. D. Wise and J. B. Angell, "An IC Piezoresistive Pressure Sensor for Biomedical Instrumentation," *IEEE Transactions on Biomedical Engineering,* vol. 20, no. 2, pp. 101-109, 1973.

[27] S. Y. Yurish, "Universal Interfacing Circuit for Resistive-Bridge Sensors," in *IEEE 2010 Conference on Sensor Device Technologies and Applications*, Venice, 2010.

[28] D. Crescini, V. Ferrari, Z. Vajna, D. Marioli, A. Taroni, A. Borgese, M. Marinelli, E. Milani, A. Paoletti, A. Tucciarone and G. Verona-Rinati, "Design and Development of a Piezoresistive Pressure Sensor on Micromachined Silicon for High Temperature Applicatoins and of a Signal-Conditioning Electronic Circuit," *Microsystem Technologies,* vol. 9, pp. 431-435, 2003.

[29] K. A. Townsend, J. W. Haslett, T. K. Tsang, M. N. El-Gamal and K. Iniewski, "Recent Advances and Future Trends in Low Power Wireless Systems for Medical Applications," in *IEEE Fifth International Workshop on System-on-Chip for Real-Time Applications*, Calgary, 2005.

[30] A. D. DeHennis and K. D. Wise, "A Fully Integrated Multisite Pressure Sensor for Wireless Arterial Flow Characterization," *IEEE Journal of Microelectromechanical Systems,* vol. 15, no. 3, pp. 678-685, 2006.

[31] M. Ghovanloo and S. Atluri, "An Integrated Full-Wave CMOS Rectifier With Built-In Back Telemetry for RFID and Implantable Biomedical Applications," *IEEE Transactions on Circuits and Systems,* vol. 55, no. 10, pp. 3328-3334, 2008.

[32] H. Ali, T. J. Ahmad and S. A. Khan, "Inductive Link Design for Medical Implants," in *IEEE Symposium on Industrial Electronics and Applications*, Kuala Lumpur, Malaysia, 2009.

[33] G. Wang, W. Liu, M. Sivaprakasam and G. A. Kendir, "Design and Analysis of an Adaptive Transcutaneous Power Telemetry for Biomedical Implants," *IEEE Transactions on Circuits and Systems,* vol. 52, no. 10, pp. 2109-2117, 2005.

[34] J. V. Ham and R. Puers, "A Power and Data Front-end IC for Biomedical Monitoring Systems," *Sensors and Actuators,* vol. 147, pp. 641-648, 2008.

[35] E. Kennedy, Operational Amplifier Circuits: Theory and Applications, Fort Worth: Holt, Rinehart and Winston, Inc., 1988.

[36] M. Bao, Handbook of Sensors and Actuators, Volume 8, Micromechanical Transducers, Amsterdam: Elsevier B.V., 2000.

[37] K. Hoffman, An Introduction to Measurements Using Strain Gages, Darmstadt: Hottinger Baldwin Messtechnik GmbH, 1989.

[38] National Oceanic and Atmospheric Administration, "Most intense tropical cyclone on record," 21 April 2010. [Online]. Available: http://www.aoml.noaa.gov/hrd/tcfaq/E1.html. [Accessed 26 July 2013].

[39] World Meteological Organization, "World: Highest Sea Level Air Pressure Above 750 meters," Arizona State University School of Geographical Sciences, 2010. [Online]. Available: http://wmo.asu.edu/highest-sea-lvl-air-pressure-above-700m. [Accessed 22 July 2013].

[40] World Meteorlogical Organization, "World: Highest Sea Level Air Pressure Below 750 meters," Arizona State University School of Geographical Sciences, 2010. [Online]. Available: http://wmo.asu.edu/world-highest-sea-level-air-pressure-below-700m. [Accessed 22 July 2013].

[41] M. L. Simpson, C. L. Britton, A. L. Wintenberg and G. R. Young, "An Integrated CMOS Time Interval Measurement System with Subnanosecond Resolution for the WA-98 Calorimeter," *IEEE Journal of Solid State Circuits,* vol. 32, no. 2, pp. 198-205, 1997.

[42] D. M. Binkley and M. E. Casey, "Performance of Fast Monolithic ECL Voltage Comparators in Constant-Fraction Discriminators and Other Timing Circuits," *IEEE Transactions on Nuclear Science,* vol. 35, no. 1, pp. 226-230, 1988.

[43] "Principles and Application of Timing Spectroscopy," EG&G ORTEC, Oak Ridge.

[44] M. L. Simpson, C. L. Britton, A. L. Wintenberg and G. R. Young, "An Integrated, CMOS, Constant-Fraction Timing Discriminator for Multichannel Detector Systems," *IEEE Transactions on Nuclear Science,* vol. 42, no. 4, pp. 762-766, 1995.

[45] J. Sotelo, "The hydrokinetic parameters of shunts for hydrocephalus might be inadequate," *Surgical Neurology International,* vol. 3, no. 40, 2012.

Appendix

MLV Series Low Voltage Pressure Sensors

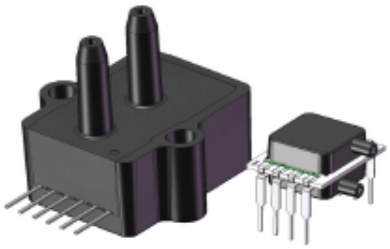

Features

- 1 to 30 inH2O & 5 to 150 PSI Pressure Ranges
- 5V Operation
- High Output
- Low Power Consumption
- Excellent Position Sensitivity
- Low Warm-Up Shift
- Enhanced Front to Back Linearity
- Protective Parylene Coating Option

Applications

- Medical Breathing
- Environmental Controls
- HVAC
- Industrial Controls
- Portable/Hand-Held Equipment

General Description

The MLV Series Compensated Sensor is based on All Sensors' CoBeam²™ Technology². The device provides a high output signal at a low operating voltage while maintaining comparable output levels to traditional equivalent compensated millivolt sensors operating at higher voltages. This lower supply voltage gives rise to improved warm-up shift while the CoBeam² Technology itself reduces package stress susceptibility resulting in improved overall long term stability. The technology also vastly improves position sensitivity compared to conventional single die devices.

These calibrated and compensated sensors give an acurate and stable output over a wide temperature range. This series is intended for use with non-corrosive, non-ionic working fluids such as air, dry gases and the like. A protective parylene coating is optionally available for moisture/harsh media protection. The output is also ratiometric to the suply voltage and designed to operate at 5.0 volts DC.

Standard Pressure Ranges

Device	Operating Range	Proof Pressure	Burst Pressure	Nominal Span
MLV-L01D	±1 inH2O	100 inH2O	300 inH2O	7 mV
MLV-L02D	±2 inH2O	100 inH2O	300 inH2O	10 mV
MLV-L05D	±5 inH2O	200 inH2O	300 inH2O	15 mV
MLV-L10D	±10 inH2O	200 inH2O	300 inH2O	20 mV
MLV-L20D	±20 inH2O	200 inH2O	500 inH2O	20 mV
MLV-L30D	±30 inH2O	200 inH2O	800 inH2O	20 mV
MLV-005D	±5 PSI	10 PSI	30 PSI	25 mV
MLV-015D	±15 PSI	60 PSI	120 PSI	37.5 mV
MLV-015A	0 - 15 PSIA	60 PSI	120 PSI	37.5 mV
MLV-030D	±30 PSI	90 PSI	150 PSI	37.5 mV
MLV-100D	±100 PSI	200 PSI	250 PSI	37.5 mV
MLV-150D	±150 PSI	200 PSI	250 PSI	37.5 mV

Equivalent Circuit

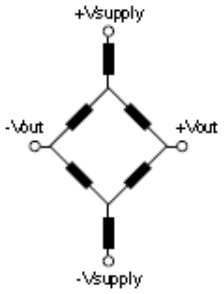

Approvals

MKT	DATE	MFG	DATE	ENG	DATE	QA	DATE
☐ As Is ☐ With Change		☐ As Is ☐ With Change		☐ As Is ☐ With Change		☐ As Is ☐ With Change	

all sensors
a 16035 Vineyard Blvd. Morgan Hill, CA 95037 p 408 225 4314 f 408 225 2079 e www.allsensors.com

Pressure Sensor Maximum Ratings	
Supply Voltage (Vs)	12 Vdc
Common Mode Pressure	
InH2O Devices (L01, L02, L05, L10, L20, L30)	10 psig
PSI Devices (005, 015, 030, 100, 150)	50 psig
Lead Temperature (soldering 2-4 sec.)	270 °C

Environmental Specifications	
Temperature Ranges	
Compensated	0°C to 50°C
Operating	-25°C to 85 °C
Storage	-40°C to 125 °C
Humidity Limits	0 to 95% RH (non condensing)

Performance Characteristics for MLV Series (InH2O)

ALL PARAMETERS ARE MEASURED AT 5.0 VOLT EXCITATION AND ROOM TEMPERATURE UNLESS OTHERWISE SPECIFIED. PRESSURE MEASUREMENTS ARE WITH POSITIVE PRESSURE APPLIED TO PORT B (THE ONLY PORT FOR THE SINGLE PORT CONFIGURATION PACKAGES).

Parameter	Min	Typ	Max	Units	Notes
Output Span					
L01D @ 1 inH2O	6.0	7.0	8.0	mV	4
L02D @ 2 inH2O	9.0	10.0	11.0	mV	4
L05D @ 5 inH2O	14.0	15.0	16.0	mV	4
L10D @ 10 inH2O	19.0	20.0	21.0	mV	4
L20D @ 20 inH2O	19.0	20.0	21.0	mV	4
L30D @ 30 inH2O	19.0	20.0	21.0	mV	4
Span Temperature Shift (0°C to 50°C)	-	-	±250	uV	1
Offset Voltage @ Zero Diff. Pressure	-	-	±500	uV	-
Offset Temperature Shift (0°C to 50°C)					
L01D, L02D, L05D	-	-	±250	uV	1
L10D, L20D, L30D	-	-	±200	uV	1
Offset Warm-up Shift	-	-	±50.0	uV	2
Offset Position Sensitivity (1g)					
L01D	-	-	±20.0	uV	6
L02D	-	-	±15.0	uV	6
L05D, L10D, L20D, L30D	-	-	±10.0	uV	6
Offset Long Term Drift (One Year)					
L01D, L02D, L05D	-	±150	-	uV	-
L10D, L20D, L30D	-	±100	-	uV	-
Linearity, Hysteresis Error	-	0.10	0.30	%FSS	3
Response Time (10% to 90% Pressure Response)	-	500	-	us	-
Front to Back Linearity	-	0.75	-	%FSS	5
Input Resistance	-	12.0	-	k ohm	-
Output Resistance	-	3.0	-	k ohm	-

Performance Characteristics for MLV Series (PSI)

ALL PARAMETERS ARE MEASURED AT 5.0VOLT EXCITATION AND ROOM TEMPERATURE UNLESS OTHERWISE SPECIFIED. PRESSURE MEASUREMENTS ARE WITH POSITIVE PRESSURE APPLIED TO PORT B (THE ONLY PORT FOR THE SINGLE PORT CONFIGURATION PACKAGES).

Parameter	Min	Typ	Max	Units	Notes
Output Span					
005D @ 5 PSI	24.0	25.0	26.0	mV	4
015D @ 15 PSI	36.5	37.5	38.5	mV	4
015A @ 15 PSIA	36.5	37.5	38.5	mV	4
030D @ 30 PSI	36.5	37.5	38.5	mV	4
100D @ 100 PSI	36.5	37.5	38.5	mV	4
150D @ 150 PSI	36.5	37.5	38.5	mV	4
Span Temperature Shift (0°C to 50°C)	-	-	±1.0	mV	1
Offset Voltage @ Zero Diff. Pressure	-	-	±300	uV	-
Offset Temperature Shift (0°C to 50°C)	-	-	±300	uV	1
Offset Warm-Up Shift	-	-	±50	uV	2
Offset Long Term Draft (one year)	-	±100	-	uV	-
Linearity, Hysteresis Error	-	0.20	0.50	%FSS	3
Response Time (10% to 90% Pressure Response)	-	500	-	us	-
Front to Back Linearity	-	0.75	-	%FSS	5
Input Resistance	-	1.20	-	kohm	-
Output Resistance	-	3.0	-	kohm	-

Specification Notes

NOTE 1: SHIFT IS RELATIVE TO 25°C.

NOTE 2: SHIFT IS WITHIN THE FIRST HOUR OF EXCITATION APPLIED TO THE DEVICE.

NOTE 3: MEASURED AT ONE-HALF FULL SCALE RATED PRESSURE USING BEST STRAIGHT LINE CURVE FIT.

NOTE 4: THE SPAN IS THE ALGEBRAIC DIFFERENCE BETWEEN FULL SCALE OUTPUT VOLTAGE AND THE OFFSET VOLTAGE.

NOTE 5: FRONT-BACK LINEARITY COMPUTED AS: $L_{FB} = \left(\left| \frac{Span_{Front}}{Span_{Back}} \right| - 1 \right) \cdot 100\%$

NOTE 6: PARAMETER IS CHARACTERIZED AND NOT 100% TESTED.

a 16035 Vineyard Blvd. Morgan Hill, CA 95037 p 408 225 4314 f 408 225 2079 e www.allsensors.com all sensors

How To Order

A Package

Example: MLV-L02D-A6BBF-N

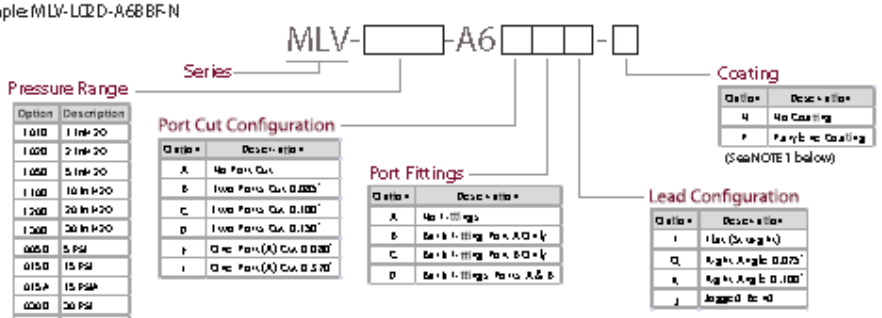

Option	Description
1D1D	1 inH2O
1D2D	2 inH2O
1D5D	5 inH2O
1100	10 inH2O
1200	20 inH2O
1300	30 inH2O
005D	5 PSI
015D	15 PSI
015A	15 PSIA
0300	30 PSI
1001	100 PSI
1501	150 PSI

Option	Description
A	No Port Cut
B	Two Ports Cut 0.035"
C	Two Ports Cut 0.100"
D	Two Ports Cut 0.150"
E	One Port (A) Cut 0.035"
F	One Port (A) Cut 0.370"

Option	Description
A	No Fittings
B	Barbed Fitting Port A Only
C	Barbed Fitting Port B Only
D	Barbed Fittings Ports A & B

Option	Description
N	No Coating
P	Parylene Coating

Option	Description
1	Flex (Straight)
Q	Right Angle 0.075"
R	Right Angle 0.100"
J	Jagged Bend

E Package

Example: MLV-L02D-E1ND-N

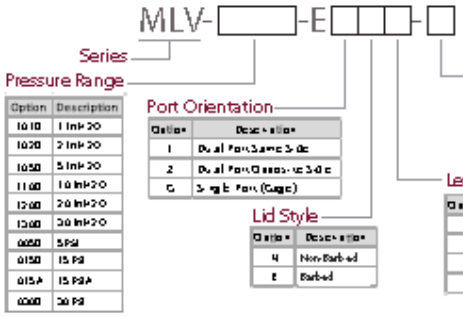

Option	Description
1D1D	1 inH2O
1D2D	2 inH2O
1D5D	5 inH2O
1100	10 inH2O
1200	20 inH2O
1300	30 inH2O
005D	5 PSI
015D	15 PSI
015A	15 PSIA
0300	30 PSI

Option	Description
1	Dual Port, Same Side
2	Dual Port, Opposite Side
G	Single Port (Gage)

Option	Description
S	SIP
D	DIP
J	J-Lead SMT
L	Low Profile DIP

Option	Description
N	Non-Barbed
B	Barbed

Option	Description
N	No Coating
P	Parylene Coating

TABLE 1: Available E-Series Package Configurations

Port Orientation	Non-Barbed Lid Style: Lead Style				Barbed Lid Style: Lead Style			
	SIP	DIP	J-Lead SMT	Low Profile DIP	SIP	DIP	J-Lead SMT	Low Profile DIP
Dual Port, Same Side	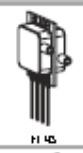			N/A			N/A	N/A
Dual Port, Opposite Side	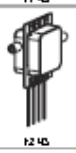			N/A			N/A	N/A
Single Port (Gage)								

NOTE 1) Parylene Coating: Parylene coating provides a moisture barrier and protection from some harsh media. Consult factory for applicability of Parylene for the target application and sensor type.

A6 Package (Without Options)

Pinout
1) N/C
2) Vs
3) +Out
4) Gnd
5) -Out
6) N/C

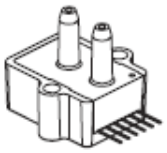

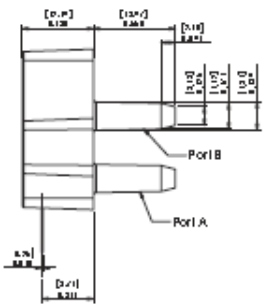

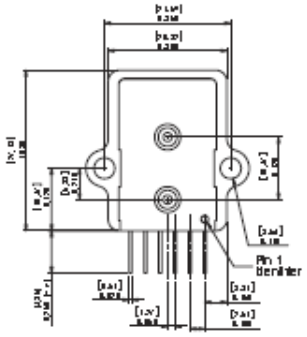

NOTES
1) Dimensions are in inches [mm].
2) For suggested pad layout see drawing: PAD-DP

A-Package: Port Cut Options

Example: MLV-L10D-A6**X**AF-N
Port Cut Options

A- No Port Cut Configuration

D- Two Ports Cut 0.150" Configuration

B- Two Ports Cut 0.085" Configuration

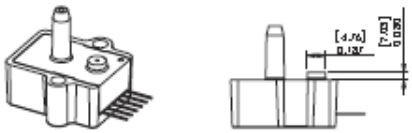

E- Port A cut 0.080" Configuration

C- Two Ports Cut 0.100" Configuration

F- Port A Cut 0.370" Configuration

a 16035 Vineyard Blvd. Morgan Hill, CA 95037 p 408 225 4314 f 408 225 2079 e www.allsensors.com all sensors

A-Package: Port Fitting Options

Example: MLV-L10D-A6DxF-N

Port Fitting Options

NOTE: Port Cut Configuration "D" Shown As Reference.

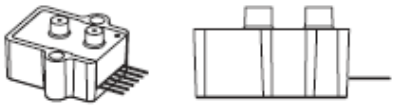

A- No Fittings Configuration

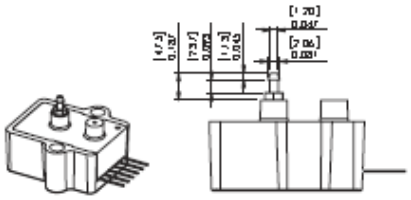

C- Barb Fitting Port B Only Configuration

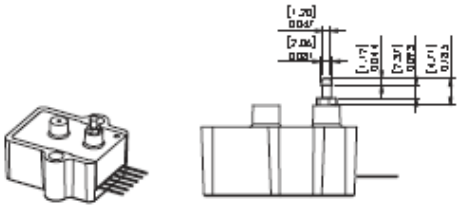

B- Barb Fitting Port A Only Configuration

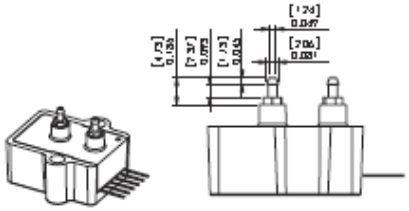

D- Barb Fitting Ports A and B Configuration

A-Package: Lead Bend Options

Example: MLV-L10D-A6AAx-N

Lead Bend Options

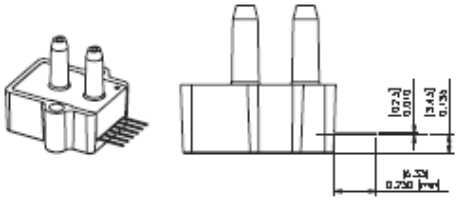

F- Flat (Straight) Configuration

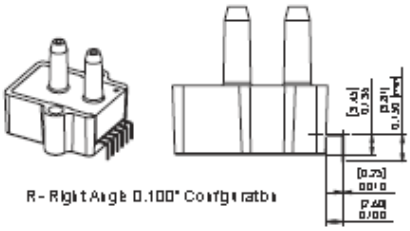

R- Right Angle 0.100" Configuration

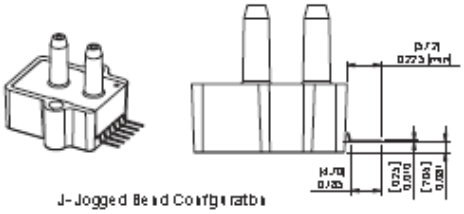

J- Jogged Bend Configuration

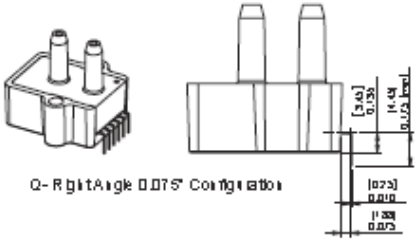

Q- Right Angle 0.075" Configuration

E1NS Package

Pinout
1) Gnd
2) +Out
3) Vs
4) -Out

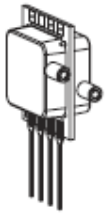

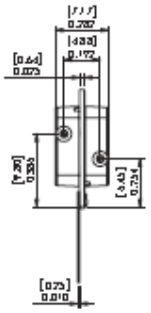

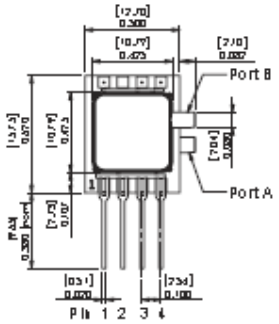

NOTES
1) Dimensions are in inches [mm]
2) For suggested pad layout, see drawing: PAD-01

E1BS Package

Pinout
1) Gnd
2) +Out
3) Vs
4) -Out

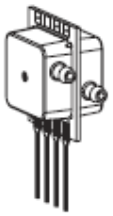

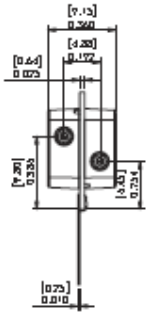

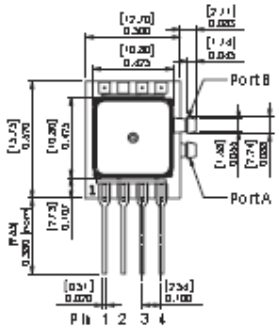

NOTES
1) Dimensions are in inches [mm]
2) For suggested pad layout, see drawing: PAD-01

a 16035 Vineyard Blvd. Morgan Hill, CA 95037 p 408 225 4314 f 408 225 2079 e www.allsensors.com all sensors

E2NS Package

Pinout
1) Gnd
2) +Out
3) Vs
4) -Out

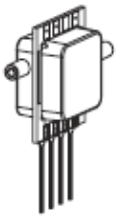

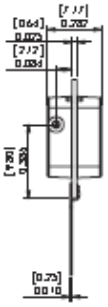

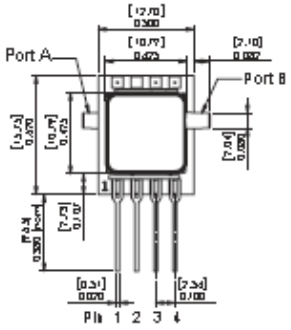

NOTES
1) Dimensions are in inches [mm]
2) For suggested pad layout, see drawing : PAD-01

E2BS Package

Pinout
1) Gnd
2) +Out
3) Vs
4) -Out

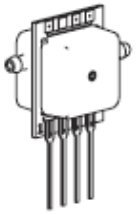

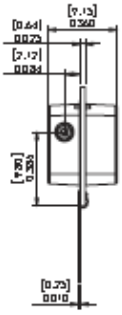

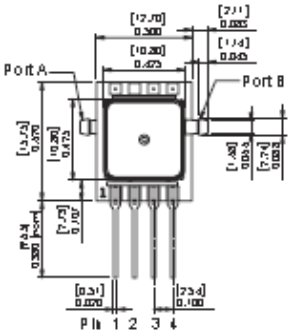

NOTES
1) Dimensions are in inches [mm]
2) For suggested pad layout, see drawing : PAD-01

EGNS Package

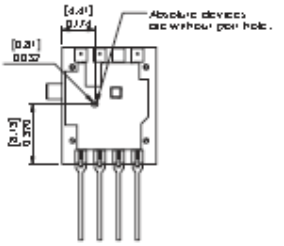

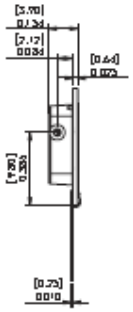

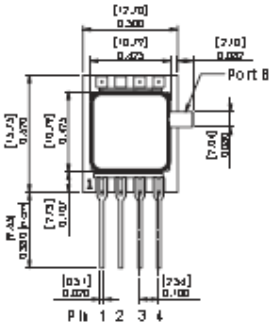

Pinout
1) Gnd
2) +Out
3) Vs
4) -Out

NOTES
1) Dimensions are in inches [mm]
2) For suggested pad layout, see drawing: PAD-01

EGBS Package

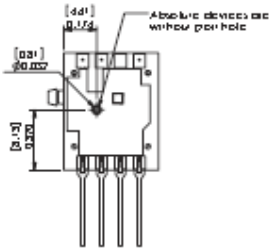

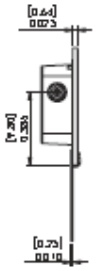

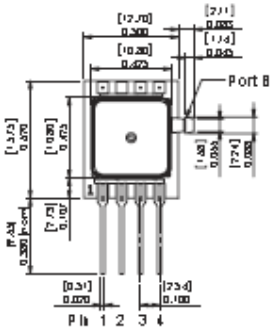

Pinout
1) Gnd
2) +Out
3) Vs
4) -Out

NOTES
1) Dimensions are in inches [mm]
2) For suggested pad layout, see drawing: PAD-01

a 16035 Vineyard Blvd. Morgan Hill, CA 95037 p 408 225 4314 f 408 225 2079 e www.allsensors.com all sensors

E1ND Package

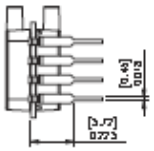

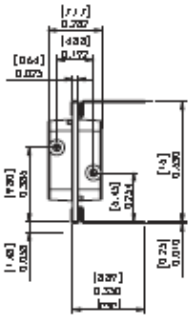

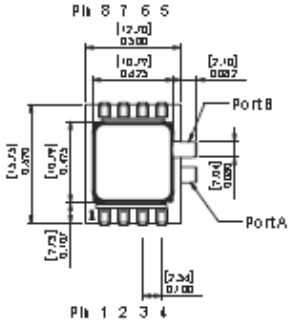

Pinout
1) Gnd
2) +Out
3) Vs
4) -Out
5) Do Not Connect
6) Do Not Connect
7) Do Not Connect
8) Do Not Connect

NOTES
1) Dimensions are in inches [mm]
2) For suggested pad layout, see drawing: PAD-03

E1BD Package

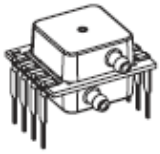

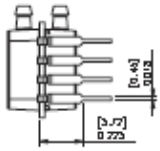

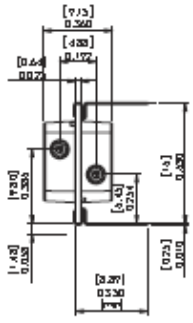

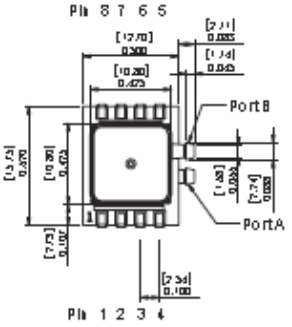

Pinout
1) Gnd
2) +Out
3) Vs
4) -Out
5) Do Not Connect
6) Do Not Connect
7) Do Not Connect
8) Do Not Connect

NOTES
1) Dimensions are in inches [mm]
2) For suggested pad layout, see drawing: PAD-03

E2ND Package

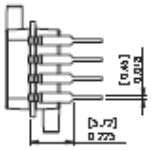

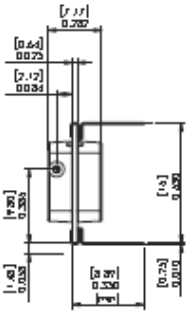

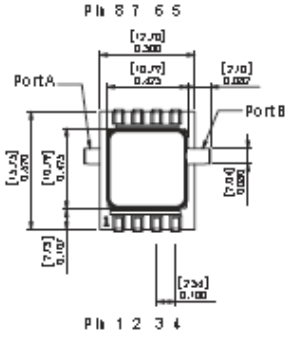

Pinout
1) Gnd
2) +Out
3) Vs
4) -Out
5) Do Not Connect
6) Do Not Connect
7) Do Not Connect
8) Do Not Connect

NOTES
1) Dimensions are in inches [mm]
2) For suggested pad layout, see drawing: PAD-03

E2BD Package

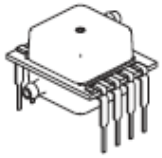

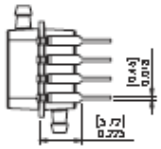

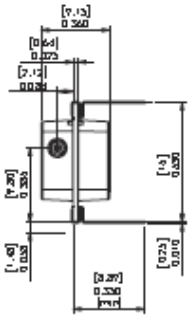

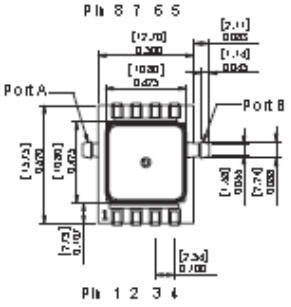

Pinout
1) Gnd
2) +Out
3) Vs
4) -Out
5) Do Not Connect
6) Do Not Connect
7) Do Not Connect
8) Do Not Connect

NOTES
1) Dimensions are in inches [mm]
2) For suggested pad layout, see drawing: PAD-03

a 16035 Vineyard Blvd. Morgan Hill, CA 95037 p 408 225 4314 f 408 225 2079 e www.allsensors.com all sensors

EGND Package

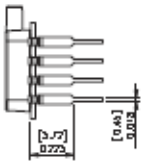

Pinout
1) Gnd
2) +Out
3) Vs
4) -Out
5) Do Not Connect
6) Do Not Connect
7) Do Not Connect
8) Do Not Connect

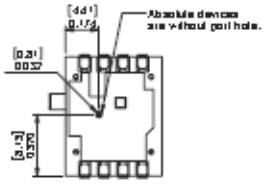

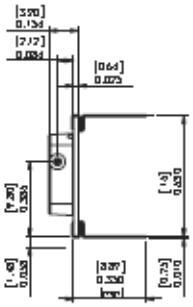

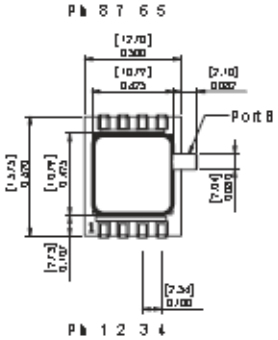

NOTES
1) Dimensions are in inches [mm]
2) For suggested pad layout, see drawing: PAD-03

EGBD Package

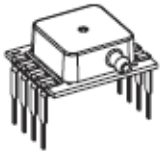

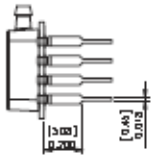

Pinout
1) Gnd
2) +Out
3) Vs
4) -Out
5) Do Not Connect
6) Do Not Connect
7) Do Not Connect
8) Do Not Connect

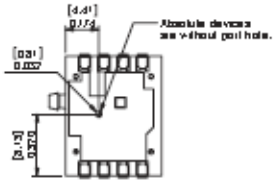

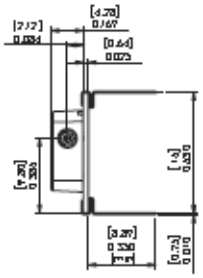

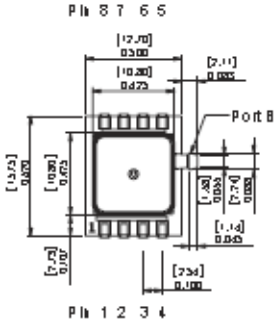

NOTES
1) Dimensions are in inches [mm]
2) For suggested pad layout, see drawing: PAD-03

E1NJ Package

Pinout
1) Gnd
2) +Out
3) Vs
4) -Out
5) Do Not Connect
6) Do Not Connect
7) Do Not Connect
8) Do Not Connect

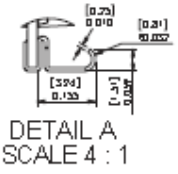

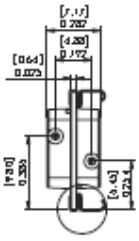

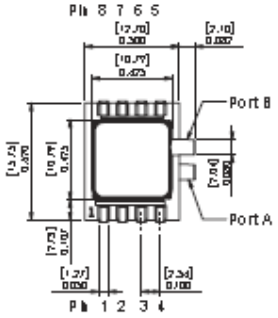

NOTES
1) Dimensions are in inches [mm]
2) For suggested pad layout, see drawing: PAD-10

E2NJ Package

Pinout
1) Gnd
2) +Out
3) Vs
4) -Out
5) Do Not Connect
6) Do Not Connect
7) Do Not Connect
8) Do Not Connect

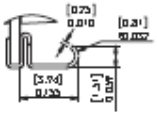

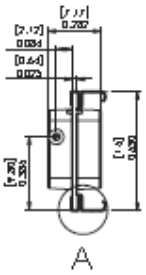

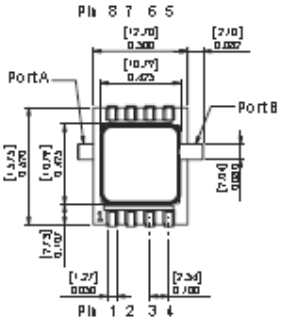

NOTES
1) Dimensions are in inches [mm]
2) For suggested pad layout, see drawing: PAD-10

a 16035 Vineyard Blvd. Morgan Hill, CA 95037 p 408 225 4314 f 408 225 2079 e www.allsensors.com all sensors

EGNJ Package

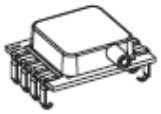

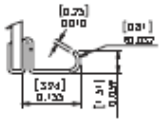

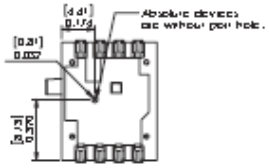

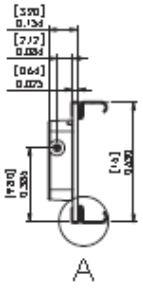

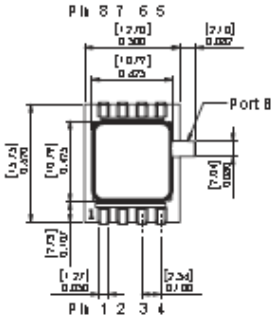

Pinout
1) Gnd
2) +Out
3) Vs
4) -Out
5) Do Not Connect
6) Do Not Connect
7) Do Not Connect
8) Do Not Connect

NOTES
1)Dimensions are in inches [mm]
2)For suggested pad layout, see drawing: PAD-10

EGBJ Package

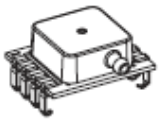

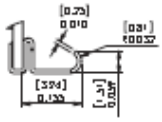

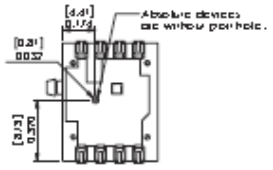

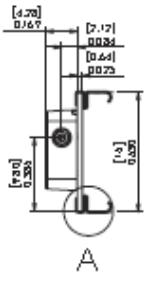

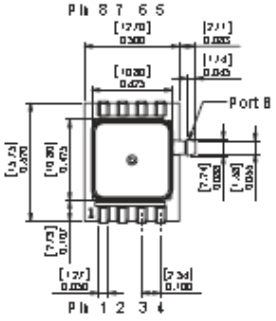

Pinout
1) Gnd
2) +Out
3) Vs
4) -Out
5) Do Not Connect
6) Do Not Connect
7) Do Not Connect
8) Do Not Connect

NOTES
1)Dimensions are in inches [mm]
2)For suggested pad layout, see drawing: PAD-10

EGNL Package

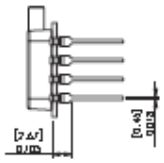

Pinout
1) Gnd
2) +Out
3) Vs
4) -Out
5) Do Not Connect
6) Do Not Connect
7) Do Not Connect
8) Do Not Connect

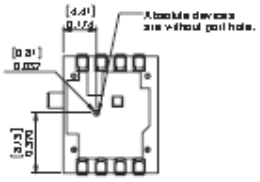

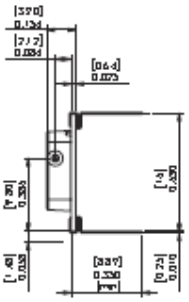

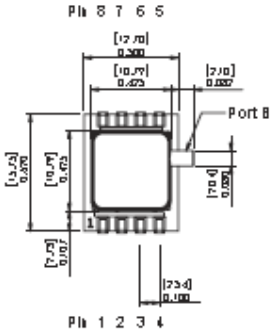

NOTES
1) Dimensions are in inches [mm]
2) For suggested pad layout, see drawing: PAD-03

EGBL Package

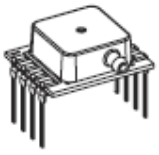

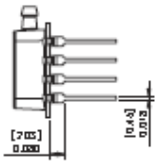

Pinout
1) Gnd
2) +Out
3) Vs
4) -Out
5) Do Not Connect
6) Do Not Connect
7) Do Not Connect
8) Do Not Connect

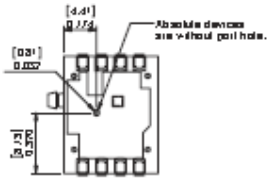

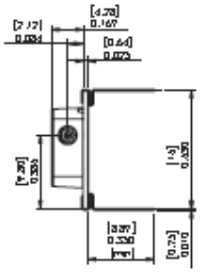

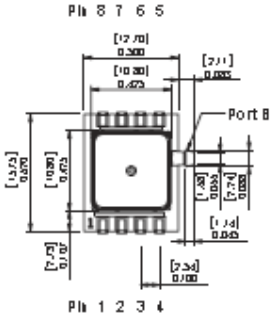

NOTES
1) Dimensions are in inches [mm]
2) For suggested pad layout, see drawing: PAD-03

a 16035 Vineyard Blvd. Morgan Hill, CA 95037 p 408 225 4314 f 408 225 2079 e www.allsensors.com all sensors

Suggested Pad Layout

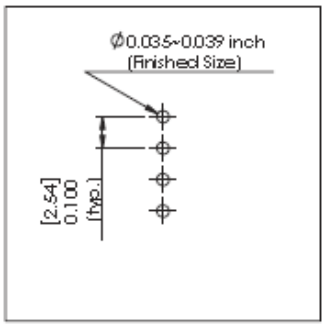

PAD-01

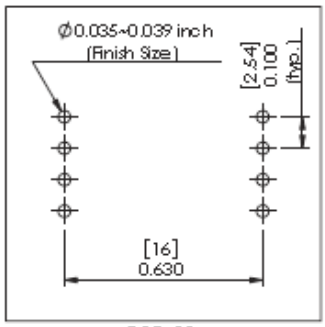

PAD-03

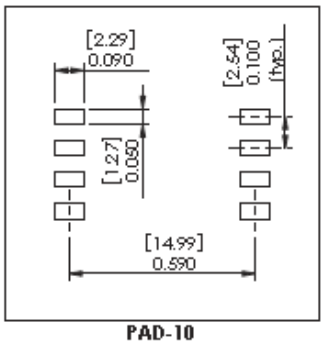

PAD-10

Package Characteristics

	Approximate Port Volume						
Package ID	Port A	Port B	Units	Notes	Weight	Units	Notes
A6AAx	132	33.6	mm^3	1	9.3	Grams	2
A6BAx	119	20.3	mm^3	1	8.7	Grams	2
A6CAx	119	20.5	mm^3	1	8.8	Grams	2
A6DAx	120	21.3	mm^3	1	8.8	Grams	2
A6EAx	119	33.6	mm^3	1	8.9	Grams	2
A6FAx	125	33.6	mm^3	1	9.2	Grams	2
E1Nx	174	168	mm^3	-	1.2	Grams	-
E2Nx	174	168	mm^3	-	1.2	Grams	-
EGNx	1.4	168	mm^3	-	0.9	Grams	-

Package Notes
Note 1: Add 4.5 mm^3 per port with barb fitting.
Note 2: Add 0.15 gram per barb fitting.

Product Labeling

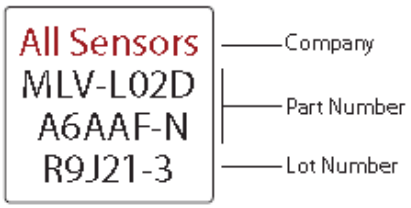

Example Device Label

* 5 PSI to 150 PSI devices may not be assembled with CoBeam2™ Technology.

Vita

Chad Eric Seaver is a native of East Tennessee and was born during the year of 1973. He graduated from Volunteer High in 1992 and thereafter attended the University of Tennessee where he studied Electrical Engineering with an emphasis upon embedded processing. He joined the Oak Ridge National Laboratory's (ORNL) Chemical Technology division in 1995 supporting the development of remotely operated robotics as an Engineering Intern. Upon graduation with a Bachelor of Science degree in Electrical Engineering in 1996, he joined the full time staff of ORNL continuing to develop remotely operated robotics for hazardous duty deployment. He thereafter developed similar unmanned ground vehicles during his employment with Northrup Grumman. Chad later worked as a Senior Specialist for the global automotive firm, Denso, before he discovered his passion in Biomedical Engineering. In 2000, Chad joined CTI Molecular Imaging as a Development Engineer where he designed medical image processing electronics. He advanced to Business Manager with the firm and later was promoted to Senior Manager of Engineering after the company's acquisition by Siemens Medical Solutions. During his tenure with Siemens, Chad began pursuit of his Master of Science degree in Electrical Engineering with an emphasis upon analog electronics for biosensing as well as studies within medical physics. In 2011, Chad co-founded the neurosurgical medical device firm, Arkis BioSciences. In 2013, Chad completed his Master of Science degree and also began leading Arkis BioSciences as Chief Executive Officer. Chad is the proud father of two boys, Alex and Evan, and cherishes his marriage to his wife Patricia.